University of Nottingham
UK | CHINA | MALAYSIA

Development Of A Novel TEHL to CFD Coupling Methodology In OpenFOAM

Thesis submitted to the University of Nottingham for the degree of
Doctor of Philosophy, September 2024.

James Layton

14273719

Supervised by

Dr Stephen Ambrose, Dr Benjamin C Rothwell, Prof Carol Eastwick, Dr Humberto Medina

Signature _____

Date _____ / _____ / _____

Abstract

Enhancing the efficiency of aero-engines requires their transmissions systems to be capable of higher energy densities, which inevitably increases the thermal load that is generated within the system. Lubricated contacts that operate hydrodynamically are a significant source of heat in the system caused by the extreme shearing of the lubricating oil. Journal bearings are key components in high power transmission that operate in a hydrodynamic regime and are used for their low friction, wear and power loss performance in highly loaded and high speed conditions. While there is significant research in the field of tribology on hydrodynamic lubrication for journal bearings and other types of contacts, numerical models are generally confined to the contact region and their effects are not considered in the context of the broader domain. The pressure and temperature developed in the oil within the contact region will impact the behaviour of the fluid after is exits the region, and furthermore the oil flow prior to entering the contact will impact the lubrication performance. Therefore, there is a need for numerical models to consider hydrodynamic lubrication within the broader system domain.

In this thesis a multi-region numerical model is developed where the domain is discretised into three types of regions, applying separate governing equation systems. The region types are the Thermo-Elastohydrodynamic Lubrication (TEHL) region applying a lubrication model for hydrodynamic regimes, the CFD type region applying a Naier-Stokes based fluid simulation model, and the Solid type region. The regions are solved sequentially in a global iterative scheme that converges the solution of all the regions. The coupling of the solutions is obtained by the interfacing boundary conditions that use the latest solutions for the neighbouring regions in their application.

The TEHL model is based on the Reynolds equation from Reynolds (1886) which is funda-

mental to lubrication theory and modeling in tribology. This type of model is beneficial for its low computational cost compared to applying a Navier-Stokes based CFD model to simulate a hydrodynamic lubrication regime, which is highly computationally expensive. The TEHL model incorporates cavitation using the model from Elrod & Adam M. L. (1974) and a liquid gas model for the fluid properties, deformation of the surfaces using the half-space approximation Hertz (1881), thermal effects using a temperature equation and viscosity-temperature power law model.

The CFD model is based on the Navier-Stokes equations in an incompressible form and is initially considered as steady-state. An energy equation is incorporated for coupling the thermal effects and a viscosity-temperature model is included in this region. Turbulence effects are Incorporated using the $k-\varepsilon$ model. In Chapter 5, multi-phase effects are introduced using the Volume of Fluid (VoF) method as a preliminary investigation for expanding the model. In the VoF cases the simulations are transient.

The Solid type model considers steady-state heat conduction through the region of a homogeneous material.

A comparison of the TEHL model to experimental results is performed for a journal bearing case. Pressure profiles showed good agreement with the experimental profiles in terms of their general shape and position of the peak and cavitation regions. Temperature profiles showed good agreement in general profile and trends. There is some notable difference near the inlet where the numerical model over predicts the temperature in the region.

The CFD model is introduced into the journal bearing case to simulate the mixing between the supply and recirculating oil. Similar agreement is shown between the numerical and experimental results for the fluid pressure and temperature when the CFD model is introduced, showing the conditions within the supply groove are being simulated well by the CFD model. Good consistency of the pressure, temperature and velocity fields is observed at the numerical interfaces showing the solutions between the regions are being coupled.

Ongoing work with the model includes incorporating multi-phase effects and defining suitable boundary conditions for multi-phase simulations. A new case involving a half-journal experimental rig, developed separately from this work, provides an opportunity to validate the

multi-phase introduction into the CFD model by visualizing the oil inflow and outflow.

The numerical model developed in thesis is applicable to many scenarios in industry where coupling between hydrodynamic regimes and the broader domain is significant. Further applications include the disintegration of oil from journal bearings which is influenced by the temperature and pressure in the lubricating film, thrust bearing type configurations, lubrication of piston ring seal and rolling element bearing.

Preface

The research work presented in this thesis was carried out at the University of Nottingham's Mechanical and Aerospace Systems (MAS) research group, which is also home to the Rolls-Royce University Technology Centre (UTC) in gas turbine transmission systems, between October 2020 and September 2024. The authors thank Rolls-Royce plc and the EPSRC for the support under the Prosperity Partnership Grant Cornerstone: Mechanical Engineering Science to Enable Aero Propulsion Futures", Grant Ref: EP/R004951/1.

I hereby confirm that this dissertation is my own work and contains nothing which is the outcome of work carried out in collaboration with others, except as specified in the text and acknowledgments. Whenever information from other authors was used, an appropriate reference was made. No parts of this work have been submitted to any other University or Institution for any other qualification.

Acknowledgements

I would like to thank my academic supervisors, Dr. Stephen Ambrose, Dr Benjamin C Rothwell, Prof. Carol Eastwick and Dr. Humberto Medina, for their support and mentorship during the course of my PhD. Their experience and insight were significant to the results in this thesis and to my own personal development.

I would like to thank Rolls-Royce plc and the EPSRC for the support under the Prosperity Partnership Grant Cornerstone: Mechanical Engineering Science to Enable Aero Propulsion Futures, Grant Ref: EP/R004951/1.

Nomenclature

Symbol	Unit	Description
α	K^{-1}	Coefficient of thermal expansion
β	Pa	Bulk modulus (compressibility)
c	m	Journal bearing clearance
c_p	$J \cdot kg^{-1} \cdot K^{-1}$	Specific heat capacity
D	m	Diameter
ε	-	Relative displacement of the shaft centre from the bush centre
E	Pa	Young's modulus
E'	Pa	Adjusted Young's modulus
g	-	Switch function
h	m	Height of the lubricating film
h_e	m	Journal bearing film height from the eccentricity of the shaft
h_d	m	Film height from the surfaces elastic deformation
h_T	m	Film height from thermal expansion of the bodies
He	-	Hersey number
k	$W \cdot m^{-1} \cdot K^{-1}$	Thermal conductivity
L	m	Length
μ	Pas	Dynamic viscosity
$\dot{M}$	$kg \cdot s^{-1}$	Mass flow rate
ν	-	Poisson's ratio
N	rpm	Rotational speed
θ	rad	Angular position
P	Pa	Pressure
P_{cav}	Pa	Cavitation pressure
ρ	$kg \cdot m^{-3}$	Density
ρ_{cav}	$kg \cdot m^{-3}$	Density at cavitation pressure
ϕ	-	Density relative to density at cavitation pressure
$\dot{Q}$	$m^3 \cdot s^{-1}$	Volume flow rate
R	m	Radius
T	K	Temperature
U	$m \cdot s^{-1}$	Average velocity between surfaces that contain a lubricating film
u	$m \cdot s^{-1}$	Circumferential velocity
v	$m \cdot s^{-1}$	Radial Velocity
w	$m \cdot s^{-1}$	Axial velocity
W	N	Normal load
x'	m	Circumferential direction
y'	m	Radial direction
z'	m	Axial direction
γ_T	k^{-1}	Viscosity-temperature coefficient

Acronym	Description
EHL	ElastoHydrodynamic Lubrication
$TEHL$	Thermo-ElastoHydrodynamic Lubrication
CFD	Computational Fluid Dynamics
FEM	Finite Element Method
FSI	Fluid-Solid Interaction
BDC	Bottom Dead Centre
TDC	Top Dead Centre

Contents

List of Tables

List of Figures

Chapter 1

Introduction

In this chapter the background to the research conducted in this thesis is described from the original motivations from the aerospace industry. An overview of previous related research is given to contextualise the work along with the industrial incentive. The key aims and objectives of the project are listed and the end of the chapter followed by key contributions of knowledge made during the project.

1.1 Background and Context

The human impact on climate change and the environment from carbon dioxide emissions is widely acknowledged and is a major factor influencing the direction of research and development in industry. In response, international targets and national policies have been introduced to encourage the European aircraft industry towards more sustainable solutions, for example, in the Flightpath 2050 European Commission *et al.* (2011) report which proposes reducing CO_2 emissions by 75%, NOx emissions by 90% and noise by 65% by 2050. The targets for the aviation industry are reinforced in the UK's Jet Zero Strategy Department For Transport (2022) which outlines a framework for reducing carbon emissions approaching the year 2050. One factor within the strategy is to improve fuel efficiency in aircraft propulsion systems to reduce their total carbon emission, which contributes 15% toward achieving the net zero target as shown in Figure 1.1.

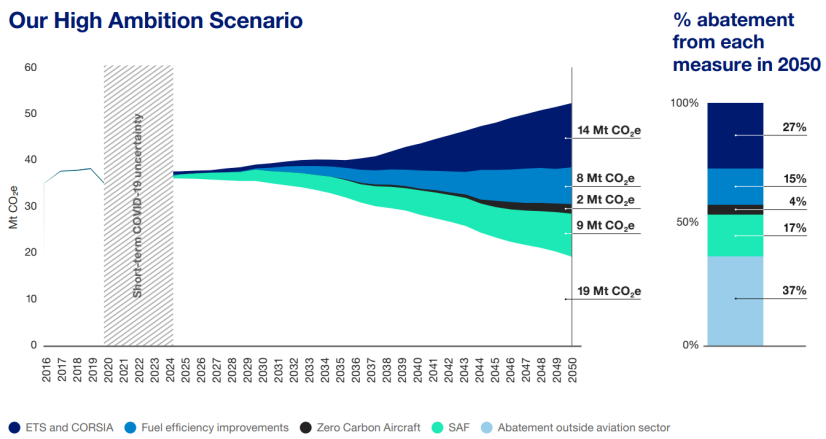

Figure 1.1: Contributing factors to reducing CO_2 emission by 2050, comparison with prediction, from Jet Zero Strategy Department For Transport (2022)

The power density within the latest generations of Aircraft engines is increasing to maximise their fuel efficiency, such as the Rolls-Royce Ultra Fan Engine Rolls-Royce (n.d.) which is currently recorded to have delivered a power of 64MW from its gearbox. With gearbox efficiency in the order of 99%, the energy loss in the gear system is in the range of 600kW in this example, which is predominantly lost as heat. This thermal load is substantially managed by the oil lubrication system, which must adapt to the increasing amount of heat generated in later generations of aerospace engines. Increases in weight and size are counteractive to reducing emissions, therefore, targeted improvements based on the fundamental phenomena and flow behaviour is needed to improve the systems efficiency and performance. Simulation capabilities are a significant enabler to this development.

A notable uncertainty is the amount of oil which must be fed into lubricated contact regions, such as in bearings and gears, which if over supplied can generate more heat from overworking the oil, however if there is insufficient supply the lubrication performance is impacted. Lubricated contacts are often designed to operate hydrodynamically where a film of the lubricant is driven into a contact region by the components motion and separates the interacting surfaces. This behaviour is ideal for high speed and load components as the film of lubricant significantly reduces friction, wear and energy loss. A minimum flow rate of lubricant to the contact is required to maintain the film, if the supply is insufficient the lubricant performance suffers. The ideal supply rate to minimise over-working the oil would therefore be the minimum to maintain the lubricating film. Furthermore, the lubricated contact creates a significant pres-

sure in the film which causes the fluid to be dispersed from the contact, contributing to flow patterns of oil in the wider system. Predicting the flow of oil is necessary for optimising the thermal performance of the system. This demonstrates the coupled nature between lubricated contacts and the wider domain.

A component which fundamentally relies on the hydrodynamic lubrication phenomena is journal bearings which are effective at supporting shafts at high rotational speed and carrying high loads. They are key components in high-power transmission systems because of their low friction and wear during operation, thereby reducing the energy lost in the system and maximising lifetime. Several aspects of the journal bearings operation contribute to the efficiency of the broader system; high shearing of the oil in the journal bearing is a source of heat contributing to the thermal load, and oil dispersed by the high speed of the bearing include micro-sized droplets which impact the density of the fluid surrounding the components, leading to increased drag. Journal bearing performance is complex because it is affected by many variables; speed of the component, the load on the bearing, materials, oil rheology, supply pressure, flow rate and surface roughness are some parameters which are considered. This further highlights the coupled nature of the hydrodynamic lubrication phenomena to wider domain, and therefore should be incorporated within numerical simulations to better optimise the system, in particular the supply conditions which are known to influence journal bearing performance (Costa *et al.*, 2003).

Computational hardware and numerical techniques have advanced significantly to develop the Navier-Stokes based computational fluid dynamics (CFD) numerical methodology. Models for turbulence, cavitation, multiphase flow and fluid rheology can be included in CFD frameworks to provide a detailed simulation of the flow behaviour. However, the geometric scale of hydrodynamic lubrication regimes and the high gradients of velocity and pressure generated require a highly refined mesh to resolve and, therefore, a very high computational cost. Accurate consideration of hydrodynamic lubrication effects is often excluded in simulations of high power transmission systems because of these computational challenges, however, given the examples previously outlined, the effects are influential on the systems efficiency. Developing more efficient thermal management systems will require these affects to be considered in simulations as they become more significant with increasing power density and, therefore,

greater thermal loads which future generations of aircraft propulsion will produce.

The study of hydrodynamic lubrication within the field of tribology has developed the Reynolds lubrication theory, based on the work of Reynolds (1886), which derives a simplified equation which governs hydrodynamic lubrication regimes. Further work included the effects of surface deformation, temperature and fluid rheology in the numerical model. The simplifications greatly reduce the computational load while maintaining a good quality solution which has been well validated against experimental results. Implementing the methodology within a CFD framework would allow the development of CFD simulations which incorporate the affects of hydrodynamic lubrication while maintaining a practical computational demand for designing more efficient thermal management systems and move toward the carbon emissions targets set in the aircraft industry.

1.2 Aims And Objectives

1.2.1 Aims

The aim of this work is to develop a numerical framework which interfaces solutions between the Reynolds based Thermal Elasto-Hydrodynamic Lubrication (TEHL) methodology with a Navier-Stokes CFD methodology. This will allow the scope of numerical simulations to be broadened beyond the domain of lubricated contacts and consider their effects in a system at an efficient computational cost.

1.2.2 Objectives

1. Formulate and implement a Reynolds based TEHL solver within OpenFOAM.
2. Validate the TEHL model against external experimental results from literature to verify the accuracy of implemented methodology.
3. Develop a coupling methodology between the TEHL and CFD methodologies to produce a continuous solution. This will provide the basis for simulations including and expanding beyond lubricated contacts.

4. Verify the coupling by validating against experimental results. This will give confidence in the accuracy of the coupling methodology.

1.3 Contribution to Knowledge and Publications

The present study attempts to address multiple gaps in literature and in doing so makes important contributions:

1. This research extends the hydrodynamic lubrication modelling methodology by coupling the model with CFD. This is the first study to consider coupling between Reynolds based lubrication modelling and CFD.

2. The interfacing between the lubrication model and CFD is investigated and validated. This novel investigation provides an initial framework for coupling the models in simulations.

3. This study implements the Reynolds based lubrication model within an open-source CFD software, OpenFOAM, using the finite-volume method which is detailed in Layton *et al.* (2023). While other studies have implemented the methodology in OpenFOAM, this study incorporates more physical behaviour including temperature and elastic deformation.

4. The implementation in OpenFOAM provides a flexible software which is capable for modelling cases beyond those investigated in this study.

Chapter 2

Literature Review

2.1 Introduction

The aim of this PhD is to develop a coupling methodology linking Reynolds based Thermal Elasto-Hydrodynamic Lubrication (TEHL) modelling with Navier-Stokes based Computational Fluid Dynamics (CFD). In this section, the research in the wider context of transmission systems is overviewed, focusing on features of the broader oil system that impact energy efficiency: gear windage and oil shedding, which high pressure lubricated contacts contribute to and would benefit from a TEHL-CFD coupled model. The background on high-pressure lubricated contacts research is reviewed and summarised to contextualise the current work. A key focus of the review is journal bearings which operate based on the hydrodynamic lubrication phenomena and are a significant component in aviation transmission. Previous modelling approaches and numerical methodologies applied to the hydrodynamic lubrication problem are described, with a particular focus on journal bearings.

2.2 Transmission Systems

The extreme power densities in high-power transmission systems produce significant thermal loads despite the high efficiency of the system. Much of this energy is lost in the form of heat and produces a thermal load which must be managed to prevent thermal related component

failure. Oil systems are used for cooling components within the transmission system and provide lubrication in the contact points to reduce friction between components and, therefore, the heat produced.

The presence of oil in the mechanical system leads to various mechanisms of power loss which are briefly overviewed here to contextualise the influences that are later discussed. Windage is a notable power loss mechanism where dissipated oil from mechanical components effects the aerodynamic properties and increases drag on rotating components (Eastwick & Johnson, 2008). Dawson (1984) experimentally studied windage power loss in spur gears, investigating the affects of geometry, speed size and shrouding. Their gears were operated within air and it is noted the observed power loss would be enhanced by the presence of oil in the atmosphere. The investigation in Diab *et al.* (2006) included windage power loss alongside gas trapping and tooth friction. This study found that for high speed and wide faced components the windage loss is prominent compared to the other sources considered. Oil shedding is another key feature in transmission systems which effects thermal and mechanical efficiency. Oil ejected towards the walls creates the potential for concentrations of heat in the system, and disintegration of the oil into the oil-air mixture influences the windage power loss (Eastwick & Johnson, 2008). Larsson *et al.* (1994) investigated the oil droplets produced by an elasto-hydrodynamic lubrication contact, finding that the droplet volume increased with the temperature, viscosity and surface velocity.

The oil dispersion from journal bearings is related to the fundamental shedding behaviour investigated in studies such as Glahn *et al.* (2002) which investigated the oil shedding behaviour from the rim of a rotating disk. The mechanisms for droplet disintegration were the same as rotary atomisers, however the transition points were different. The study produced a non-dimensionalised dataset for the fundamental droplet generation from a rotating disk, and using empirical correlations the disintegration mode can be estimated. The study demonstrates the variation in droplet size at difference disintegration mechanisms which will influence the wider system, and empirical estimations are limited in their accuracy. The requirements for accurately predicting flow from journal bearings is highlighted in Berthold *et al.* (2018) which applied a CFD model to simulate the side leakage from a planetary gearbox journal bearing. The ligament formation is observed in the numerical models and it is found that the oil vis-

cosity, which is significantly effected by temperature, profoundly affects the flow path of the oil. This demonstrates that an accurate prediction of the oil temperature exiting the journal bearing would significantly influence the predicted flow path and the disintegration mechanism. Therefore, the influence of heating in the bearing should be considered in the simulation methodology. The side flow from a journal bearing is further investigated in Berthold *et al.* (2019) which tested two numerical schemes for the multiphase flow interface reconstruction. In this study, the side flow from the journal bearing is calculated from a separate model applying a simplified methodology based on lubrication theory to generate a representative axial velocity profile. This approach provided an appropriate inlet condition for the CFD model and avoids CFD modelling of the journal bearings lubrication region, however the lubrication model is incomplete.

This overview of research related to transmission systems shows some of the flow properties which influence efficiency and are affected by the performance of lubricated contacts. The topic of lubricated contacts in the field of tribology is complex and broad, related to several mechanical components. The next section reviews studies broadly in the field of lubricated contacts.

2.3 Highly Loaded Lubricated Contacts

Highly loaded contacts within transmission systems, for example during the meshing cycles between gears and in the load bearing regions of bearings, are areas of extreme pressure where the energy is transferred between components in the system. Friction between components generates significant amounts of heat which is commonly managed using an oil lubrication system, reducing friction and cooling the components. The research relating to highly loaded contacts is driven to optimise designs of mechanical components and allow for greater loads and speeds in operation, higher efficiency, and reduced wear to maximise lifespan. The presence of the lubricant in high-power transmission means the contact regions are often operating in a hydrodynamic lubrication regime, where a film of oil is separating the interacting surfaces. This is desirable given the low friction and wear inherent to hydrodynamic lubrication regimes and many components benefit from this such as journal bearings and rolling elements bearings

(shown in Figure 2.1).

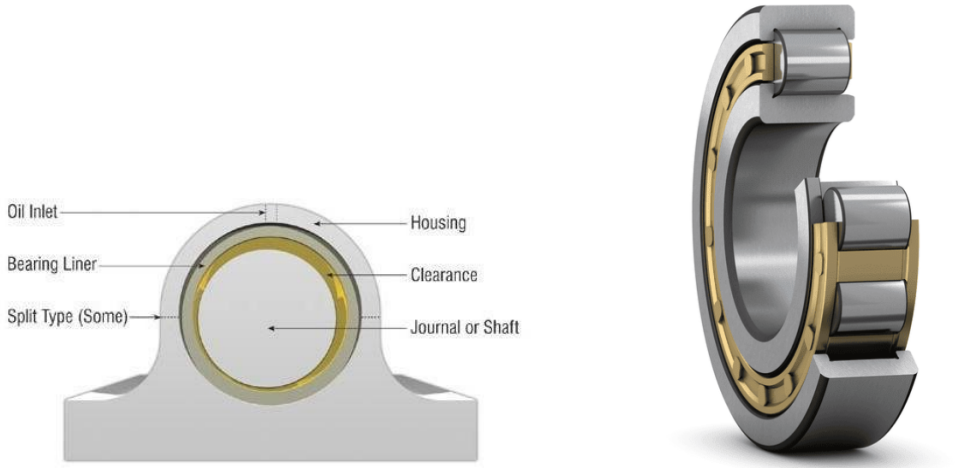

(a) Journal Bearing [Srinivas *et al.* (2015)] (b) Rolling Element Bearing [Cheng (1965)]

Figure 2.1: Examples of hydrodynamically lubricated transmission system components

A hydrodynamic lubrication regime generally identified based on the behaviour of the coefficient of friction (CoF) which varies as the hydrodynamic film forms and the regime of lubrication varies. Three-regimes of lubrication are generally identified depending on the level of separation between the surfaces and their respective roughness relating to the size of the surface asperities; boundary lubrication where the surfaces are in direct contact, mixed lubrication where some contact between asperities is present and full film lubrication where the surfaces are completely separated by a lubricating fluid film. The work of Stribeck (1901, 1902) and Hersey (1914) identified the relationship between coefficient of friction and the non-dimensional Hersey number, Equation 2.1, which links the dynamic viscosity, μ, rotational speed, N, and normal load, W, identifying these as key parameters influencing the regime of lubrication:

$$He = \frac{\mu N}{W} \tag{2.1}$$

The non-linear behaviour is seen in the Stribeck curve depicted in Figure 2.2 which clearly shows the three regimes of lubrication. Understandably, the CoF within the boundary regime is determined by material properties of the surfaces in contact. The mixed lubrication regime categorises the significant decrease in friction as the surfaces become separated until the full

hydrodynamic lubrication regime forms where the CoF follows a linear behaviour that attributes to the viscous forces within the fluid.

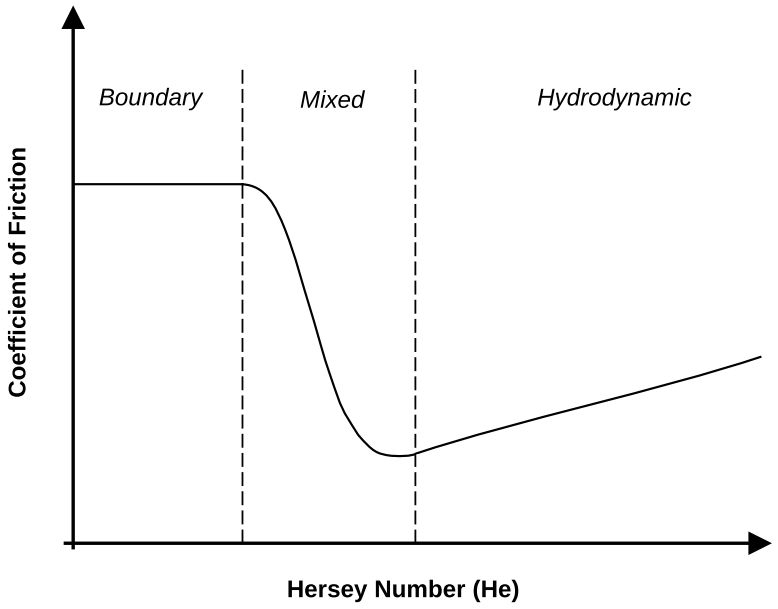

Figure 2.2: The Stribeck Curve (Stribeck, 1901, 1902)

Friction is a key factor which is influential to wear and efficiency and is therefore the focus of many research papers such as Sander *et al.* (2014) which analysed the effects of high pressure and shear thinning on friction with experimental and simulation methods. The friction in hydrodynamic regions can vary during operation, as seen in Bouyer & Fillon (2011) where the friction within a journal bearing is experimentally measured during start-up which showed the variation during this time frame. Lu & Khonsari (2005) investigated the lift-off speed in journal bearings, where the hydrodynamic film becomes fully formed, under different normal loads and inlet temperatures. The results showed that increasing the load increased the lift-off speed of the bearing, however at low load the lift-off speed was approximately equal. Oil temperature was shown to increase the lift off speed and reduce the coefficient of friction when a hydrodynamic lubrication regime is achieved. The inlet temperature effects can be attributed to the change in fluid viscosity at different temperatures. The observed influence on the bearings lubrication performance highlights the importance of the inlet temperature on the lubrication behaviour.

Thermal effects in bearings become more significant as the rotational speed and load increases

due to the greater shearing of the fluid generating more heat (Szeri, 2010). Maximum temperatures in the solid components is a key parameter to predict as it is a significant failure mechanism in transmission components (Khonsari, 1987). Thermal effects are investigated experimentally in Ma & Taylor (1996) in circular and elliptical journal bearings with particular interest in the effect on power loss, which noted the thermal behaviour was significantly affected by the rotational speed. Furthermore, the speed effected the maximum bearing temperature and the power loss, showing the thermal effects become more significant at greater rotational speeds.

2.4 Experimental Investigations Of Hydrodynamic Lubrication

Investigation of TEHL regimes are experimentally challenging due to the extreme conditions within the regions, often reaching pressure ranges in the GPa order, variations of temperature up to $100°C$ and with film thicknesses at micron scale (Albahrani *et al.*, 2016). Experimental investigations are highly valuable for producing validation data for numerical models. This section overviews some of the physical techniques developed for analysing the flow in TEHL regimes and experimental investigations of systems operating under hydrodynamic lubrication.

2.4.1 In-Situ Measuring Techniques Of Film Thickness

The distance between the surfaces in the contact region is a primary variable in experimental investigations as it relates to the regime of lubrication previously highlighted in Section 2.3. This distance is referred to as the film thickness when a fluid film is separating the surfaces. Much of the challenge in film thickness measurements is due to the small scale of the domain and that devices placed within the region will significantly impede the flow. Indirect in-situ approaches are, therefore, highly valuable in this context and generally make use of signaling approaches which are non-destructive to the film.

Electrical methods were some of the first techniques to be applied to measure film thickness in TEHL regimes. The electrical resistance between two gears was used to measure the film

thickness in Lane *et al.* (1952). The non-linear relation between resistance and film thickness creates difficulty in the calibration, which is generally the challenge inherent to electrical methods. The method developed by Crook (1961) and Dyson *et al.* (1965) used capacitance between the separated bodies to measure the film thickness. Ibrahim (1962) used a discharge-voltage method in studies of the scuffing between gears. A high current is passed through the film and the subsequent voltage is measured to estimate the film thickness from the apparent increase in resistance compared to when the surfaces are in contact. The capacitance and discharge voltage methods are compared in Dyson (1966), finding the relation between film thickness and voltage discharge is highly non-linear. The calibration challenges and often non-linear relations between the experimental method and the film thickness are disadvantages to electrical methods, which were later replaced with the development of optical methods.

Optical methods are another basis for film thickness measurements widely applied to hydrodynamic lubrication regimes. X-rays were first used by Sibley & Orcutt (1961) to measure the thickness of oil films between two rollers. Kirk M. T. (1962) developed an optical interferometry method which uses the constructive-destructive interference of light to image the oil film. Infrared techniques are also investigated such as in Lauer & Peterkin (1975) and are used to map the temperature field in the film in Turchine *et al.* (1974). A method based on fluorescence was first used in Smart & Ford (1974). Particle image velocimetry (PIV) is an optical technique using particulates in the fluid to visualise the flow. PIV has been used in Bair *et al.* (1993) to observe the shearing within the lubricant. Later, Horvat & Braun (2011) applied a PIV method in a numerical and experimental investigation of hydrostatic bearings. The general disadvantage of optical methods is the requirement for a transparent material in one of the components to allow light access to the contact region. This limits the ability to study TEHL contacts using realistic materials as the transparent materials will have difference elastic and thermal properties, influencing the lubrication behaviour in the region.

In the 21st century, acoustic methods began to emerge for film thickness measurements in hydrodynamic lubrication regimes which are advantageous over optical methods for not requiring transparent materials. Dwyer-Joyce *et al.* (2003) first used ultrasound for the measurement of the oil film thickness in a sliding ball and flat surface contact. In the original experiment, the film thickness measurements recorded were in the range of 50-500nm, which agreed with

previous studies and validated the methodology. The operating limits where later identified in Dwyer-Joyce *et al.* (2004) for the ultrasonic method. The methodology was further developed towards measuring the viscosity within the lubricating film in Kasolang *et al.* (2011) and in Schirru *et al.* (2018).

In-situ measurement of the film thickness is a challenging aspect to experimental investigations of lubricated contacts and many innovative methods have been developed for capturing this feature. Ongoing development and application of methods such as the acoustic method using ultrasonic signals, provides excellent validation data for numerical models to progress.

2.4.2 Experimental Investigations

Many experimental investigations in literature do not incorporate advanced film thickness measurements in their methodology because of the challenging nature and primarily consider the pressure and temperature fields. Ferron *et al.* (1983) develops an experimental apparatus of a single axially grooved journal bearing, as shown in Figure 2.3, with capability to measure pressure along the centreline of the film and temperature with the bush. They compare the experimental results with a numerical model which showed good correlations between the pressure and temperature profiles. The experimental rig is later adapted in Bouyer & Fillon (2002) to investigate the effect of misalignment of the shaft on the temperature profile. In their results, the misalignment effected the oil flow rate and was more influenced at low load and speed. Misalignment is also investigated in Pierre *et al.* (2004) which compared the temperature fields of a numerical model with experimental results of a journal bearing. Ma & Taylor (1996) investigated the thermal effects in a plain and an elliptical journal bearing. Their results showed the significant effect of the rotational speed on increasing the maximum bush temperature, power loss and flow rate. The temperature distribution is observed as being predominant in the circumferential direction compared to the axial. The effect of thermal deformation has been presented in Zhang *et al.* (2000) where thermal expansion of the solid regions is predicted in the order of $10\mu m$ and shown to improve the temperature profile prediction when the deformation is considered. Kasolang *et al.* (2013) uses the ultrasonic method used in Dwyer-Joyce *et al.* (2003) to measure the film thickness and viscosity profiles in a journal bearing. The location of the cavitation region is also estimated using the disruption to the ultrasonic wave

caused by the multi-phase flow.

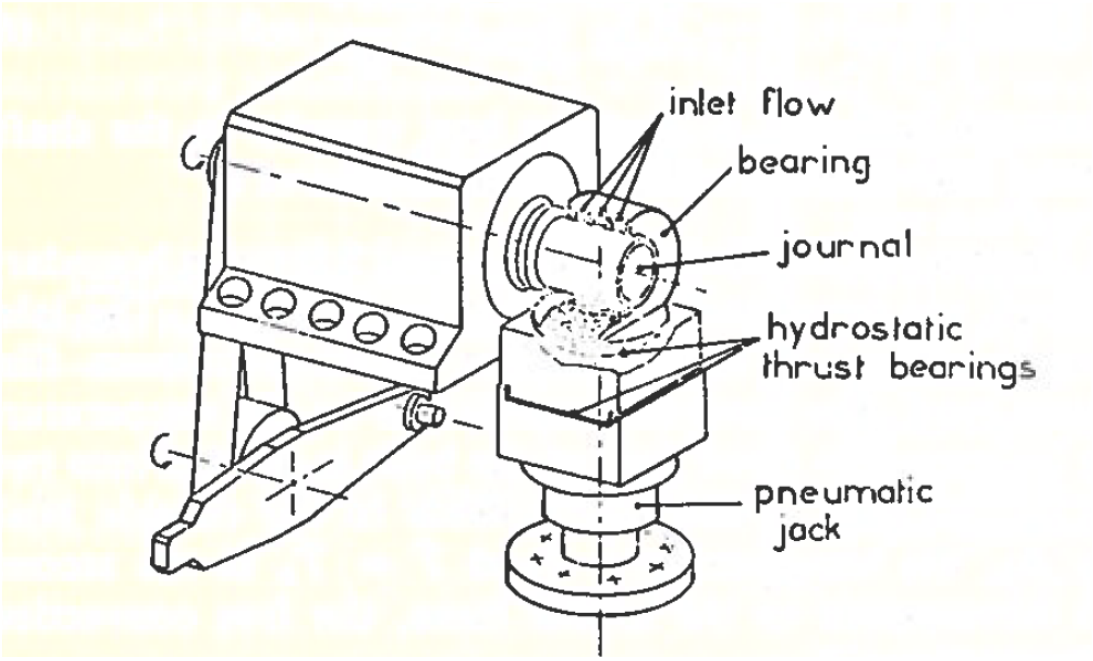

Figure 2.3: Experimental journal bearing apparatus from Ferron *et al.* (1983)

Bouyer & Fillon (2011) investigated the start-up friction torque of a journal bearing and found surface finish and oil supply temperature were influential factors. Sander *et al.* (2014) used data from an experimental journal bearing rig to validate a numerical model which considers piezo viscous and shear thinning effects. The results show that a complete rheological model of the lubricant is required for close agreement with the experimental results, showcasing the influence of the lubricant properties on the lubrication performance. Ahmad *et al.* (2014) experimentally tested the affect of the groove location on a journal bearing. The results showed the pressure profile is significantly effected by the location of the groove and temperature tends to decrease when the groove is located in the converging region of the geometry, highlighting the significant affect the groove has on the lubrication performance in a journal bearing. Lu & Khonsari (2005) investigated the lift-off speed in journal bearings, where the hydrodynamic film becomes fully formed, with varying inlet temperature and load.

This section summarises experimental studies for journal bearings which provide the necessary validation data for numerical models. In many of the studies the influence of the groove region is noted and that many factors including inlet temperature, misalignment and lubricant rheology influence the lubrication and thermal performance of the bearing. The multiple

variables influencing the lubrication performance that are external to the domain highlight the requirement for accurate boundary condition prediction for the lubrication domain.

2.5 Reynolds Based Lubrication Modelling

The Reynolds's based lubrication methodology is a modelling approach within tribology which uses the thin-film assumptions to generate a system of equations for approximating hydrodynamic lubrication regimes. The methodology is renowned for a low computational demand while maintaining a good level of accuracy in the solution. Significant development throughout the 20th Century incorporated temperature, deformation, cavitation and variable fluid rheology in the model, which remains highly attractive due to its practical efficiency. This section covers the development of the Reynolds based TEHL methodology.

2.5.1 Reynolds Equation

The field of hydrodynamic lubrication simulation in tribology began with the derivation of the Reynolds equation in the influential work of Reynolds (1886) which uses the equations for viscous stress in a fluid in motion to derive an equation for the pressure in a lubrication film between two bodies in relative motion operating in a hydrodynamic lubrication regime. The theory assumes the space between the surfaces is small enough to prevent eddy formation (i.e. laminar), inertial forces are negligible compared to the internal stresses, viscosity of the fluid is effectively constant, curvature can be disregarded due to the difference between the radii of the bodies and the thickness of the film, and the velocity gradient across thickness of the film is dominant compared to the other directions.

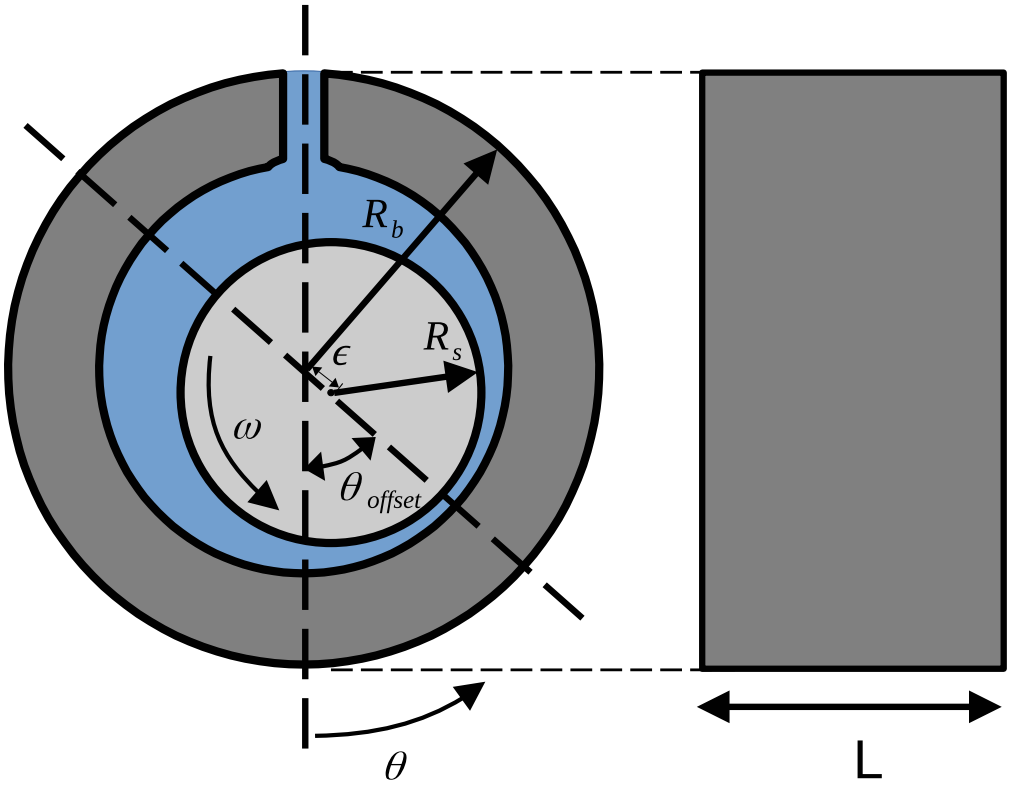

Figure 2.4: Journal Bearing Geometry

The first analytical solution of the Reynolds equation came in the form of the short and long bearing theories where the applicability of each assumption is dependent on the length-to-diameter ratio $\left(\frac{L}{D}\right)$ of the bearing using the shaft diameter and the bush length, as shown in Figure 2.4. In the short bearing theory, where $L << D$, the bearing is treated with infinitesimally small length, determining that the pressure gradient axially is dominant over the circumferential gradient, thereby, the circumferential gradient is removed from the equation. In the case of a long bearing, where $L >> D$, the length is assumed infinite and the pressure gradient axially in the film tends to zero, thereby, the axial gradient term is removed. The short and long bearing assumptions are unsuitable for real component design where the limiting values for $\frac{L}{D}$ are approximately in range of < 0.5 and > 2 respectively, therefore, numerical solutions for the Reynolds equation have been pursued following the work of Reynolds (1886).

2.5.2 Cavitation

The converging-diverging geometry of a hydrodynamic lubrication region is shown in Figure 2.5, where the top surface in motion is driving the fluid into a smaller gap, generating the pressure field which carries the load on the contact. The diverging region develops a low pressure in the fluid which can cause the film to rupture in the form of cavitation. This is generally by either two mechanisms; gaseous cavitation, where dissolved gases are liberated from the fluid to form bubbles, and vapor cavitation where the lubricant will boil if the pressure falls below the fluids vapor pressure (Dowson & Taylor, 1979).

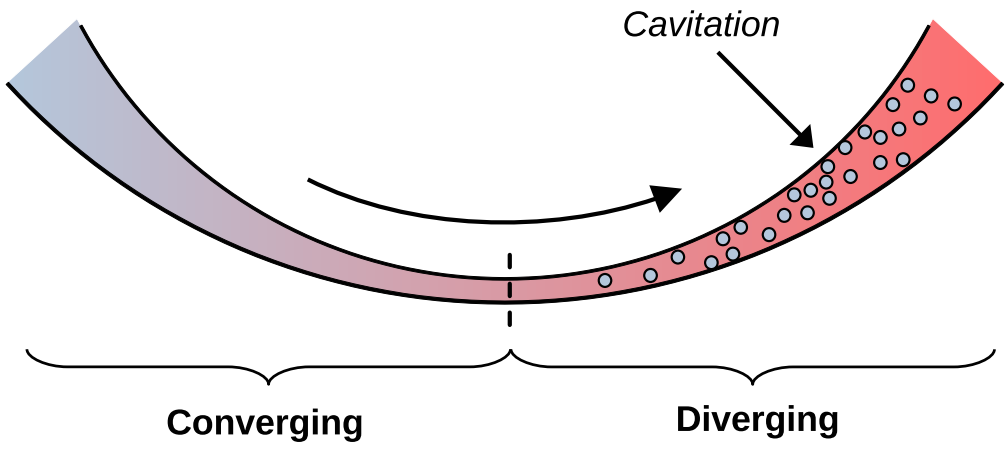

Figure 2.5: Hydrodynamic lubrication converging-diverging gap

The first model for the cavitation phenomena was the half-Sommerfeld boundary condition described by Gumbel (1921). The approach limits the pressure field to a minimum value which reflects the constant pressure field observed in the region. The minimum condition is applied after the solution of the Reynolds equation is found, thereby removing continuity from the solution which is a notable inconsistency in the approach. While the condition does not consider the cavitation phenomena as a physical mechanism, rather a limitation on the pressure, the methodology was attractive for its simplicity. A more accurate consideration of cavitation was seen in the Reynolds boundary condition first formulated by Swift (1931) and Stieber (1933) which argued that the pressure gradient at the film rupture boundary is zero.

Cameron & Wood (1949) applied the Reynolds boundary condition to the finite and infinite journal bearings, correlating with experimental results to show the condition is applicable. Floberg (1974), Jakobsson & Floberg (1957) and Olsson (1965) derived what is summarised as the Jakobsson-Floberg-Olsson (JFO) cavitation theory which draws a distinction between two regions in the lubricating film; the complete film region where the Reynolds equation applies, and the cavitation region where tensile stresses in the fluid rupture the film and only part of the cavity consists of fluid. Considering mass conservation and striation flow in the cavitation region, therefore, requires the pressure value and gradient to be zero, defining the JFO boundary conditions for cavitation.

Elrod & Adam M. L. (1974) developed a generalised form of the Reynolds equation which applies universally to the lubricating film by incorporating a switch function to implement the JFO conditions and was then reduced in complexity in Elrod (1981). Vijayaraghavan & Keith (1989) built on the Elrod-Adam (EA) algorithm by automatically switching the discretisation scheme of the advective term between first and second order in the cavitation and non-cavitation regions respectively. This allowed a second-order solution to be found in the non-cavitation region while a first-order upwind scheme could be applied in the cavitation region for numerical stability due to the equation reducing to hyperbolic form. Brewe (1986) numerically investigated a submerged dynamically loaded journal bearing using a conservative method based on the Elrod algorithm to consider cavitation. Kumar & Booker (1991) introduced a finite element cavitation algorithm similar to Elrod & Adam M. L. (1974) except assuming incompressible fluid in the full film region. The simplicity and accuracy of the Elrod-Adams approach remains attractive for numerical models, however, the stiffness in the resulting coefficient matrix is an important convergence factor and for practicality, a lower than physical fluid bulk modulus is generally employed to improve convergence properties.

Alternative approaches to cavitation in hydrodynamic lubrication generally incorporate a fluid-state model which responds to the pressure field. Bayada & Chupin (2013) incorporates a pressure-density model which varies the bulk modulus in the governing Reynolds equation to account for cavitation of the fluid. Van Odyck & Venner (2003) assumes Stokes flow in the film which neglects inertia from the Navier-Stokes equations and describe a pressure-density relation to model the cavitation phenomena. De Boer & Dowson (2018) applies a

Lagrangian-Eulerian methodology for modelling the cavitation phenomena in an EHL line contact. Ransegnola *et al.* (2021) develops a fluid-state model considering both gaseous and vaporous cavitation for a more complex consideration of the phenomena. These approaches can require more material information on the lubricating fluid to model the pressure-density relation, however they avoid the switch function inherent to Elrod based algorithms. Palavecino *et al.* (2024) develops a conservative two-phase model for cavitation of hydrodynamic lubrication regimes using the Rayleigh–Plesset equation. The method can describe vaporous and gaseous cavitation in the fluid, and the results compared well with experimental results visualising the cavitation region.

Fluid Rheology approaches often require more details on the fluid properties across a range of pressures and the properties in the cavitation region. This information is often not available in literature which commonly only states the cavitation pressure. The Elrod-Adam cavitation model is used in the current study because the cavitation pressure is often quoted in experimental studies while further detail to define a complete fluid model is generally excluded. The Elrod-Adam cavitation model is well validated and applied in several numerical studies and is mass-conserving which is sufficient for the scope of this study.

2.5.3 Elastic Deformation

Dowson & Higginson (1959) were the first to include the deformation affects in hydrodynamic lubrication which incorporated elasticity of the solid regions to produce a coupled pressure-deformation solver. This regime became known as elasto-hydrodynamic lubrication where deformation of the solids is significant enough to influence the numerical solution. The half-space approximation from Hertz (1881) is a common model for the elastic deformation in EHL regimes. The half-space model assumes the deformation is a superposition of hertzian contacts to derive an equation which integrates the pressure field and has been applied in studies such as Dobrica *et al.* (2006) and Ma *et al.* (2022). The equation has a complexity of $O(n^2)$ due to the embedded integral which elevates the computational requirement. Several numerical setups are investigated in Meng & Chen (2015) including a finite-element method, the half-space hypothesis and an influence coefficient method. The study found there was greater discrepancies between the methods at higher length-diameter ratios, high eccentrici-

ties, high rotational speeds, and high viscosity in the lubricant. Full elastic system approaches for the solid deformation have been applied in Habchi *et al.* (2008a) and Habchi (2014) using finite-element methods (FEM) in the solid region and coupled to the fluid through a fluid-solid interaction (FSI) methodology. FEM methods applied in the solid regions will provide the highest accuracy result for the deformation as they directly incorporate the elastic properties of the material, however have a greater computational load. In this study the half-space approximation is used to avoid developing an FSI methodology between the film and solid regions which is beyond the scope of this research which focuses on the interfacing with CFD.

2.5.4 Thermal Effects

Thermal effects are an important aspect in hydrodynamic lubrication regime in modern industry as highlighted in Chapter 1. The significant velocity gradients in hydrodynamic lubrication regions generate heat by viscous dissipation, creating a non-uniform temperature field across the lubricating film. Heat is also generated by compression of the fluid, although is less influential compared to shearing effects. Energy equations are incorporated into the numerical methodology to include the effects from the temperature rise in the fluid which affect the properties of the fluid. Cheng (1965) was among the first to investigate the thermal effects in hydrodynamic lubrication, using a two dimensional finite-difference method to find a solution. The results showed the influence on the pressure and film profile, and the significant influence on the frictional force, showing the necessity to consider temperature in the numerical model. Dowson & Whitaker (1965) also investigated the thermal effects on sliding and rolling contacts, applying an energy equation in the fluid and using a finite-element discretisation scheme.

Kim *et al.* (2001) reduces the energy equation to a two-dimensional form neglecting the flow direction normal to the surfaces and assuming a parabolic profile across the film height. A similar approach is taken in Stefani & Rebora (2009) which assumes a fourth-order polynomial temperature profile across the film height and is incorporated into the energy equation. Chen *et al.* (2018) also uses a semi-analytical approach in the temperature solution where a second order polynomial model is used as an assumed temperature profile. The semi-analytical approaches improve the simulation speed as the energy equation is simplified to a two-dimensional form, however they require an assumed temperature profile which may not

reflect the true temperature distribution. Three-dimensional energy equations have been incorporated in studies such as Guo *et al.* (2001) which solved the three-dimensional energy equation in a high slide-roll ratio case.

Bouyer & Fillon (2004) includes the energy equation in a numerical model to investigate the effect of thermal and elastic deformation on the solution for a journal bearing with a shaft speed of 3000rpm and load 150kN, developing eccentricities > 0.9. The results show the thermal effects have a strong influence on film thickness and maximum pressure, highlighting the need to include the energy equation at more severe operating conditions. Figure 2.6 shows a comparison of the pressure profiles when deformation and thermal effects are excluded or included in the numerical model.

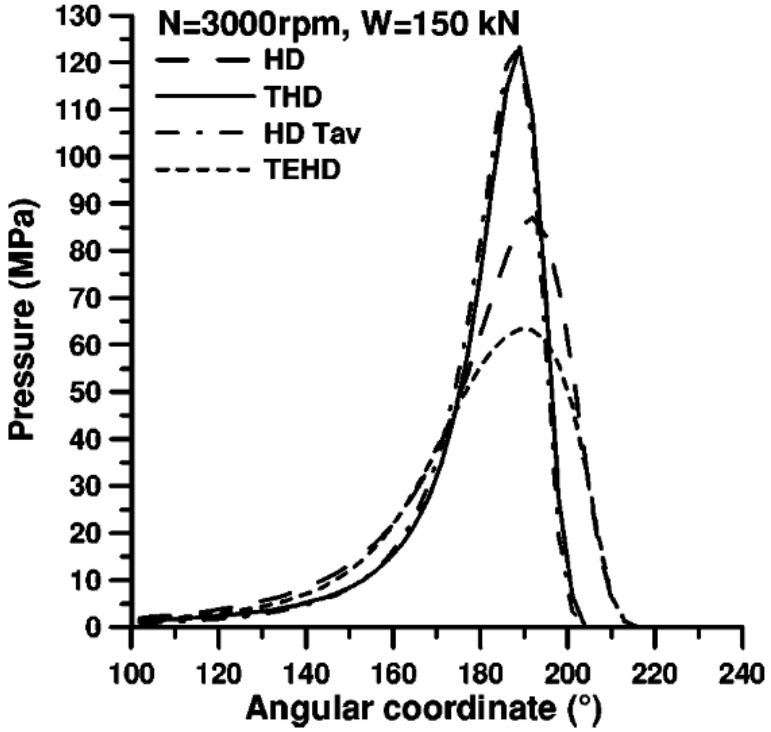

Figure 2.6: Comparison of pressure profiles for isothermal hydrodynamic simulation (HD), thermohydrodynamic simulation (THD), isothermal at an average temperature (HD Tav) and thermo-elastohydrodynamic simulation from Bouyer & Fillon (2004)

Pierre *et al.* (2004) develops a three-dimensional thermo-hydrodynamic numerical model incorporating the Elrod-Adams cavitation algorithm for a misaligned journal bearing, comparing with experimental results. Temperature dependence of viscosity is considered and the study describes the methodology for varying the fluid rheology using the results of the Elrod-Adams

cavitation model.

The shear heating term is the primary heat source in the energy equation of TEHL models seen in literature. In sufficiently high pressure cases, an additional compressive heat term is often included based on the work done on the fluid. Habchi *et al.* (2008b) develops a TEHL model for Newtonian and non-Newtonian lubrication, also incorporating the compressive heating term which is shown to be less significant than the shear heating source. The compressibility heat effect is also included in the energy equation from Ardah *et al.* (2023) along with the shear heating term and the heat capacity heating and cooling effects. Compressibility heating is generally seen in cases where the pressure reaches the order of 0.1GPa and excluded beneath this magnitude. The magnitudes of pressure in the studies investigated in this thesis are below this magnitude, in the order of 0.01GPa, and therefore these effects will be excluded with the aim to improve stability of the numerical solver.

Various forms of the energy equation are presented in literature and the temperature effects are shown to significantly effect the solution. From this review the energy equation in a three-dimensional form is preferred to accurately account for the temperature distribution across the height of the film. The shear heating term is the notable heat source in the equation and is dominant in cases with lower pressure gradients.

2.5.5 Fluid Rheology

2.5.5.1 Viscosity

Viscosity is a significant material property which affects the behaviour of hydrodynamic lubrication regimes, and conditions in these regions are significant enough to vary the properties throughout the domain. The heat generated in highly shearing TEHL regimes causes a decrease in viscosity of the lubricant due to the increase in temperature. Power law models are commonly used to model the temperature dependence of viscosity. The Roelands model from Roelands (1966) introduces pressure affects into the viscosity model alongside temperature. The pressure-viscosity model from Barus (1893) is relatively simple, using a power law function requiring only single coefficient to characterise the pressure-viscosity relationship.

However, this model notably becomes inaccurate with increasing pressure. Yasutomi *et al.* (1984) presents a temperature-viscosity relation base on free volume theory. These viscosity models are compared for various lubricant oils in Sadinski & Doll (2021) which presents the performance of the models across a range of temperature, pressure and shear rates. Similar agreement to the experimental measurements is shown across the temperature range and pressure effects are shown the become significant in the GPa order. Given the similarity across the temperature range and at low pressure, the exponential models are preferred given their simplicity to implement.

2.5.5.2 Density

The high pressure magnitudes which develop in TEHL regimes are sufficient for the incompressible assumption to be inaccurate. Compressibility of fluid is generally linear up to a compression of approximately 35% (Lugt & Morales-Espejel, 2011). A pressure density model was presented in Dowson & Higginson (1966) for the pressure ranges in EHL regimes. Density of the fluid is often linked the the cavitation phenomena such as in the classic Elrod-Adams (Elrod & Adam M. L., 1974) model for cavitation which applies a logarithmic pressure-density function bases on a value of compressibility of the fluid.

The Elrod-Adams algorithm is preferred as the cavitation model because the required information on the fluids rheology is minimal. Therefore, the logarithmic function will be used for the pressure-density relation in this study.

2.5.5.3 Thermodynamic Material Properties

A factor affecting the thermodynamic properties of the lubricating fluid is caused by the cavitation phenomena creating a multiphase flow in the lubricated contact region. In Ardah *et al.* (2023) the lubricant material properties which include the density, viscosity, specific heat capacity and thermal conductivity, are modified with a liquid-gas mixture model, deriving an effective constant value for the film based on the volumetric ratios of each phase. Pierre *et al.* (2004) uses a similar approach but uses the mass ratio between phases for the specific heat capacity. Larsson & Andersson (2000) included a pressure dependent thermal conductivity

model and pressure-temperature dependent specific heat capacity model. The variability of specific heat capacity and thermal conductivity is insignificant below the GPa range and can be neglected below this order.

2.5.6 Numerical Techniques

Various numerical techniques have been used to obtain solutions to the TEHL problem. Hamrock & Dowson (1976a), Hamrock & Dowson (1976b) and Hamrock & Dowson (1977) produced the first numerical results for EHL simulation using a Gauss-Seidel iteration methodology. Lubrecht *et al.* (1987) introduced multigrid techniques to enhance the computational speed of the EHL numerical model which are also applied in Venner (1991). Okamura (1993) used a Newton-Raphson approach which showed faster computing speed. Ardah *et al.* (2023) developed a finite-volume framework for a TEHL methodology, thereby incorporating the conservative properties of the finite-volume method to improve over finite-difference approaches. Škurić *et al.* (2019) used a finite area approach in OpenFOAM for the Reynolds equation. Giacopini *et al.* (2010) develops a new complementarity based mass-conserving formulation of the Reynolds equation. The conservative properties are a key advantage of the finite-volume discretisation method and is also used in CFD methodology and, therefore, would be an appropriate method to use in the coupling methodology.

2.6 CFD Modelling Of Hydrodynamic Lubrication

Advancing computational technology has given opportunity for finite-volume Navier-Stokes based methodologies to be applied to hydrodynamic lubrication regimes. Almqvist & Larsson (2002) were among the first to apply a CFD model to an EHL regime up to contact pressure of 0.7GPa. They note the high computational cost of the approach which requires small under-relaxation factors for convergence, where the solution is explicitly reduced between iterations. The under-relaxation provides the required stability, however, it slows the convergence and further increases the computational time of the simulation. Moreover, a CFD approach enlarges the problem as four equations must be solved for 3D cases to obtain a solution for pressure compared to one equation for the Reynolds approach. The agreement between CFD

and Reynolds based methodologies is shown in Almqvist *et al.* (2004) for EHL line contacts and found very small deviations between the solutions. While more computationally intensive, CFD models allow greater flexibility for modifying lubricant rheology and simulating more complexity in the flow, particularly the reformation process and starvation at the inlet. Finite-element based methods have also been investigated in Bruyere *et al.* (2012) to model a thermal elastohydrodynamic line contact. A direct coupling methodology is applied where the equations are combined into a single non-linear system, therefore requiring fewer iterations compared to sequential numerical procedures. Each iteration required approximately 10mins.

The fundamental advantage to CFD approaches is the potential to incorporate more physically representative models in the lubrication domain. Many investigations aim to expand the methodologies such as Hartinger *et al.* (2008) uses a CFD model for a hydrodynamic lubrication regime within a 2D rolling contact which includes shear thinning, elastic deformation and thermal effects. Fluid-Solid Interfacing models are presented in Hajishafiee *et al.* (2017) which uses OpenFOAM to simulate an EHL regime relating to rolling element bearings. The model considers a 2D geometry with compressibility, lubricant rheology, cavitation and thermal effects included. A wide range of physical phenomena is captured at the expense of a large computational cost where approximately 20 days were required to reach a solution. Bruyere *et al.* (2017) uses a two-phase model to simulate the cavitation phenomena at the outlet and capture the recirculating flows in the region. Hartinger & Reddyhoff (2018) compared CFD predictions of an EHL line contact considering thermal effects with experimental measurements of surface temperature and friction. Tošić *et al.* (2019) developed a CFD model for TEHL in a line contact and compared the solutions from using two combinations of models and showed the thermal conditions are affected by the rheological model used at high pressures of the order 1GPa. Martin *et al.* (2024) applies a full 3D CFD methodology to simulate a journal bearing including multi-phase effects. The results provide a detailed physical prediction of the lubricant flow, however required approximately 34 days to reach convergence on 36 CPU cores.

Singh *et al.* (2021) developed a fluid-solid interaction model for an EHL line contact in ANSYS FLUENT similar to Hajishafiee *et al.* (2017), connecting a CFD model with an elastic solid model to couple the deformation field. The model considered mass transfer between

liquid and vapor phases, compressibility and non-Newtonian rheology, and included a load balancing algorithm with a dynamic meshing method. They saw a significant reduction in computation time by using alternate numerical methods requiring fewer elements and iterations. The advantage of CFD is noted where the model is not confined to the contact region, allowing more accurate solutions through FSI and cavitation models, although at a higher computational cost. The greater physical accuracy of CFD approaches is also applicable for validation of TEHL models, such as in the study by Havaej *et al.* (2023) which compared the affect of different constitutive models for lubricant behaviour on TEHL simulations using a CFD approach.

Recently, CFD methods have been applied to journal bearings which apply more complex multiphase methodologies compared to Reynolds based models. In Song & Gu (2015) a numerical model of a journal bearing is presented which includes cavitation as a bubbly flow using the Reyleigh-Plesset equation. The complex geometry and flow within the groove is considered within the model allowing the flow details such as recirculating flow in the groove to be investigated. Furthermore, they consider conjugate heat transfer with the bush which is also described in the numerical model in Li *et al.* (2019). A multiphase model is also incorporated in Dhande & Pande (2018) and Dhande & Pande (2017), where the latter includes an FSI model to account for elastic deformation. A similar FSI approach is taken in Chen *et al.* (2019). The flexibility of CFD techniques to investigate flow details around complex features is highlighted in Chen *et al.* (2019) which investigated the affect of various groove arrangements in a journal bearing.

CFD approaches to TEHL regimes incorporate many of the physics of the region and accurately resolve the velocity-pressure fields which are simplified in the Reynolds based models. The primary disadvantages is the computational load inherent to the models because of the high mesh refinement required, more equations governing the domain and large number of iterations to reach a solution. The reduced computational time is the notable advantage to using the simplified Reynolds based methodology and is the primary motivation for incorporating this approach into a CFD framework.

2.7 Summary

Thermal elastohydrodynamic lubrication is an important factor to the operation of high power transmission systems, greatly influencing the energy efficiency, thermal performance and component lifetime. The high energy density of the contact regions is a significant source of heat in the thermal system and the outflow from these regions is affected by several factor in the contact region; the pressure field, fluid cavitation and the temperature variation. Fluid exiting these lubrication regions is influential to the wider system, relating to heat generation, windage power loss and oil pooling.

A wide array of experimental and numerical research has developed a comprehensive understanding of hydrodynamic lubrication regimes with exceptional modelling capability. Numerical methodologies in the field could be broadly categorised between two types: Reynolds based approaches which apply the equation from Reynolds (1886), and CFD approaches based on the Navier-Stokes equations applicable to all fluid dynamics problems. The Reynolds based methodologies remain highly attractive for their computational efficiency compared with CFD models of TEHL regimes, while maintaining acceptable accuracy.

A computationally efficient simulation setup for transmission system scenarios which contain TEHL regions would therefore incorporate a low demanding Reynolds based methodology in the lubricated contact, while applying the general CFD methodology on the wider domain with a coupling methodology applied to generate a solution to the full transmission system. This approach would be a novel implementation of the Reynolds based lubrication methodology as numerical studies generally apply fixed or approximated conditions to the boundaries of the lubrication domain. Furthermore, coupling the methodologies introduces the advantages of the lubrication model to improve CFD models of lubricated systems.

Chapter 3

Film Model And Validation

In this section, the lubrication model for hydrodynamic regimes and its implementation in OpenFOAM is described. The boundary conditions for each variable are given with justifications for the setup. Mesh sensitivity of the model is investigated using a simplified geometry to explore different aspects and their effect on the solution. The numerical model is validated against experimental results from literature of a single axial groove journal bearing from Ferron *et al.* (1983). This case is selected as the study provides a detailed account of the experimental setup and a broad experimental parameter range to validate the numerical model.

3.1 Governing Equations

In this section, the governing equations for the lubrication model are presented with descriptions of their assumptions and formulation. The mathematical model for the solid region is also presented which is included in a coupled numerical model in following sections to build a lubrication model within OpenFOAM.

3.1.1 Hydrodynamic Lubrication Region

This section presented the lubrication modeling methodology and the governing equations applied in the numerical model. Firstly, the foundational Reynolds Equation from Reynolds

(1886) for lubrication theory is presented before describing the cavitation modeling algorithm. The equation for deformation, temperature and fluid properties are then presented to build the full mathematical model for hydrodyanmic lubrication to be implemented in OpenFOAM.

3.1.1.1 Reynolds Equation

Hydrodynamic lubrication requires a characteristic wedge type geometry as shown in Figure 3.1 where the lubricating fluid is driven into a converging gap that develops a pressure in the fluid which causes surface to separate. A coordinate system is applied relative to the surfaces as shown in Figure 3.1, where x' is parallel to the converging direction, y' is perpendicular to the surfaces and z' is the direction perpendicular to x' and y'.

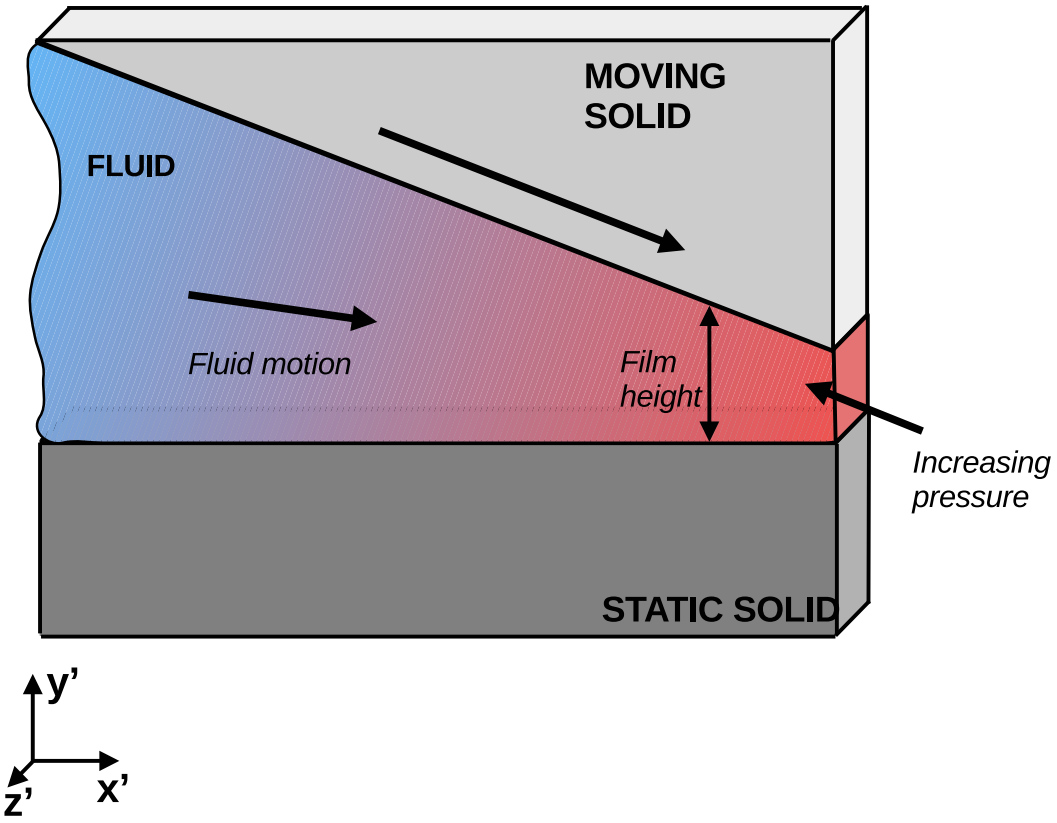

Figure 3.1: Schematic of the coordinate system for Reynolds Equation (Equation 3.1)

This height of the wedge formed in hydrodynamic lubrication is generally in the order of microns, and given this thin geometry several assumptions can be made for the flow in the regime which were original proposed by Reynolds (1886):

- The height of the film is sufficiently small to assume only laminar flow occurs in the film
- Pressure variation across the film height is negligible $\left(\frac{\partial P}{\partial y'} = 0\right)$
- Curvature effects are insignificant due to the large difference in scale between the surface radius and the film height $(h << R)$
- Forces from weight and inertia are insignificant compared with the forces arising from viscous stresses
- Fluid compressibility and variations in viscosity are insignificant

Applying these assumptions to the Navier-Stokes equation governing the behaviour of a viscous fluid, the Reynolds equation (Reynolds, 1886) is derived for thin film lubrication regimes:

$$\frac{\partial}{\partial x'}\left(\frac{\rho h^3}{12\mu}\frac{\partial P}{\partial x'}\right) + \frac{\partial}{\partial z'}\left(\frac{\rho h^3}{12\mu}\frac{\partial P}{\partial z'}\right) = \frac{\partial}{\partial x'}(\rho U h) \tag{3.1}$$

where U is the average speed of the adjacent surfaces, ρ is the fluid density, μ is the fluid dynamic viscosity, h is the film height and P is the fluid pressure.

3.1.1.2 Elrod-Adams Cavitation Model

The diverging region of the hydrodynamic lubrication domain creates a low pressure in the fluid which can reach sub-ambient values. The tensile stress placed on the fluid can cause the film to rupture as cavitation. The mass conserving Elrod-Adam algorithm (Elrod & Adam M. L., 1974) is applied in this model, which continues to be applied in numerical models such as Ardah *et al.* (2023), because of its well validated performance and relative simple implementation. A variable is introduced, Φ, which is the relative density:

$$\Phi = \frac{\rho}{\rho_{cav}} \tag{3.2}$$

where ρ is the density of the compressed lubricant and ρ_{cav} in the density of the lubricant at

the cavitation pressure, P_{cav}. A density-pressure relation is defined by:

$$P = P_{cav} + \beta \ln(\Phi) \tag{3.3}$$

where β is the inverse bulk modulus (Pa) of the fluid (i.e. the compressibility). A switch function, g, is used to describe whether the fluid is cavitated at a given location, thereby distinguishing two regions in the domain; the full-film region where there is no cavitation $(g = 1)$, and the cavitation region where the film is a mixture of liquid and gaseous phases $(g = 0)$. The value of g is a function of Φ such that:

$$\begin{aligned} \Phi < 1, \quad g(\Phi) = 0 \\ \Phi \geq 1, \quad g(\Phi) = 1 \end{aligned} \tag{3.4}$$

Incorporating g into equation 3.3 bounds the pressure to a minimum value, P_{cav}, which reflects the observed behaviour in the cavitation region:

$$P = P_{cav} + g\beta \ln(\Phi) \tag{3.5}$$

Given the fluid is highly incompressible (i.e.$\beta >> 0$), from equation 3.5 the value of Φ is very close to one and the logarithm can be approximated as:

$$P = P_{cav} + g\beta(\Phi - 1) \tag{3.6}$$

Incorporating into Equation 3.1 results in a single equation for the hydrodynamic lubrication region:

$$\frac{\partial}{\partial x'}\left(\frac{g\beta h^3}{12\mu}\frac{\partial \Phi}{\partial x}\right) + \frac{\partial}{\partial z'}\left(\frac{g\beta h^3}{12\mu}\frac{\partial \Phi}{\partial z'}\right) = U\frac{\partial \Phi h}{\partial x'} \tag{3.7}$$

3.1.1.3 Film Temperature

The temperature in the film is described by the equation:

$$\frac{\partial}{\partial x'}\left(c_p \rho u T\right) + \frac{\partial}{\partial z'}\left(c_p \rho w T\right) - k\frac{\partial^2 T}{\partial y'^2} = \mu\left(\frac{\partial u}{\partial y'}^2 + \frac{\partial w}{\partial y'}^2\right) \tag{3.8}$$

where T is the film temperature, c_p is the specific heat capacity at constant pressure and k is the thermal conductivity. The velocity field, U, is calculated based on the underlying assumptions used to derive equation 3.1 where components components of velocity are calculated by:

$$\begin{aligned} u &= U\frac{y'}{h} + \frac{1}{2\mu}\frac{\partial P}{\partial x'}\left(y' - h\right)y' \\ w &= \frac{1}{2\mu}\frac{\partial P}{\partial z'}\left(y' - h\right)y' \end{aligned} \tag{3.9}$$

where y' is the position across the thickness of the film. The component of velocity perpendicular to the surfaces, v, is assumed to be negligible given the laminar flow assumption and is excluded from equation 3.8.

3.1.1.4 Film Height

The film height is significant to the solution of Equation 3.1 and is influenced by several factors. The resulting film height profile can be treated as the sum of the factors as shown in Equation 3.10:

$$h = h_e + h_d + h_T \tag{3.10}$$

where h_e is the profile generated by the geometric factors, h_d is the profile formed by the elastic deformation of the surfaces and h_T is the influence of thermal expansion of the bodies. In a journal bearing, the geometric factor affecting the film height is the eccentricity of the shaft which generates a film shape following Equation 3.11:

$$h_e = c(1 - \varepsilon cos(\theta)) \tag{3.11}$$

Where ε is the eccentricity defined as the offset of the shaft centre relative to the clearance, c, and θ is the angular position relative to the location of the minimum film height.

High pressure in the film causes elastic deformation, h_d, of the surfaces which is calculated using the half-space approximation from Hertz (1881):

$$\begin{aligned} h_d(x',z') &= \frac{2\pi}{E'}\int\int \frac{P(x_i,z_k)}{\sqrt{(x'-x_i)^2+(z'-z_k)^2}}dx_i dz_k \\ E' &= \frac{2}{\frac{1-\nu_1^2}{E_1}+\frac{1-\nu_2^2}{E_2}} \end{aligned} \tag{3.12}$$

where E' is the adjusted Young's Modulus and v is the poison's ratio.

An approximation for the thermal expansion, h_T, of the solid bodies is made by taking the average temperature across the surfaces, similar to the approach in Bouyer & Fillon (2004). For a journal bearing case, the expansion is approximated by a change in the radius of the surfaces:

$$h_T = \alpha_1 R_1(\bar{T}_1 - T_{ref}) - \alpha_2 R_2(\bar{T}_2 - T_{ref}) \tag{3.13}$$

where α is the thermal expansion coefficient and $\bar{T}$ is the average surface temperature. The subscripts 1 and 2 denote the adjacent surfaces forming the hydrodynamic lubrication domain.

3.1.1.5 Material Properties

Temperature variation of viscosity is modelled using a power-law model:

$$\mu_T = \mu_0 e^{\gamma_T\left(T-T_{ref}\right)} \tag{3.14}$$

where μ_T is the temperature dependent dynamic viscosity, μ is the dynamic viscosity at temperature T_{ref} and γ_T is the temperature-viscosity coefficient. Pressure also begins to influence the viscosity and generally becomes significant at approximately 0.1GPa. The magnitudes of the pressure in the cases investigated later in this chapter approach the order of 0.01GPa where

the pressure influence is expected as insignificant.

Cavitation of the fluid effects the material properties due to the presence of a gaseous phase in the film. The lubricant rheology is naturally affected by the cavitation in the diverging region where a two-phase flow of liquid and vapour exists. An approximation for each property is found using the results of the Elrod-Adams algorithm as seen in Pierre *et al.* (2004). In this approach, the switch function distinguishing the full film and cavitation regions modifies the fluid properties as shown generally by Equation 3.15 across the field:

$$\phi_{eff} = (1-g)\phi_{eff} + g\phi_l \tag{3.15}$$

where ϕ is a either μ, ρ, k or c_p, ϕ_l is the value for the liquid phase and ϕ_{eff} is the effective value in the cavitation region. A volume averaged method is used to calculate the effective viscosity in the cavitation region using the volume fraction, Φ, from the cavitation model:

$$\mu_{eff} = (1-\Phi)\mu_g + \Phi\mu_l \tag{3.16}$$

where μ_g is the viscosity of the vapor phase and μ_l is calculated from equations 3.14. Similarly the density is calculated by:

$$\rho_{eff} = (1-\Phi)\rho_g + \Phi\rho_l \tag{3.17}$$

where ρ_g and ρ_l are the density of the vapor and liquid phases respectively and ρ_{eff} is the effective density in the cavitation zone. The thermal conductivity is approximated in the same manner:

$$k_{eff} = (1-\Phi)k_g + \Phi k_l \tag{3.18}$$

where k_g and k_l are the thermal conductivity's of the vapor and liquid phases respectively and k_{eff} is the effective thermal conductivity in the cavitation zone. The specific heat capacity in

the cavitation zone is approximated with a mass averaged model:

$$c_{p_{eff}} = \frac{(1-\Phi)\rho_g c_{p_g} + \Phi\rho_l c_{p_l}}{(1-\Phi)\rho_g + \Phi\rho_l} \tag{3.19}$$

where c_{p_g} and c_{p_l} are the specific heat capacity's of the vapor and liquid phases respectively and $c_{p_{eff}}$ is the effective specific heat capacity in the cavitation zone.

3.1.2 Solid Region

Heat generation in the film produces a non-uniform temperature profile in the fluid. Most of the heat is carried out of the region by convection, however conduction with the solid regions is an influential factor to the temperature solution. An energy equation is applied to model the conduction of heat through the solid region and provide an accurate temperature boundary condition for the film region:

$$\nabla \cdot (k\nabla T) = 0 \tag{3.20}$$

Steady-state is applied to an isotropic material with constant thermal conductivity.

3.2 Spatial Domain Discretisation

The numerical methodology described in Section 3.1 is validated on a journal bearing geometry with rotating body (shaft) which is non-conformal with a stationary casing (bush) and flooded with a lubricating oil supplied from an inlet groove at Top-Dead-Center (TDC), creating a hydrodynamically lubricated region (film) between the shaft and bush. The fundamental geometry is presented in Figure 3.2 with the shaft offset from the bush centre generating the converging-diverging wedge geometry inherent to a hydrodynamic lubrication regime. The shaft radius is decreased in Figure 3.2 relative to the bush for visualisation of the film shape

and is not scaled to the true geometry.

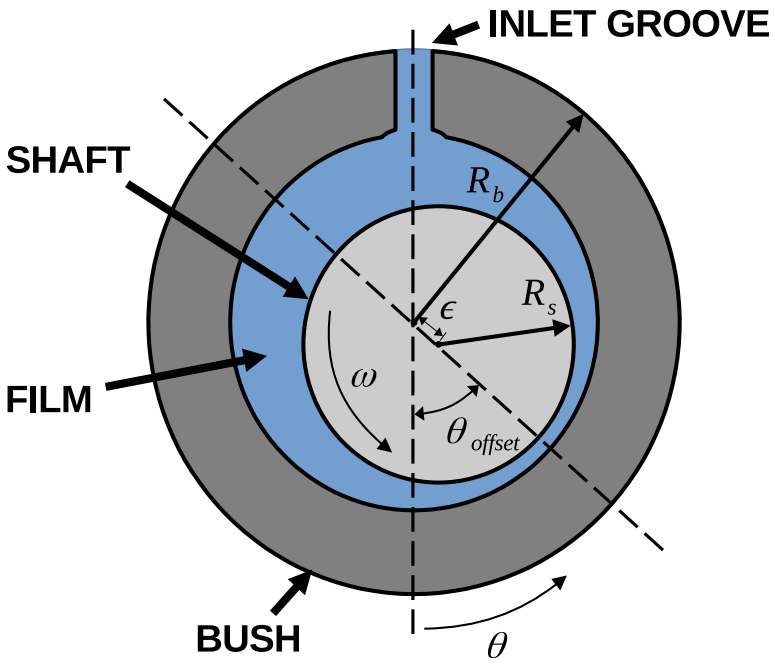

Figure 3.2: Geometry of a Journal Bearing

3.2.1 Film Region

The film region is discretised into two meshes; the pseudo 2D mesh and the 3D mesh which is presented in Figure 3.3. The functionality in OpenFOAM is limited to three-dimensional geometries and generally two-dimensional models are implemented by constructing a thin geometry with a single-cell thickness and applying appropriate boundary conditions. A similar approach is taken here with the pseudo 2D mesh to implement the Reynolds lubrication model which is two-dimensional in nature. The lubrication region is discretised into a thin geometry with a single cell discretisation in the film height direction, as shown in Figure 3.3a. Maintaining a constant thickness across the geometry and applying appropriate boundary conditions to the walls encasing the lubrication region which effectively reduces the numerical model to a two-dimensional form.

The pseudo 2D approach is also beneficial when implementing the energy equation which is three-dimensional, as the overlapping region can be interpolated between each other. Interpolation of the solution between the meshes is applied by mapping the between the closest

cells and faces in each mesh. Therefor, the value is a single cell of the 2D mesh is mapped to multiple cells in the 3D mesh. The distinction between the meshes is highlighted in Figure 3.3 where the 2D film mesh (a), has a single cell across the film height and the 3D film Mesh (b), has multiple cells across the film height. The single cell spanning the height of the 2D mesh creates a pseudo-2D domain given the mesh has a uniform thickness and is used for the solution procedure for pressure in the film. The 3D film mesh is required for the Equation 3.8 to calculate the temperature field. The cross-film conduction is important to the temperature solution and 2D approaches to the temperature field cause the peak temperature to be underestimated due to the inaccurate approximation of the temperature gradient at the film-solid interface. The importance of the temperature profile of the cross film that accounts for the conduction through the solids is noted in Khonsari (1987). The full 3D discretisation of the film domain is applied including discretisation across the film height to resolve the temperature gradients.

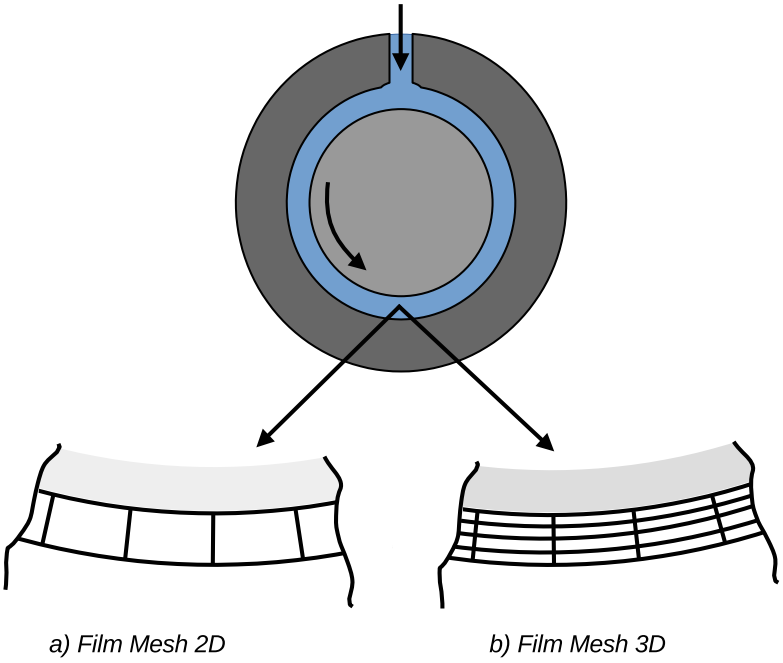

Figure 3.3: Discretisation of the film region

3.2.2 Solid Region

The solid region is discretised into control volumes with the finite-volume method. The interfacing boundary with the film is a key factor when discretising the domain. The solid mesh is

made to be conformal with the film mesh using a structured regular quadrilateral face meshing methodology on the interfacing boundary. An inflation layer is applied from the film-bush interfaces to reduce the cell volumes to a closer order of scale of the film region cells, creating a structured region near the interface. An unstructured mesh is then applied in the broader domain to allow the cells to grow in scale, reducing the total mesh size, and adjusting to the more complex shape around the groove. A schematic of a journal bearing bush is shown in Figure 3.4 identifying the structured and unstructured regions.

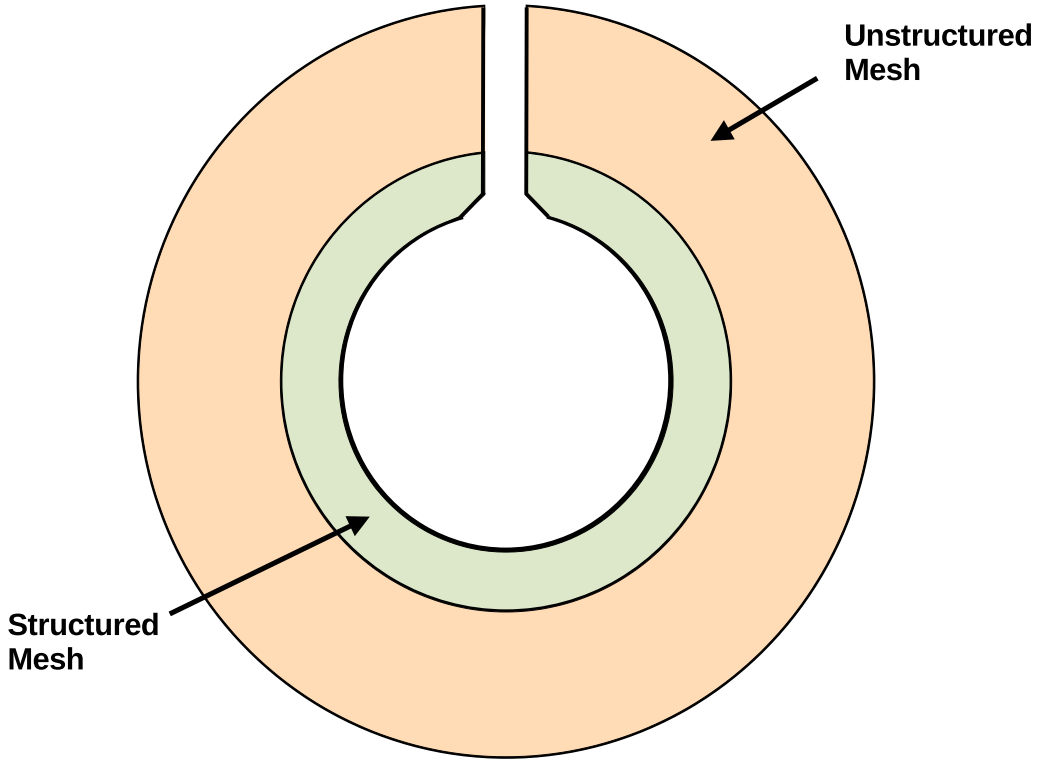

Figure 3.4: Discretisation of the solid region (journal bearing bush)

3.3 Governing Equations Discretisation

In this section the discretisation of the governing equations presented in Section 3.1 is described using the finite volume method. The discretisation schemes applied to each term is detailed and justified.

3.3.1 Pressure

The discretisation of equation 3.7, which describes the pressure in the film including cavitation effects, is described here using the finite volume method. It is useful to present Equation 3.7 generalised in vector form as shown in Equation 3.21.

$$\nabla \cdot \left(\frac{g\beta h^3}{12\mu} \nabla \Phi \right) = \nabla \cdot (\vec{U} \Phi h) \tag{3.21}$$

An element in the film region, C, is shown in Figure 3.5 which spans the height of the film between the two bounding solid surface and with neighbouring cells W and E.

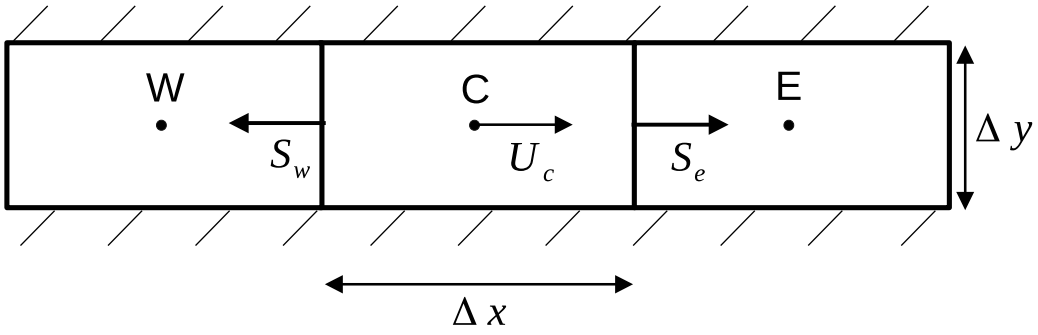

Figure 3.5: Finite volume discretisation of the 2D film region

Integrating equation 3.21 across the volume and applying the divergence theorem gives:

$$\begin{gathered} \oint_{\partial V_c} (\Gamma \nabla \Phi)\, \partial S + \oint_{\partial V_c} \left(\vec{U} h \Phi \right) \partial S = 0 \\ \Gamma = \frac{g\beta h^3}{12\mu} \end{gathered} \tag{3.22}$$

The semi-discretised form is written as:

$$\underbrace{\sum_f (\Gamma \nabla \Phi)_f \cdot S_f}_{diffusive} + \underbrace{\sum_f \left(\vec{U} h \Phi \right)_f \cdot S_f}_{advective} = 0 \tag{3.23}$$

The diffusive term in equation 3.23 is discretised using a second-order central-difference scheme and the advective term is discretised using an upwind scheme. In the cavitation region, the Elrod-Adam switch function algorithm removes the pressure gradients from Equation 3.7, enforcing the assumption of constant pressure in the region, and reduces the equation to a hyperbolic form:

$$\vec{U}\frac{\partial \Phi h}{\partial x} = 0 \tag{3.24}$$

The pure advective nature of the equation in this form requires a first order upwind scheme for numerical stability. Similar to the approach in Vijayaraghavan & Keith (1990) the equation discretisation is varied to allow for a second order solution in the full film region using the switch function, g, to alter the discretisation method in the cavitation region for each cell:

$$\sum_f (\Gamma \nabla \Phi)_f \cdot S_f + \underbrace{g\sum_f \left(\vec{U}h\Phi\right)_f \cdot S_f}_{Second-Order} + \underbrace{(1-g)\sum_f \left(\vec{U}h\Phi\right)_f \cdot S_f}_{First-Order} = 0 \tag{3.25}$$

The velocity vector, $\vec{U}$, is the Couette velocity field calculated from the average velocity of the adjacent surfaces, given the bush is stationary the value of $\vec{U}$ is half the shaft surface velocity. The direction of U is tangential to the solid boundaries in the circumferential direction. Given the gradient with the solid boundaries is 0 following the assumption in equation 3.1, and the 2D film mesh has a uniform thickness as shown in Figure 3.3, therefore the face areas S_w and S_e are equal, the discretised form of the equation is:

$$\begin{aligned} &\Gamma_e \frac{\Phi_e - \Phi_C}{\Delta x} + \Gamma_w \frac{\Phi_C - \Phi_w}{\Delta x} \\ &+ g\left[\{(\vec{U}h\}_e \frac{\Phi_E + \Phi_C}{2} + \{\vec{U}h\}_w \frac{\Phi_c + \Phi_W}{2}\right] \\ &+ (1-g)\left[\{\vec{U}h\}_e \Phi_E + \{\vec{U}h\}_w \Phi_C\right] = 0 \end{aligned} \tag{3.26}$$

3.3.2 Film Height

The height, h, in the film region is treated as a scalar value for each element, as opposed to being part of the geometry of the mesh. The solution of the film height is therefore independent of the mesh as presented in 3.6. This setup allows the value of h to vary in the solution without requiring a mesh to be regenerated, which would increase the computational time and complexity of the overall methodology. This difference must be incorporated in the calculation of fluxes on the cell faces which is noted in the discretisation of the temperature equation in Section 3.3.3.

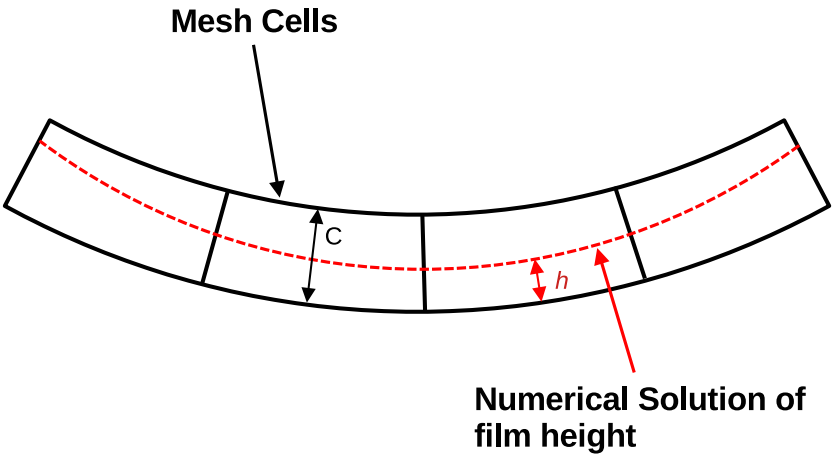

Figure 3.6: Difference in height between the mesh and the numerical solution

The film height is calculated explicitly from the latest solution of the the other fields in the domain where the calculation of h_e and h_T is straightforward. h_e is calculated for each cell given the element's coordinates in the spacial domain and values for eccentricity, shaft offset and shaft radius. The value of h_T is applied uniformly to all elements in the film domain from the solution of 3.13.

The discretised form of equation 3.12 is written as

$$h_d(x,z) = \frac{2\pi}{E'} \sum_{i=0}^{n-1} \sum_{k=0}^{n-1} \frac{P(x_i,z_k)}{\sqrt{(x-x_i)^2+(z-z_k)^2}} \Delta x_i \Delta z_k \tag{3.27}$$

The computational cost of equation 3.27 is of the order $O(n^2)$ due to the embedded summation, therefore exponentially increasing with the refinement of the mesh. The denominator in equation 3.27 is 0 at the point where $x = x_i$ and $z = z_k$, therefore in the numerical implementation this point is ignored to prevent a division by 0 error.

3.3.3 Temperature

Figure 3.7 shows an element in the height discretised film region.

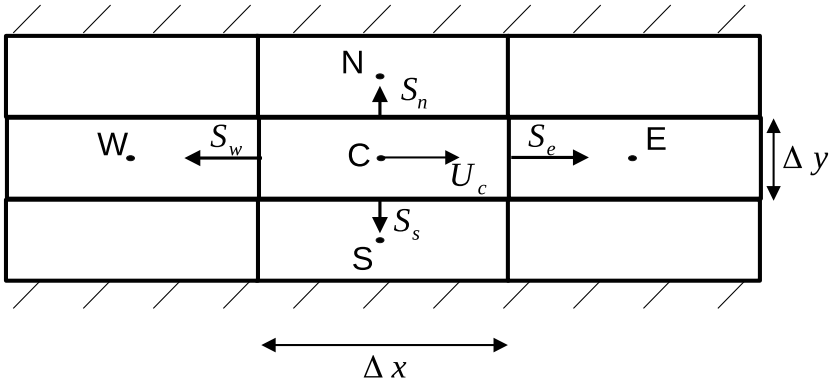

Figure 3.7: Finite volume discretisation of the 3D film region

Conservation of energy is applied to the cell to derive Equation 3.28:

$$\begin{aligned} &\nabla \cdot (c_p \rho U T) - k\nabla^2 T = \tau \cdot \nabla U \\ &\tau = \nu \left(\nabla U + \nabla U^T \right) \end{aligned} \tag{3.28}$$

Integrating equation 3.28 across the cell volume and applying the divergence theorem gives:

$$\oint_{\partial V_C} \left(c_p \rho \vec{U} T \right) \partial S - \oint_{\partial V_C} (k \nabla T) \, \partial S = \oint_{\partial V_C} \phi \, \partial V \tag{3.29}$$

where ϕ is the heat source term. The semi-discretised form of 3.28 is written as:

$$\sum_f \left(c_p \rho \vec{U} T\right)_f \cdot S_f \sum_f (k \nabla T)_f \cdot S_f = \phi \Delta V_C$$
$$\phi = \tau \cdot \nabla U \tag{3.30}$$

The flow of fluid is highly convective in the lubrication region and for stability an upwind discretisation procedure is required for the convective term in Equation 3.30. Conduction is dominant in the film height direction due the dominant convective terms parallel to the surfaces. Shearing of the fluid is also dominated by the velocity gradients perpendicular to the surfaces. Given the laminar assumption in equation 3.1, there is no flow perpendicular to the solid surfaces. The film height profile is not reflected in the mesh which has a uniform thickness, therefore affecting both the fluxes parallel to the flow, S_e and S_w, and the gradients adjacent to the solid regions, S_n and S_s. To accurately model the convective terms the relative film height value, H, is included as a variable to account for the non physical surface fluxes, S_f, in the direction of flow (i.e. S_e and S_w in Figure 3.7):

$$H = \frac{h}{C} \tag{3.31}$$

where h is the film height and C is the bearing clearance in the mesh. The discretised form of equation 3.28 with the outlined assumptions for the cell in Figure 3.7 is written as:

$$\begin{aligned} &\left[(c_p \rho \tilde{H} u)_w T_C \Delta S_w - (c_p \rho \tilde{H} u)_e T_E \Delta S_e\right] \\ &- \frac{k}{\tilde{H}^2}\left[\frac{T_N - T_C}{\Delta y}\Delta S_n + \frac{T_C - T_S}{\Delta y}\Delta S_s\right] \\ &= \left[\frac{\mu}{\tilde{H}^2}\left(\frac{\Delta u}{\Delta y}^2\right)\right]\tilde{H}\Delta V \end{aligned} \tag{3.32}$$

3.4 Boundary Conditions

In this section the boundary conditions applied in the film and solid regions are described and justified. This includes the coupling between the solutions of the lubrication and solid models.

3.4.1 Film Region

3.4.1.1 Inlet

The TEHL methodology does not directly model the conditions within the groove as the thin film assumptions are not applicable in this region. Boundaries to the film region are defined at the interface with the groove and explicitly calculated from the solution of previous iteration. Figure 3.8 shows the film region near the supply groove where the film inlet and film outlet boundaries are located.

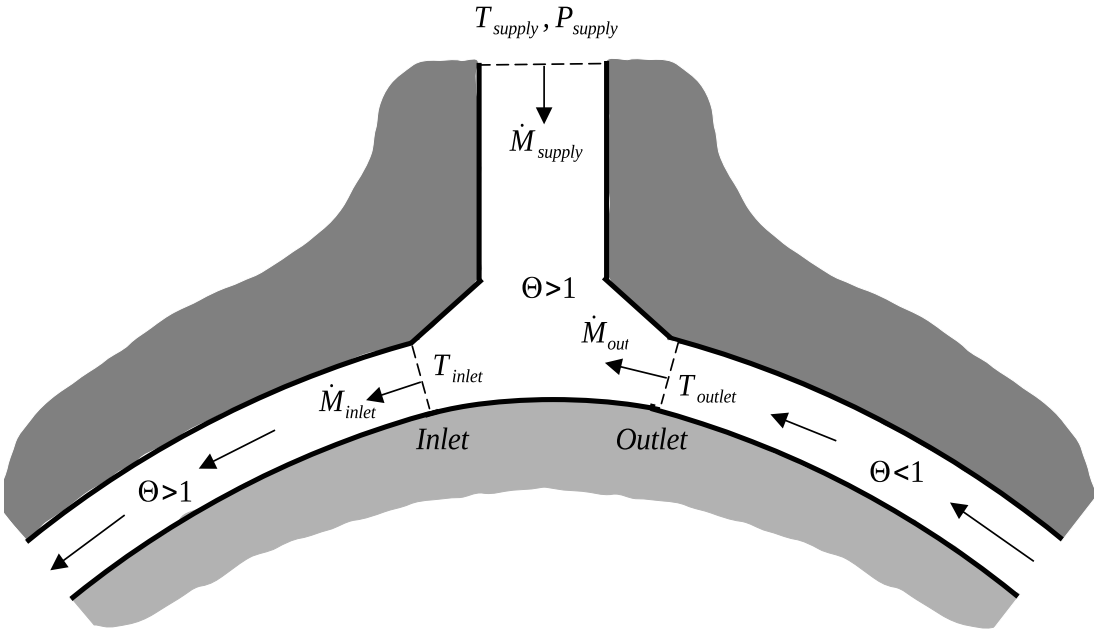

Figure 3.8: Diagram of the inlet and outlet boundary conditions for the film region

The pressure is assumed to be constant and uniform at the inlet to the film domain. For a journal bearing this value is assumed to be equal to the oil supply pressure, P_{supply}. Translating to the relative density field, it is assumed that a full supply of fluid is available, therefore g equal to one across this boundary and Φ is calculated from the pressure using equation 3.5.

For a journal bearing, the temperature at the inlet to the film is uncertain because of the re-circulating hot oil from the film outlet shown in Figure 3.8. To approximate the temperature at the film inlet, mass flow continuity is applied between the film inlet, $\dot{M}_{inlet}$, and film outlet,

$\dot{M}_{outlet}$, to estimate the lubricant supply, $\dot{M}_{supply}$:

$$\dot{M}_{supply} = \dot{M}_{inlet} - \dot{M}_{outlet} \tag{3.33}$$

The temperature at the inlet is then estimated assuming the fluid from the supply is constant temperature and completely mixes with the flow from the film outlet:

$$T_{inlet} = \frac{\left(\dot{M}_{outlet} T_{outlet} + \dot{M}_{supply} T_{supply}\right)}{\dot{M}_{inlet}} \tag{3.34}$$

This assumption of perfect mixing in the groove could be idealistic to apply in all operating conditions and also neglects heat transfer in the groove with the bush. These effects would be considered by using a CFD model in the groove region to consider more fluid behaviour in the solution.

3.4.1.2 Outlet

The boundary to the groove of a journal bearing is described as the film outlet, where recirculating oil meets with the fresh supply oil. The positive static pressure from the oil supply generates a pressure gradient between the groove and the diverging region where cavitation of the film occurs and sub-ambient pressures can occur. Reverse flow of the oil, where fluid flows from the groove to the diverging region, could therefore be assumed at low rotational speeds. Assuming this condition, the same setup as at the film inlet would be applied for pressure whereby g is 1 across this boundary and Φ is calculated from the supply pressure using equation 3.5. The temperature boundary condition would be dependent of the direction of flow and the element face. For flow out of the film domain, a temperature gradient of 0 would be applied and for reverse flow into the film domain a temperature of $40°C$ would be applied.

This setup can lead to numerical instability in the energy equation due to the velocity profile near the film outlet where the direction of flow varies across the film height. The fluid at the outlet is therefore assumed to flow out of the film region into the groove, neglecting reverse flow from the groove to the film at the outlet boundary. The boundary condition for Φ is a fixed

gradient of 0 to reflect the direction of the flow out of the domain. This causes reformation of the film after the outlet boundary.

3.4.1.3 Sides

The side boundaries of the film are presented in Figure 3.9. As seen in Alakhramsing *et al.* (2015), the appropriate setup for Φ at this boundary is dependent on the flow direction which theoretically varies along the circumference. In the converging region, a positive pressure field relative to atmospheric will force fluid out of the film. Therefore, a fixed value of Φ which relates to atmospheric pressure from Equation 3.3 is appropriate to reflect the atmospheric pressure condition at this boundary. In the diverging region, the pressure reduces to the cavitation pressure which may be ambient or sub-ambient pressure, therefore, the flow direction will be into the film region. A fixed gradient for Φ of 0 is appropriate to reflect the inflow assumption. The variable, g, is used to differentiate the full-film and cavitation regions, is used to inform the boundary condition to switch between each case.

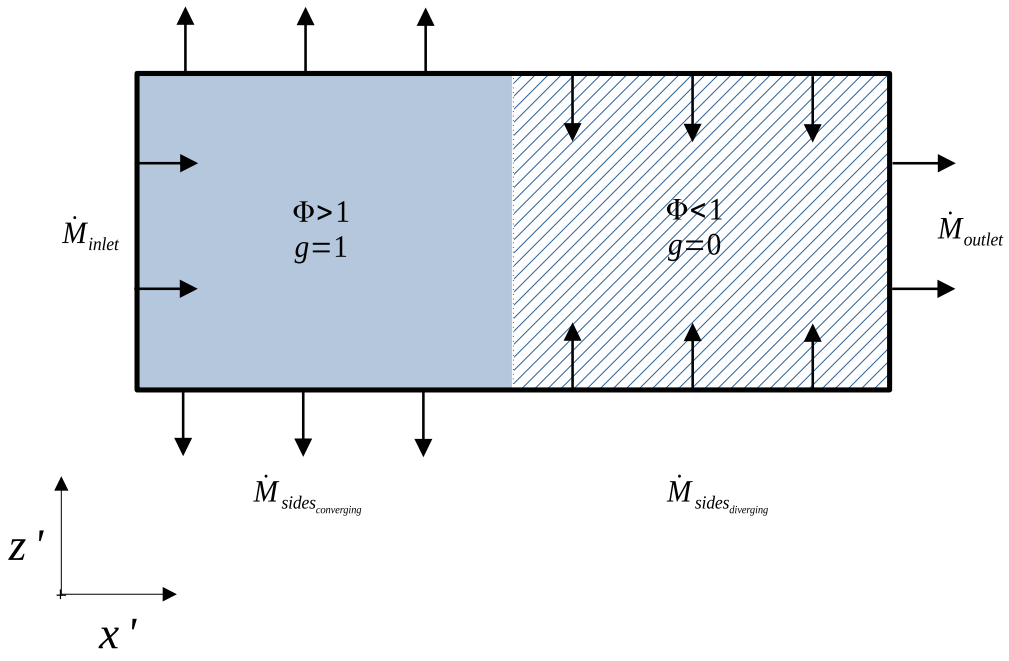

Figure 3.9: Diagram of the film-sides boundary condition setup for a journal bearing case

3.4.1.4 Bush Interface

Temperature is coupled between the film region and the solid regions based on conduction between the materials and enforcing heat flux continuity between the domains. Figure 3.10 shows a diagram of an element in the film region adjacent to the solid region.

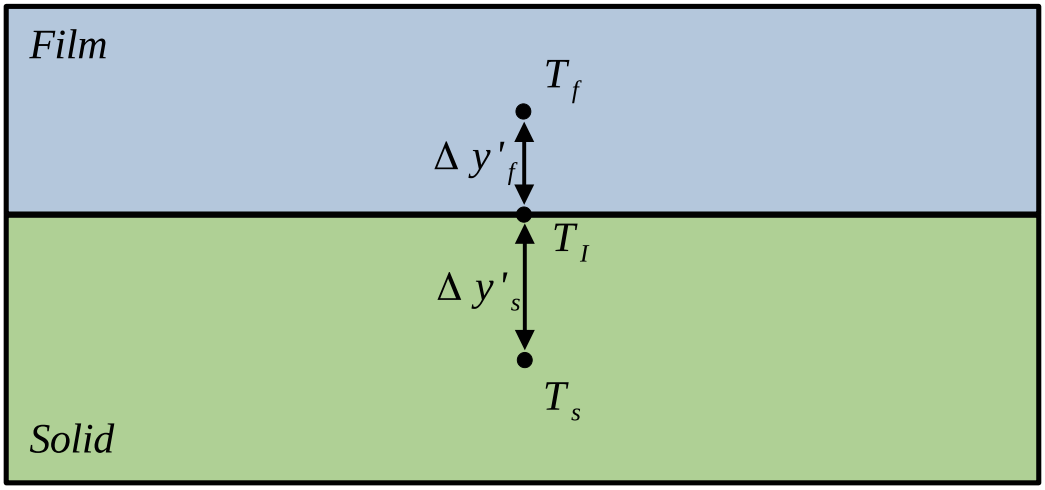

Figure 3.10: Diagram of the film-solid temperature coupling boundary condition

Applying heat continuity:

$$k_f \left.\frac{\partial T}{\partial x}\right|_f = -k_s \left.\frac{\partial T}{\partial x}\right|_s \tag{3.35}$$

in discrete form, equation 3.35 becomes:

$$\frac{k_f}{\Delta_f}(T_I - T_f) = -\frac{k_s}{\Delta_s}(T_I - T_s) \tag{3.36}$$

where T_I is the temperature at the interface. The relative film height, H is also incorporated as described in section 3.3.3:

$$\frac{k_f}{H\Delta_f}(T_I - T_f) = -\frac{k_s}{\Delta_s}(T_I - T_s) \tag{3.37}$$

3.4.1.5 Shaft

The high rotational velocity of the shaft should be considered in the thermal boundary condition and generally is treated as an isothermal body. The temperature of the shaft is approximated based on the assumption of net zero heat flux to the shaft, as applied in Ferron *et al.* (1983) and Pierre *et al.* (2004):

$$\dot{Q} = \int \frac{k_f}{H} \frac{\partial T}{\partial y}|_s dA = 0 \tag{3.38}$$

The boundary for the film-shaft interface is therefore a Dirichlet condition where the shaft temperature, T_s, is calculated from the solution temperature of the previous iteration:

$$T_s = \frac{\sum \frac{k_i T_i}{\Delta y_i}}{\sum \frac{k_i}{\Delta y_i}} \tag{3.39}$$

3.4.2 Solid Region

Three boundaries are defined in the bush (Solid region) of the journal bearing case as shown in Figure 3.11.

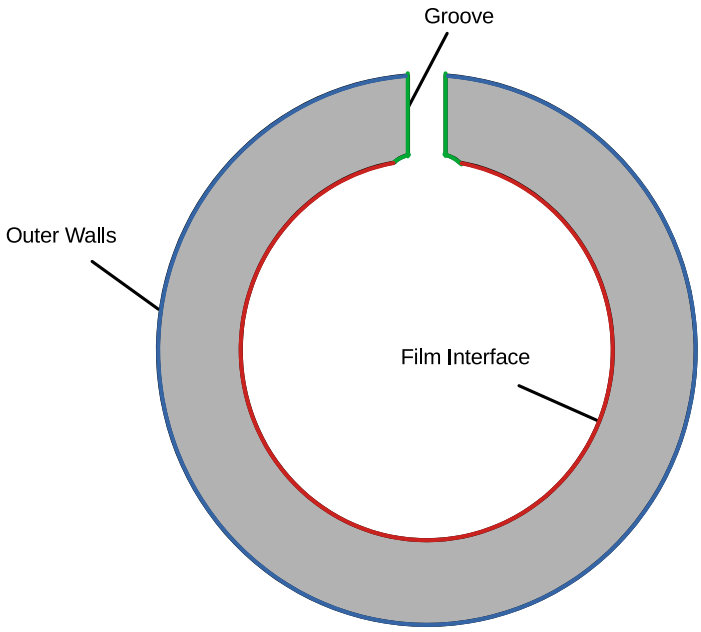

Figure 3.11: Diagram showing the boundaries of the bush region

The Outer Walls are the boundaries which are open to surrounding air, the Film Interfaces which couples with the film region and the Groove where fresh oil is supplied.

3.4.2.1 Film Interface

The boundary condition with the film region is applied in the same format as described in section 3.4.1.4.

3.4.2.2 Outer Walls

The free convection hypothesis is applied at the outer walls of the solid region:

$$k_s \left.\frac{\partial T}{\partial x}\right|_s = -h_c(T - T_{amb}) \tag{3.40}$$

where h_c is the convection coefficient and is dependent on the assumptions of the flow conditions against the wall. Typically as value of $50 - 100 \frac{W}{m^2 K}$ is used for the convection coefficient,

for example $75\frac{W}{m^2K}$ is used in Pierre *et al.* (2004). Heat in the film is predominantly carried out of the region by convection and is insensitive to the convection coefficient at the outer walls of the bush.

3.4.2.3 Groove

The free convection condition, equation 3.40, is applied at the bush interface with the groove. A higher value of the convection coefficient is used to reflect the higher thermal conductivity of the lubricating oil compared with air. Furthermore, the reference temperature is assumed to be the temperature of the supply oil.

3.5 Numerical Solution Procedure

In this section the numerical process is described which details the procedure taken to converge towards a numerical solution. The iterative process is presented both globally between the lubrication and solid regions, and within each region.

3.5.1 Multi-Region Process

A multi-region setup is used in the numerical model where individual regions are defined with separate governing equations. A sequential procedure is followed where a solution is found for each region iteratively using the latest solution from other regions. The process continues while monitoring the convergence of the maximum temperature in each region to signify convergence of the global solution. The maximum temperature is selected as the parameter of interest given this value is coupled between the TEHL and Solid methodologies. The absolute relative change in maximum temperature is applied as the convergence criteria following Equation 3.41.

$$e_i + 1 = \frac{|T_{i+1} - T_i|}{T_{i+1}} \tag{3.41}$$

A tolerance of $1e^{-4}$ is used to signify convergence of the multi-region solution and terminates the process when reached.

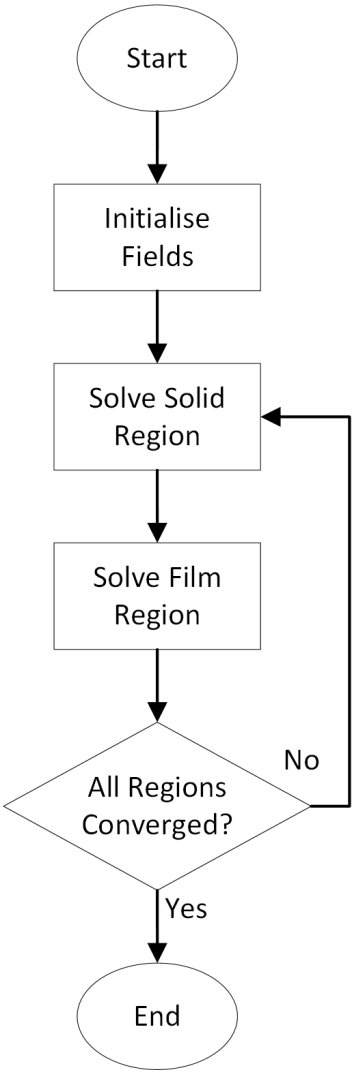

Figure 3.12: Flowchart of the Multi-region numerical procedure (see Figure 3.13 for an expansion of the Film Region numerical procedure)

3.5.2 TEHL Model

To find the solution within the TEHL region, the equations described in section 3.3 are solved iteratively until the initial residual for pressure and temperature is below a tolerance of $1e^{-4}$, or their relative change in successive iterations is below a given value. All other variables are calculated explicitly from the temperature and pressure solution, which is the justification for only monitoring the convergence of these two fields.

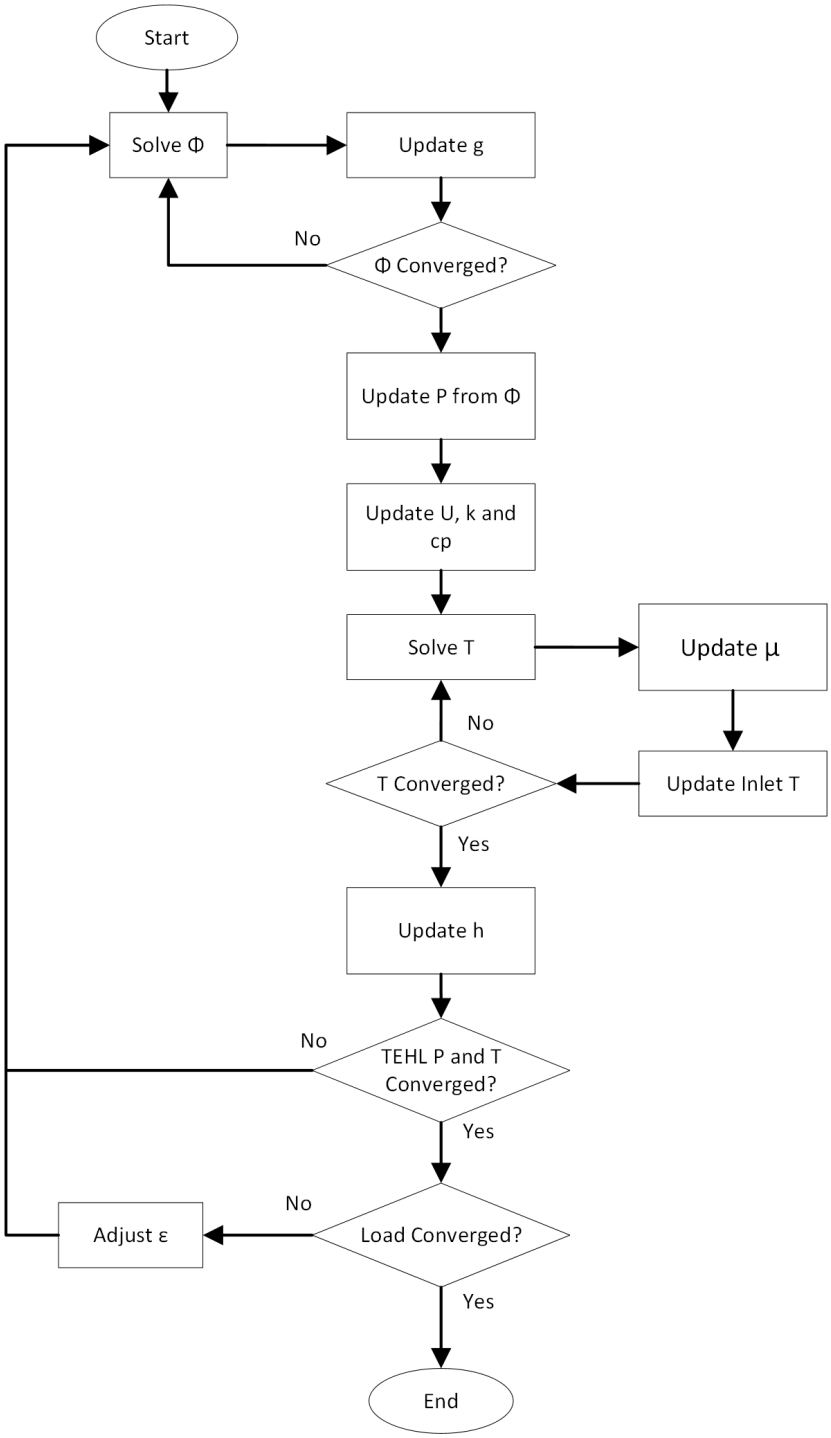

Figure 3.13: Flowchart of the TEHL solution procedure (”Solve Film Region” in Figure 3.12)

The switch function in the cavitation model is applied iteratively in a sub-loop within the TEHL solution procedure. The modification made by Fesanghary & Khonsari (2011), which is presented in algorithm 1, is effective at stabilising the convergence of the cavitation algorithm and locating the boundary of the cavitation region. However, this approach was found to

create a disconnected pressure solution and an adjustment is proposed later in the section to improve the numerical convergence procedure. During the cavitation algorithm incorporating the stabilisation Algorithm 1, the value of g is set to 0 when the value falls below 10^{-6}. Due to the function setup, an element with a value for g of 0 cannot be altered when the corresponding value of Φ is greater than 1. This is found to limit the location of the cavitation region boundary creating a disconnected pressure profile. The disconnected profile behaviour is shown in Figure 3.14 at different iterations of a solution pressure of pressure at eccentricity 0.5 and rotational speed 500rpm.

Algorithm 1 Switch function stabilisation algorithm from Fesanghary & Khonsari (2011)

if $\Phi_i >= 1$ **then**
    if $gFactor > 0$ **then**
        $g_i = g_i / gFactor$
    else
        $g_i = 1$
    end if
else
    $g_i = g_i \cdot gFactor$
end if
if $g_i > 1$ **then**
    $g_i = 1$
end if
if $g_i < 10^{-6}$ **then**
    $g_i = 0$
end if

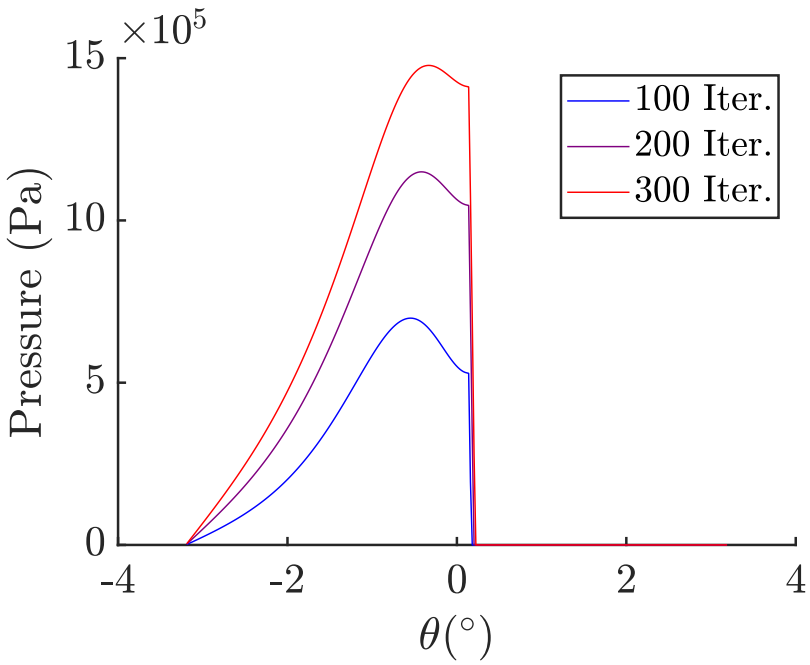

Figure 3.14: Centerline pressure profile in a journal bearing across multiple iterations of the cavitation algorithm using the modification from Fesanghary & Khonsari (2011) at eccentricity 0.5 and 500rpm

The setup is altered in Algorithm 2 whereby a minimum value for g, *gLimit*, which is close to 0 is applied to maintain the possibility for the cell values to change throughout the solution procedure. The calculation of g on line 3 is also accelerated using Φ_i, whereby if g is less than 0, the value will increase towards 1 at a greater rate proportional to the difference of Φ from one. Figure 3.15 shows the affect of the adjusted stabilisation function on the centreline pressure profiles. The value of *gLimit* used in this case is 10^{-4}. In comparison to Figure 3.14, there is a continuous profile between the high and low pressure regions at 300 iterations.

Algorithm 2 Adjusted switch function stabilisation algorithm

```
if Φ_i >= 1 then
    if gFactor > 0 then
        g_i = g_i / (gFactor · Φ_i)
    else
        g_i = 1
    end if
else
    g_i = g_i · gFactor
end if
if g_i > 1 then
    g_i = 1
end if
if g_i < gLim then
    g_i = gLim
end if
```

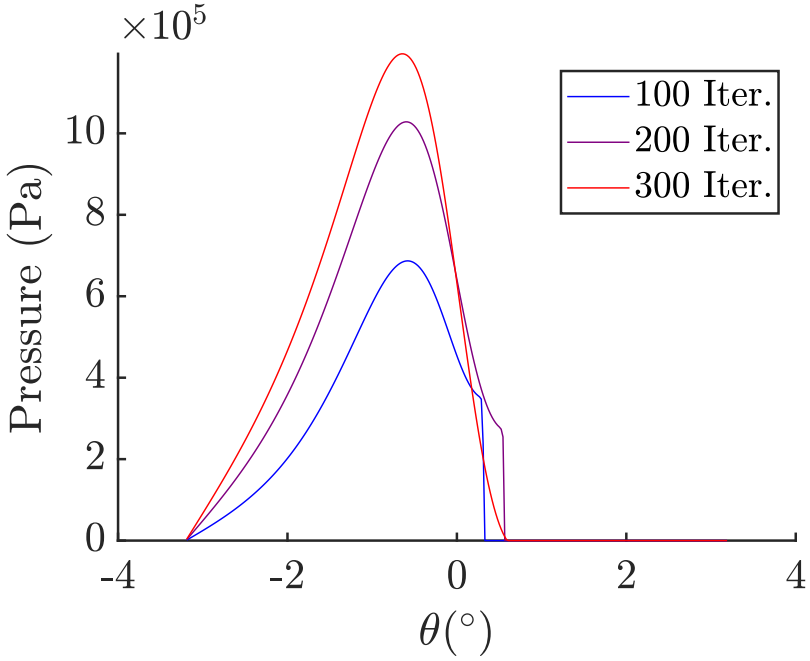

Figure 3.15: Centerline pressure profile in a journal bearing across multiple iterations of the cavitation algorithm using the adjusted stabilisation function 2 at 0.5 eccentricity and 500rpm

3.6 Mesh Sensitivity Study

A mesh independence study is performed to test the affect from various meshing parameters on the solution. A simplified two-dimensional case setup is devised as shown in Figure 3.16 of an unwrapped journal bearing where the horizontal and vertical direction relate to the cir-

cumferential and radial directions respectively. The highly structured and regular mesh is fast to produce and allows the parameters to be tested independently.

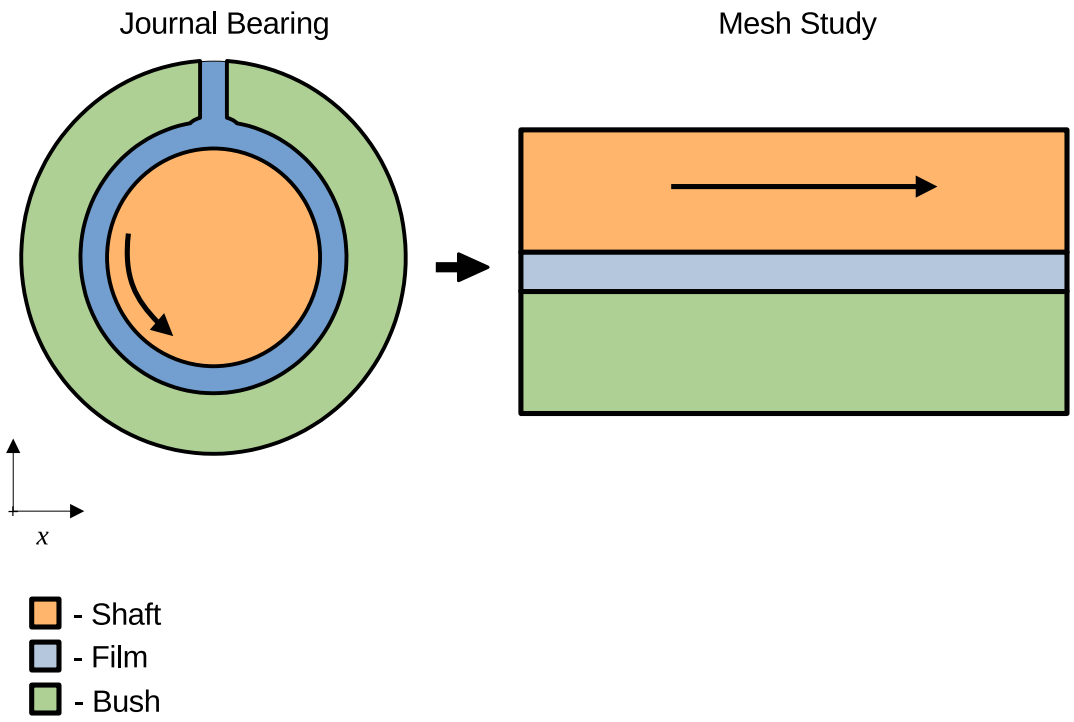

Figure 3.16: Setup of the mesh sensitivity studies geometry compared with the journal bearing geometry

The mesh parameters which are tested are shown in Figure 3.17 which are the number of cells in the vertical direction in the film region (Case A), the element size ratio across the film-solid interface (Case B) and the number of cells in the horizontal x-direction (Case C).

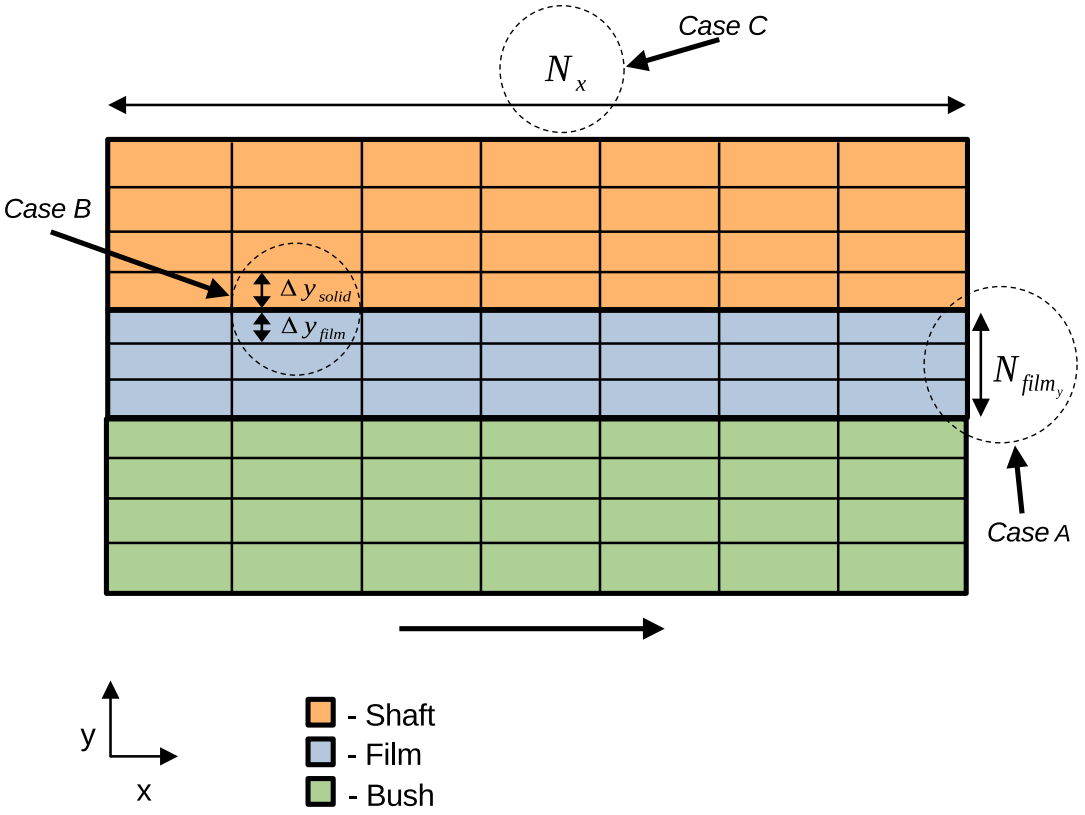

Figure 3.17: Parameters varied in the mesh sensitivity study

The maximum field values for the bush temperature, film temperature and film pressure are monitored to show mesh sensitivity of the solution. The values are presented relative to the value at the highest refinement:

$$\bar{\phi} = \frac{\phi^n}{\phi^N} \tag{3.42}$$

where ϕ is the field variable, n is the index related to the mesh refinement and N is the index of the maximum refinement. The temperature values are taken in $^{\circ}C$ when generating the relative values. The mesh sensitivity case is performed with eccentricity values of 0.2 and 0.8, and at rotational speeds 500rpm and 5000rpm, to test cases at low and high eccentricity and speed, based on operating conditions from Ferron *et al.* (1983). The dimensions of the bearing from Ferron *et al.* (1983) are shown in Figure 3.1, which are used to calculate the dimensions of the mesh sensitivity study mesh.

Property	Symbol	Value
Shaft Radius (mm)	R_s	50
Bush Radius (mm)	R_b	100
Bush Length (mm)	L	80
Clearance (μm)	C	145
Groove Angle (°)	θ_g	18
Groove Length (mm)	L_g	70
Feed Hole Diameter (mm)	D_g	14
No. Feed Holes		3

Table 3.1: Bearing Properties from Ferron *et al.* (1983)

Case a:

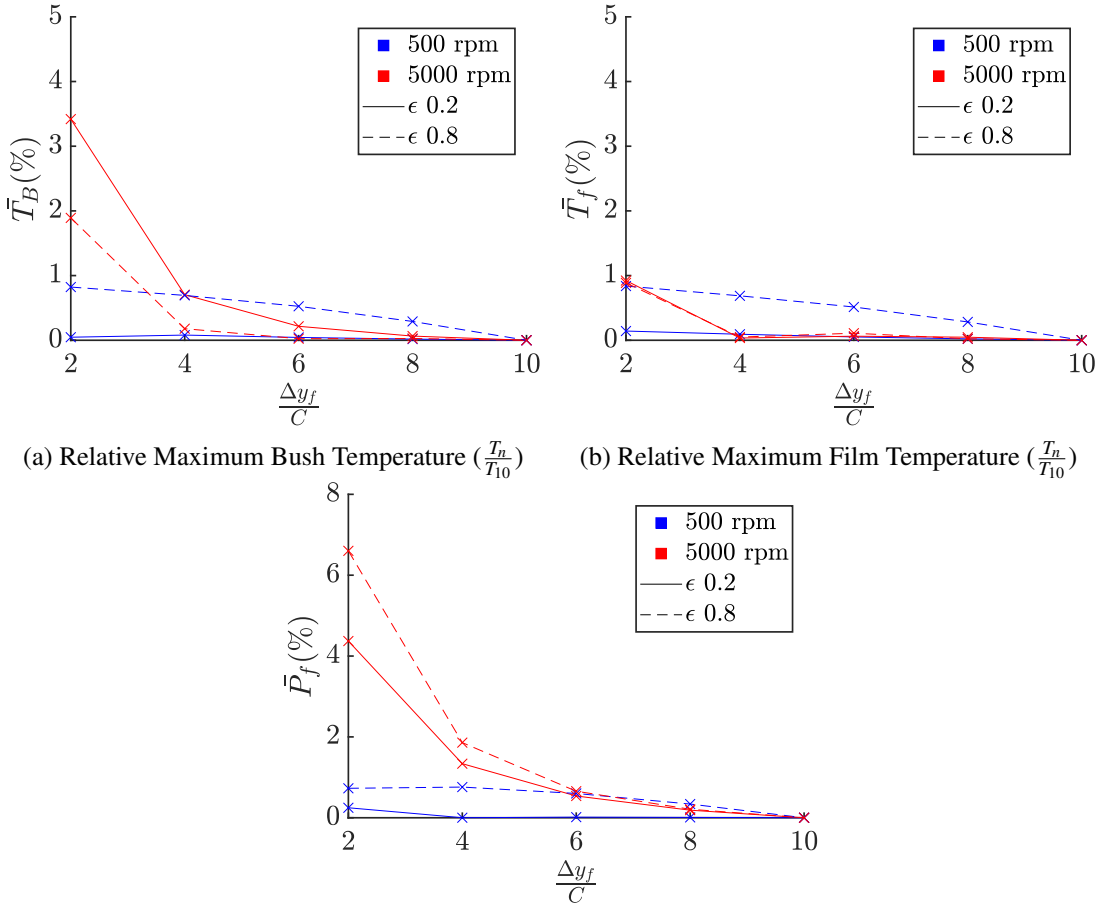

(a) Relative Maximum Bush Temperature ($\frac{T_n}{T_{10}}$)

(b) Relative Maximum Film Temperature ($\frac{T_n}{T_{10}}$)

(c) Relative Maximum Film Pressure ($\frac{P_n}{P_{10}}$)

Figure 3.18: Variation of the solution against the number of cells across the film thickness

The number of elements across the film height is varied between 2 and 10 cells. The cell size ratio across the film-solid interface is 1 and the number of cells parallel to the flow is 800. The results are presented in Figure 3.18 which show the variation of maximum temperature in the

bush, Figure 3.18a, maximum temperature in the film, Figure 3.18b, and maximum pressure in the film, Figure 3.18c, all compared to the discretisation, with the relative values calculated using Equation 3.42.

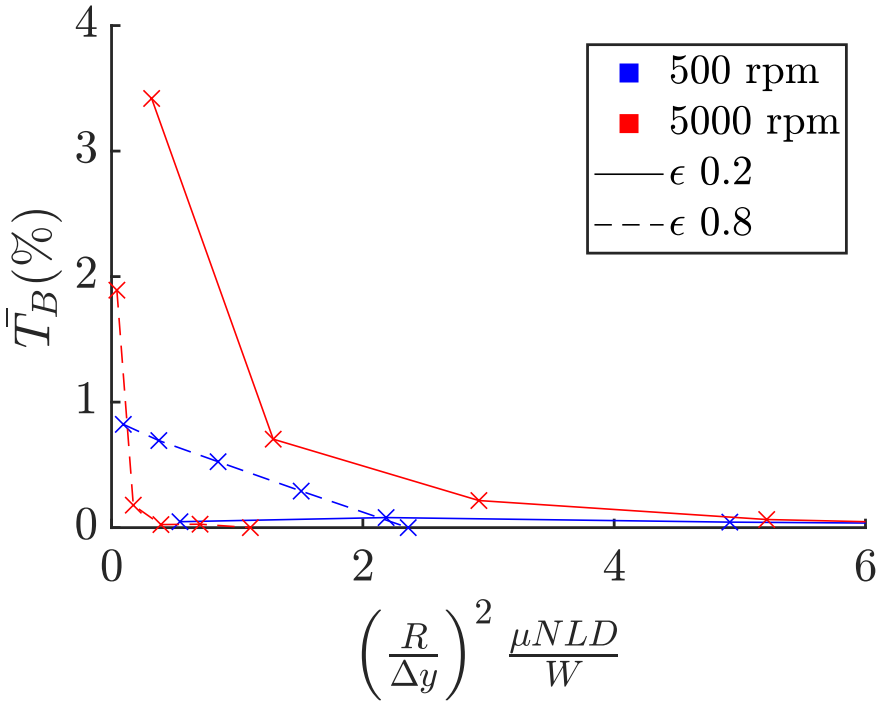

Figure 3.19: Variation of maximum bush temperature against the non-dimensionalised bearing mesh parameter

Comparing the results of each field, the maximum bush temperature is highly affected by the discretisation across the film height. Variation of the bush temperature is $< 1\%$ at a 4 cell refinement for the high rotational speed cases as seen in Figure 3.18a. Mesh sensitivity in the solution is shown to be affected by the rotational speed for the temperature results, where the higher rotational speed case has a greater error at lower refinement. This is understandable considering the rotational speed effects the heat generated from shearing of the fluid, therefore higher rotational speed cases generally increase the heat dissipation in the case. Temperature in the film is relatively unaffected by the y-cell discretisation, showing a difference of $< 1\%$ between the minimum and maximum cell discretisation levels. The film pressure is significantly affected by this discretisation as shown in Figure 3.18c, requiring a 6 cell discretisation to reduce the pressure to $< 1\%$ of the maximum discretisation level. The pressure solution is most likely affected by the viscosity field resulting from the temperature solution, given this is the most prominent value coupling the temperature and pressure solutions. The greater dis-

cretisation across the film height improves the capture of the temperature profile and affects the resulting averaged viscosity across the film height, which explains why the pressure varies significantly while the maximum film temperature is relatively consistent. Figure 3.19 shows the relative maximum bush temperature against a non-dimensional value relating the operating parameters, geometry and mesh discretisation across the film height.

Case b:

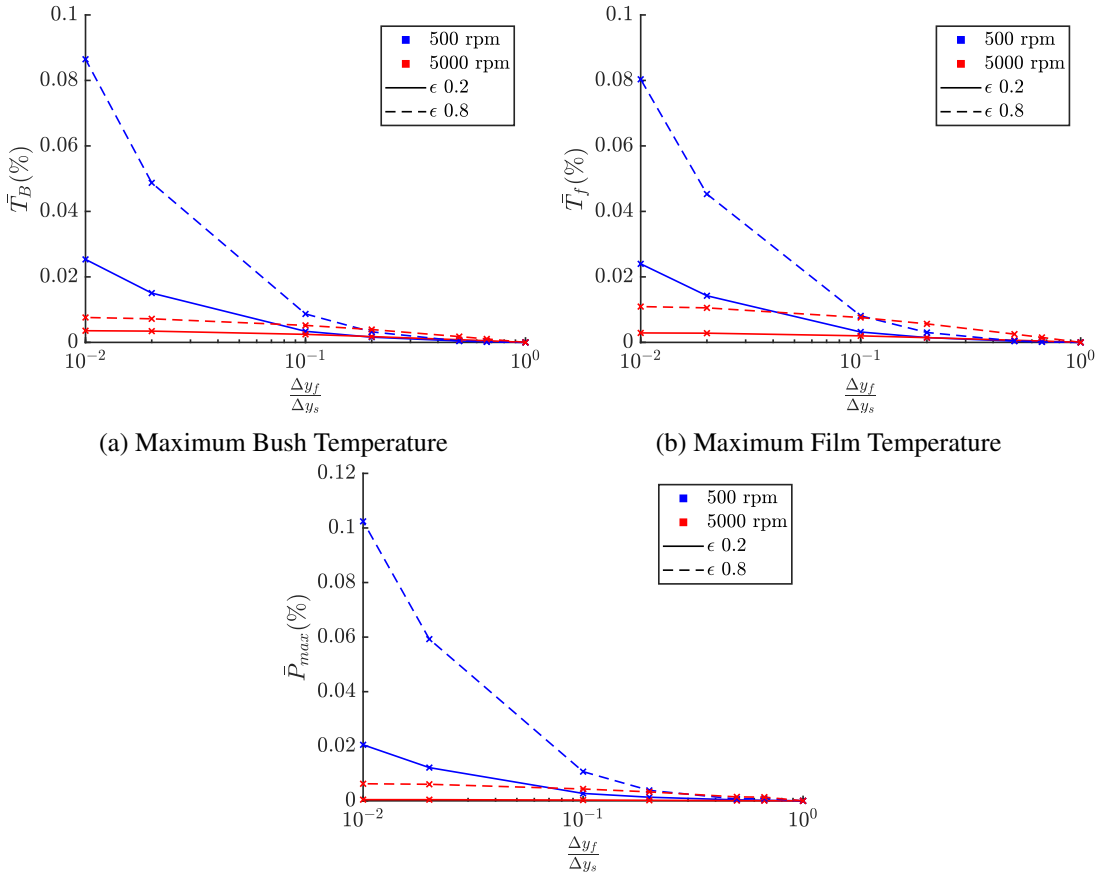

(a) Maximum Bush Temperature

(b) Maximum Film Temperature

(c) Maximum Film Pressure

Figure 3.20: Variation of the solution against the ratio of cell size at the film-solid interface

The influence of the cell height ratio at the film-solid interface is shown in Figure 3.20. Across the film height 8 cells are used and 400 cells are used in the direction parallel to the flow. The results show less sensitivity in comparison to Case a where all test cases show $< 1\%$ variation in the solution. The greatest variation is seen in the low rotational speed and high eccentricity cases, approximately 0.1% in each field. The low sensitivity of the solution shown in the results suggests this mesh parameter is insignificant. A high cell size ratio between the film and solid region could therefore be applied which would be beneficial towards reducing the

mesh size in the solid region.

Case c:

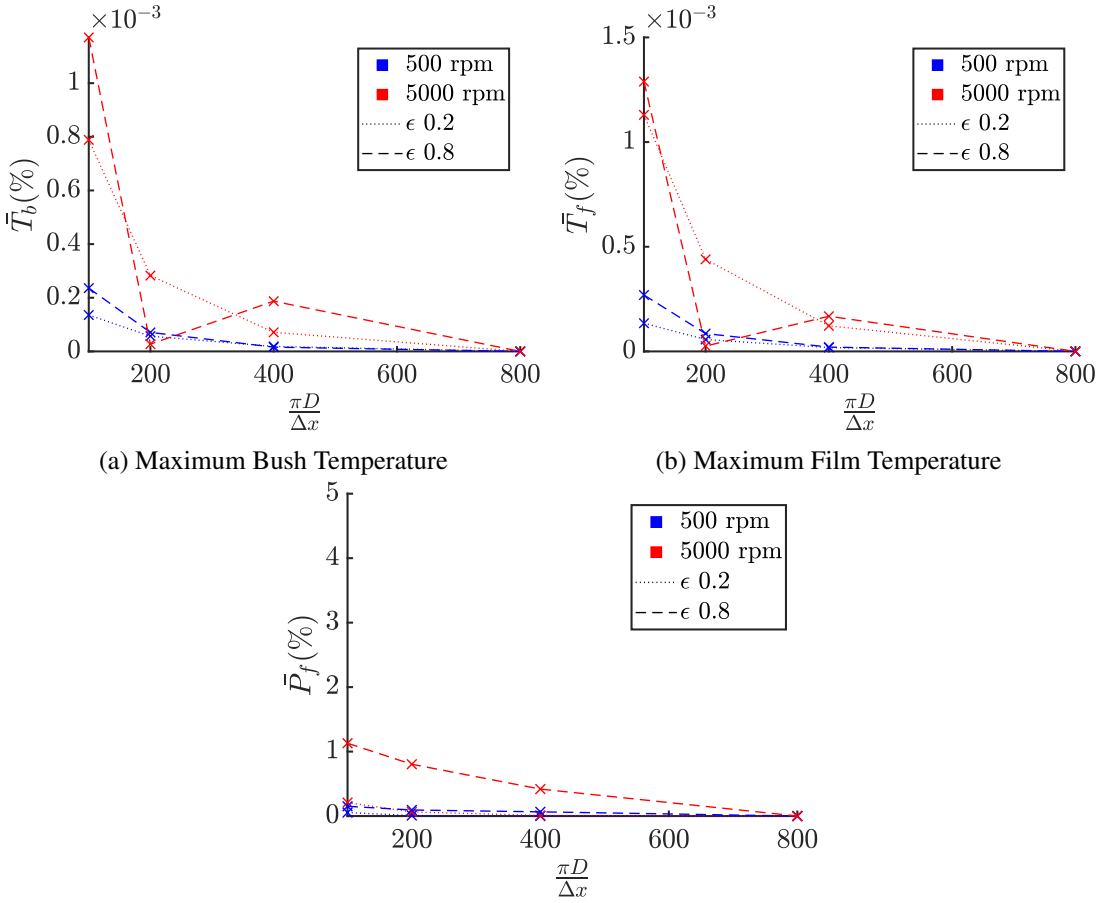

(a) Maximum Bush Temperature

(b) Maximum Film Temperature

(c) Maximum Film Pressure

Figure 3.21: Variation of the solution against the number of elements in the direction of flow

The affect on the solution from the discretisation of the case in the direction of the flow is shown in Figure 3.21. Solutions of the temperature are generally unaffected by this aspect of the mesh where variation of maximum temperature in the bush and film regions is less than approximately 0.001%. Film pressure shown in Figure 3.21c is more sensitive to the discretisation in the flow direction, requiring a 200 cell discretisation to reduce variation to $< 1\%$. The highest eccentricity and rotational speed case is most sensitive to the discretisation in the flow direction, which is consistent with increasing pressure in the film.

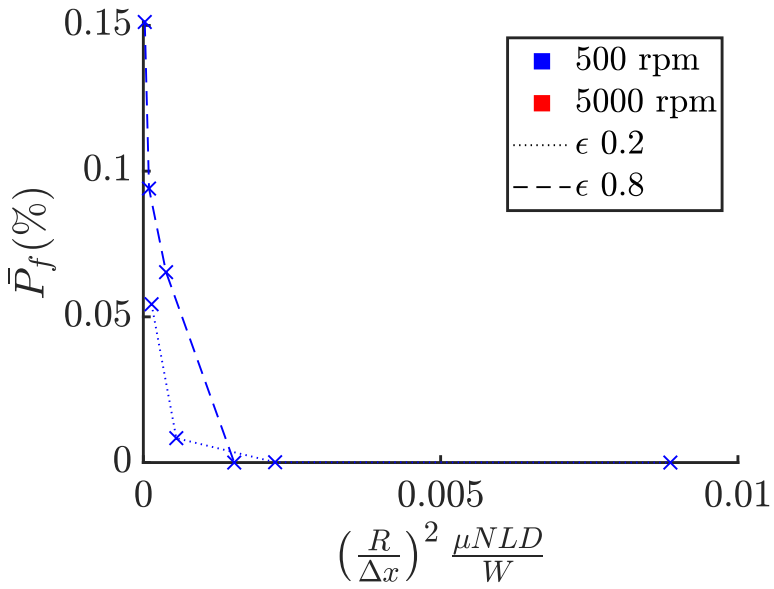

Figure 3.22: Variation of maximum film pressure against the non-dimensionalised bearing mesh parameter

The study of mesh sensitivity has shown that the a prominent parameter to consider is the discretisation across the film height which impacts both the maximum temperature in the bush and maximum pressure in the film. The discretisation in the flow direction is also shown to affect the solution of pressure in the film, particularly at greater rotational speed and eccentricity cases. The ratio of cell size across the film-solid interface is shown to be insignificant to the results for the operational range tested, allowing the mesh size in the solid region to be several magnitudes higher in comparison to the film mesh. The non-dimensionalised parameters in Figures 3.19 and 3.22 can be used to approximate the cell size required in the film region to create a mesh insensitive case.

3.7 Validation And Results

In this section, the numerical methodology described previously in the chapter is applied to a case study of a journal bearing. A description of the case is given with details from the original experimental work. The results produced by the numerical model are compared with the experimental results to show the accuracy and capability of the lubrication model implemented within OpenFOAM.

3.7.1 Case Description

A study is performed comparing the implementation of the Reynolds based TEHL methodology in OpenFOAM against the experimental case from Ferron *et al.* (1983). The experimental work studied the thermodynamic performance of a journal bearing with a single axial supply groove operating across a rotational speed range of 1500-4000rpm and a normal load range of 1000-10000N. Measurements included the pressure along the mid-plane with tappings in the bearing and temperature near the film-bush surface with thermo-couples in the bush. A diagram of the case configuration is shown in Figure 3.23, with the dimensions summarised in Table 3.1.

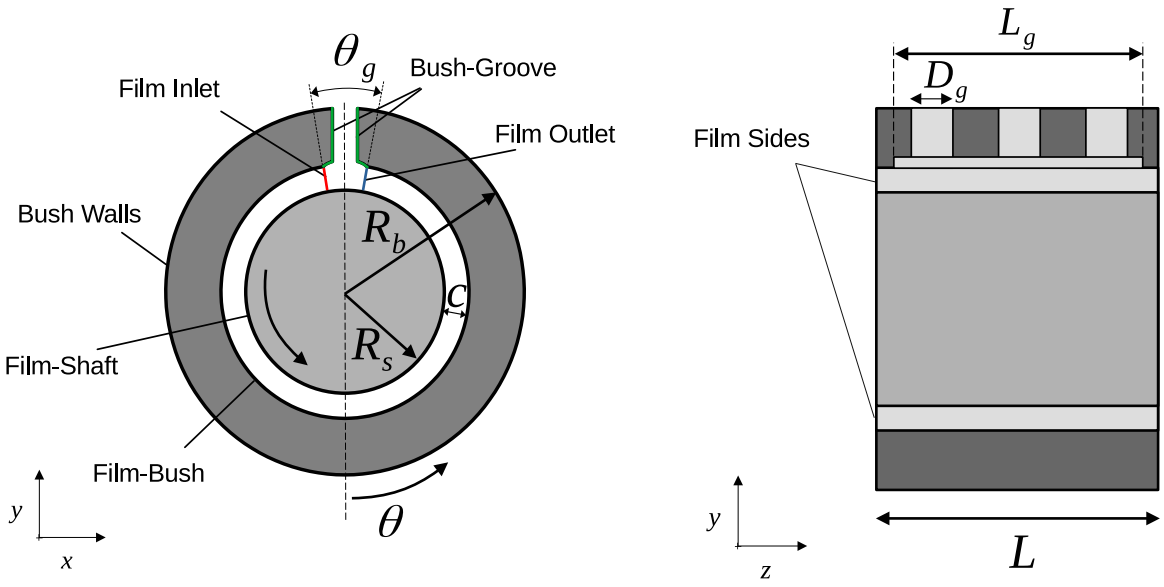

(a) Front View

(b) Side View

Figure 3.23: Diagram depicting the experimental configuration used for validation 44

The material properties for air is used for the vapor phase in the cavitation region. The bush and shaft materials are bronze and steel respectively. Uncertainty of the thermal conductivity of the bush was originally stated in Ferron *et al.* (1983) which used a value of $250\frac{W}{mK}$ and lower values have be used in Banwait & Chandrawat (1998), $100\frac{W}{mK}$, and Stefani & Rebora (2009), $50\frac{W}{mK}$. In this study the bush thermal conductivity is $100\frac{W}{mK}$ which is noted as more representative in Banwait & Chandrawat (1998). The value for material properties of the solids and lubricant are summarised in Table 3.2.

Symbol	Value	Units
P_{cav}	$1x10^3$	Pa
β	$1x10^8$	Pa
ρ_l	860	$\frac{kg}{m^3}$
ρ_g	1.225	$\frac{kg}{m^3}$
c_{p_l}	2000	$\frac{J}{kgK}$
c_{p_g}	1000	$\frac{J}{kgK}$
μ_l	0.0277	Pas
μ_g	$1.918x10^{-5}$	Pas
k_l	0.13	$\frac{W}{mK}$
k_g	0.025	$\frac{W}{mK}$
γ	-0.04	K^{-1}
T_{ref}	40	$^\circ C$
k_b	100	$\frac{W}{mK}$
α_s	$1.2x10^{-5}$	K^{-1}
α_b	$1.8x10^{-5}$	K^{-1}
E_s	200	GPa
E_b	113	GPa
v_s	0.28	-
v_b	0.35	-
h_{walls}	100	$\frac{W}{m^2}$
h_{groove}	1500	$\frac{W}{m^2}$

Table 3.2: Material and Lubricant Properties Ferron *et al.* (1983)

An ordered mesh is used in the film region with 19350 cells with dimensions of approximately 1.3mm and 1mm in the circumferential and axial direction respectively. Across the film height in the 3D film mesh 6 cells are used and the ratio of cell volume across the film-solid interface is 0.175 as shown in Section 3.6. The total number of cells in the bush region is 614979. The bush region is partially structured whereby the mesh is conformal with the film region about the majority of the circumference while an unstructured approach is taken around the more complex geometry near the groove, as shown in the diagram in Figure 3.4.

The groove mixing is modelled using equation 3.34, which is applied as a uniform temperature boundary condition across the film inlet faces. The region of the fluid within the groove is therefore omitted in the mesh as seen in Figure 3.23a. The net-zero heat flux boundary condition is applied at the film-shaft interface with the temperature calculated from equation 3.39.

A parametric sweep is performed using a normal load range of 2-10kN in increments of 1kN and rotational speeds of 1500rpm, 2000rpm, 3000rpm and 4000rpm, replicating the range

tested in Ferron *et al.* (1983). The cases are performed on an 16 cores of AMD 'Genoa' CPUs. The maximum simulation time was 21.5 minutes with an average simulation time across the parametric study of 14 minutes. The total time required to complete all 36 simulations was 8.2hrs.

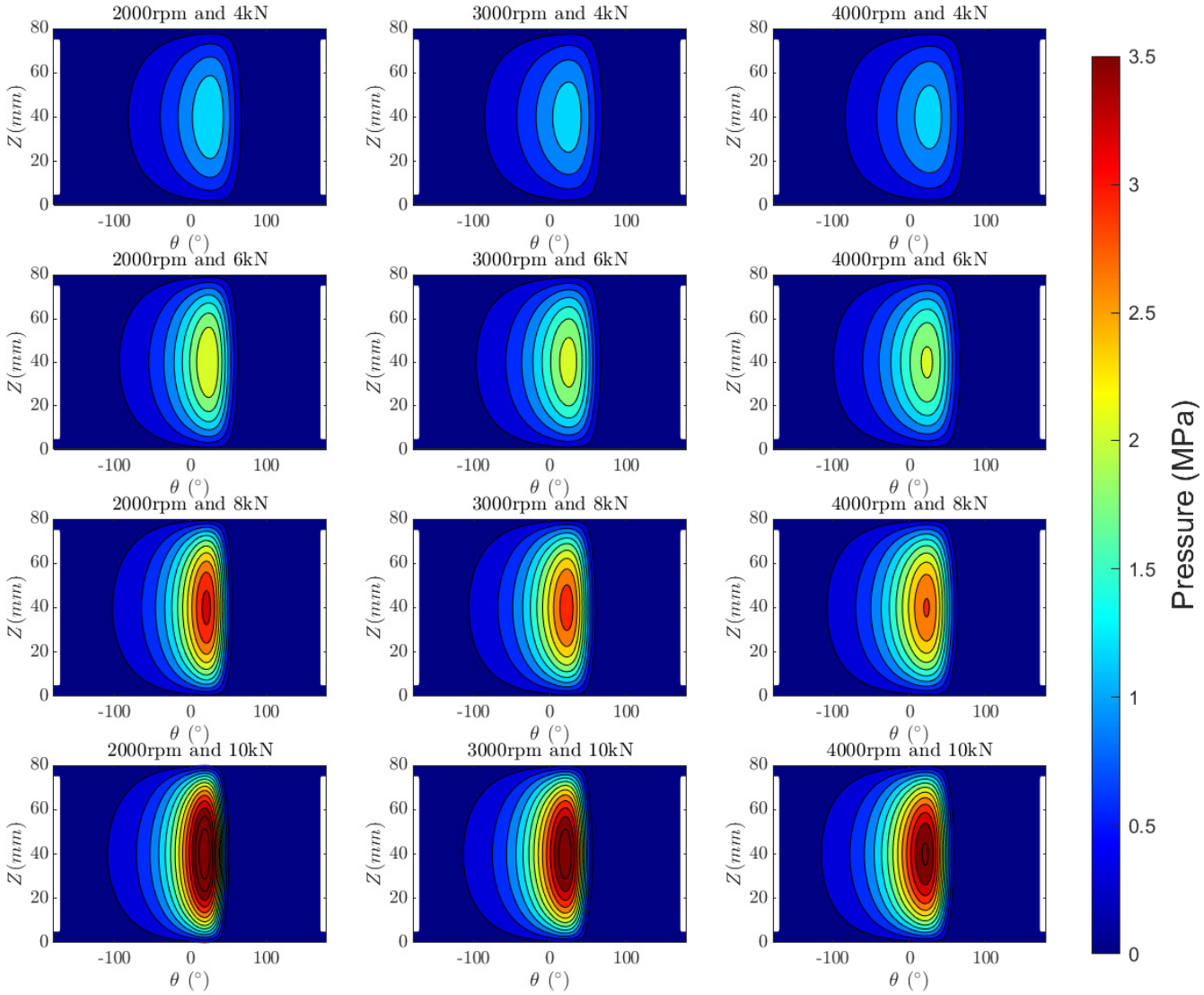

Figure 3.24: Contours of Film Pressure for 2000-4000rpm Rotational Speed and 4-10kN Load

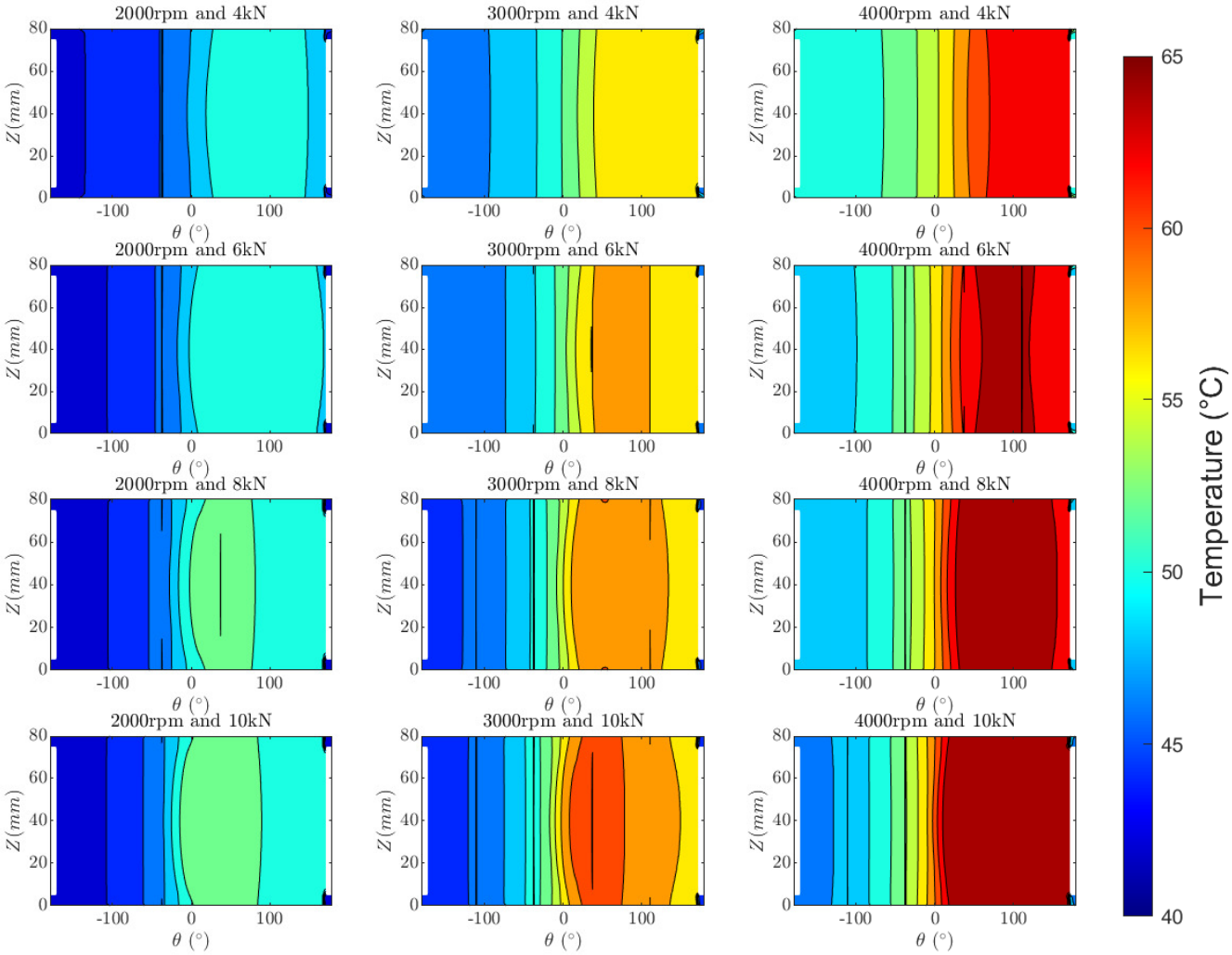

Figure 3.25: Bush-Film Temperature Contours

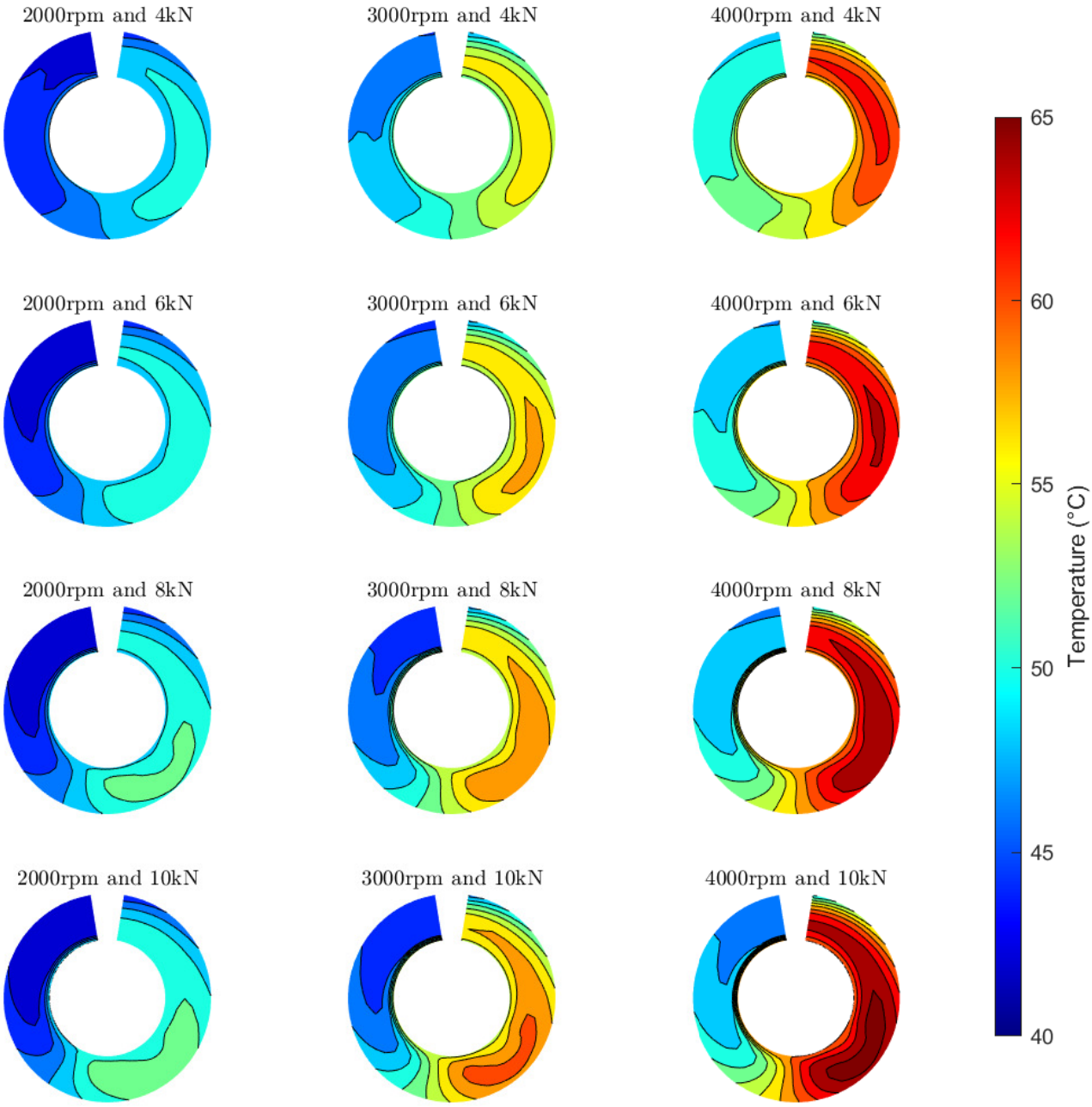

Figure 3.26: Film Centerline Temperature Contours

The fields of temperature and pressure are presented in Figures 3.24, 3.25 and 3.26 as verification for the performance of the methodology implementation in OpenFOAM across the

parameter range. Contours of pressure are shown in Figure 3.24 to present the full profile within the film where the flow is in the positive θ direction. The pattern of peak pressure can be seen where maximum pressure increases with increasing load and decreasing speed. Furthermore, Figure 3.24 shows the trend in the pressure profile to spread as rotational speed is increased and peak pressure decreases. Similarly, the temperature profile across the bush surface is shown in Figure 3.25 where the axial variation in temperature can be seen. The temperature variation in the film is shown in Figure 3.25 along the centreline of the bearing. The same trend in temperature is seen where increasing load and rotational speed increases the maximum temperature. Temperature variation across the film height can be seen and compared.

A comparison of the centreline pressure in the film is shown for two cases; case a at 2000rpm and 4kN in Figure 3.27a and case b at 4000rpm and 6kN in Figure 3.27b. The profiles show good agreement with the experimental measurements which have an experimental uncertainty of 2%. The pressure gradients are near identical increasing to the peak pressure and descending to the minimum film thickness. The location of the peak pressure closely agrees with the experimental results in both cases at 22° and also show agreement in the start of the cavitation region at 80° where the pressure reaches 0MPa. The similarity between peak pressure and cavitation boundary locations is also evidencing good agreement in the prediction of angular position of the shaft by the numerical model. Peak pressure tends to be underestimated due to the reduced bulk modulus values used in the cavitation model, as seen in the centreline profiles where the peak value is underestimated by 3% in case a, Figure 3.27a, and 2% in case b, Figure 3.27b.

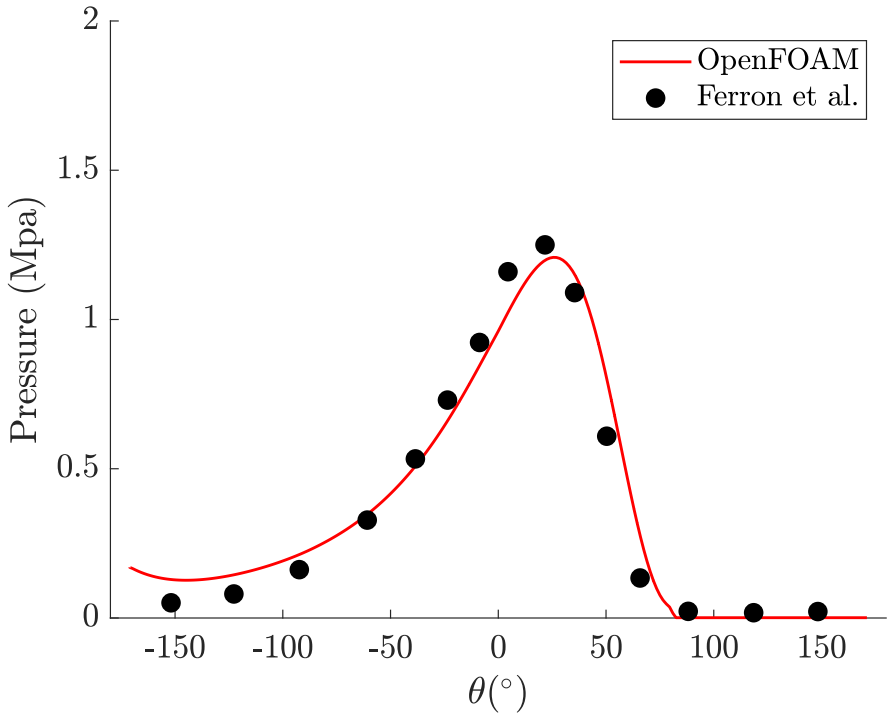

(a) 2000rpm and 4kN

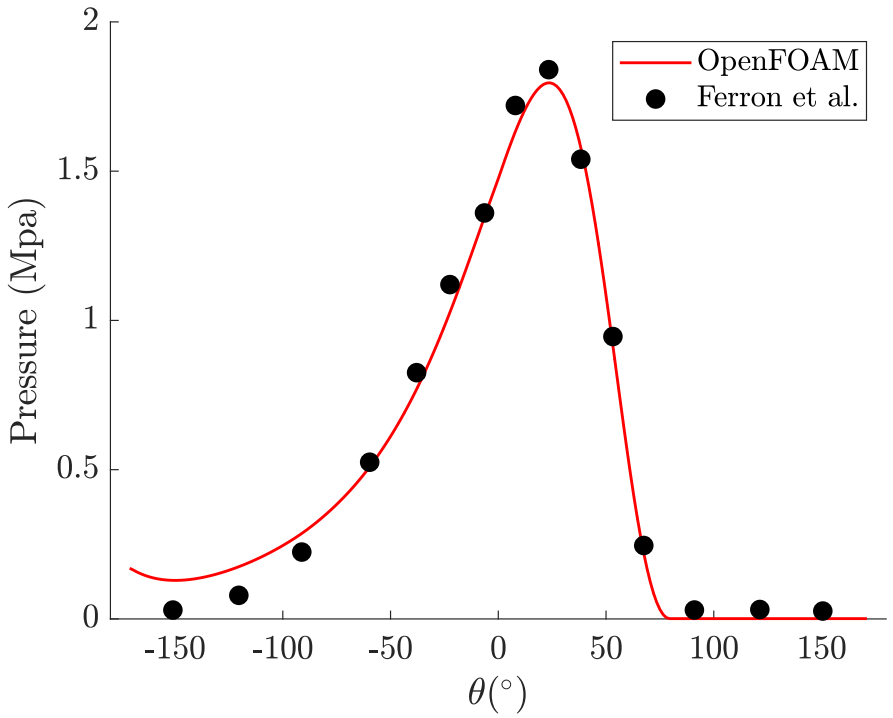

(b) 4000rpm and 6kN

Figure 3.27: Film centerline pressure profiles compared with Ferron *et al.* (1983)

The centreline temperature profiles for the film-bush interface are shown in Figure 3.28. Good agreement is observed in case a at 2000rpm and 4000kN shown in Figure 3.28a, where max-

imum temperature is predicted within 2% of the experimental results. Qualitatively, the temperature profile follows the profile observed in the experimental results where peak temperature is reached downstream of the minimum film height, located at approximately 50°. The temperature gradient increases towards the minimum film thickness before reaching the peak temperature and descending. This pattern is expected from the heat source term in Equation 3.8, which shows that the heat generation will increase non-linearly with as the film height decreases, producing the increasing temperature gradient in the results. The heat generation is also influenced by the viscosity which decreases with temperature, therefore, contributing to reduce the heat generation as the temperature increases. The results show the influence of the viscosity is less significant to the heat generation compared to the film height as the temperature gradient clearly correlates with the behavior expected from the decreasing film height. Case b shows more deviation between the numerical and experimental results, Figure 3.28b, where maximum temperature is overestimated by approximately 8%. The inlet to the film, at angular position -171° in the graphs in Figure 3.28, show the temperature is significantly higher in the numerical model, over-predicting by 12% compared to the experimental case which carries through the temperature profile. There is good qualitative agreement in the temperature profiles, particularly when comparing the temperature difference between inlet and peak values; $15.5^\circ C$ in the OpenFOAM results and $16^\circ C$ in the experimental results. This shows the TEHL model is effective at predicting the temperature rise in the film and the difference could be attributed to inaccurately predicting the temperature of the fluid at the inlet to the film.

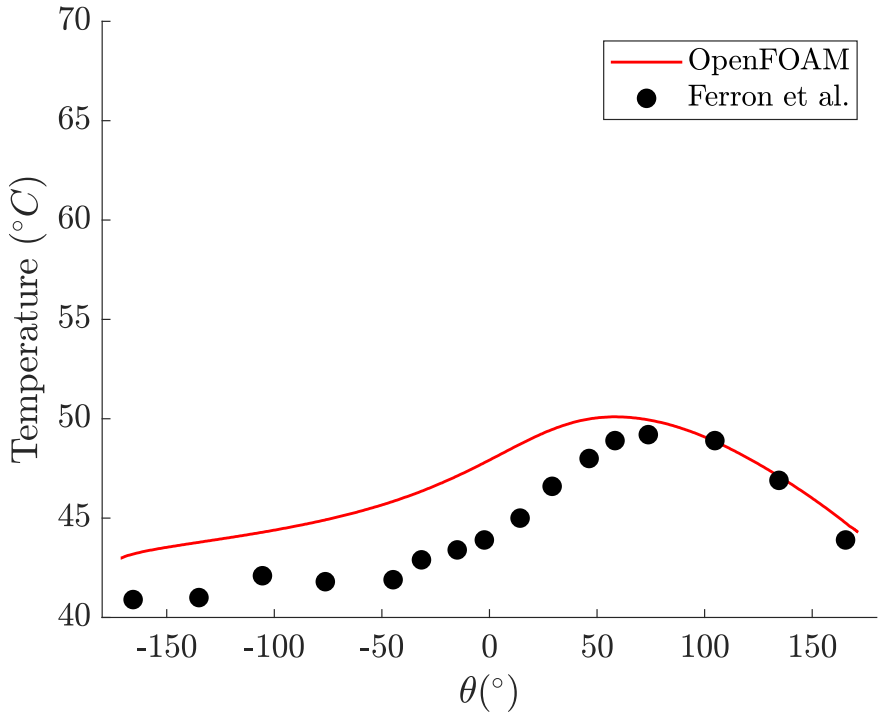

(a)

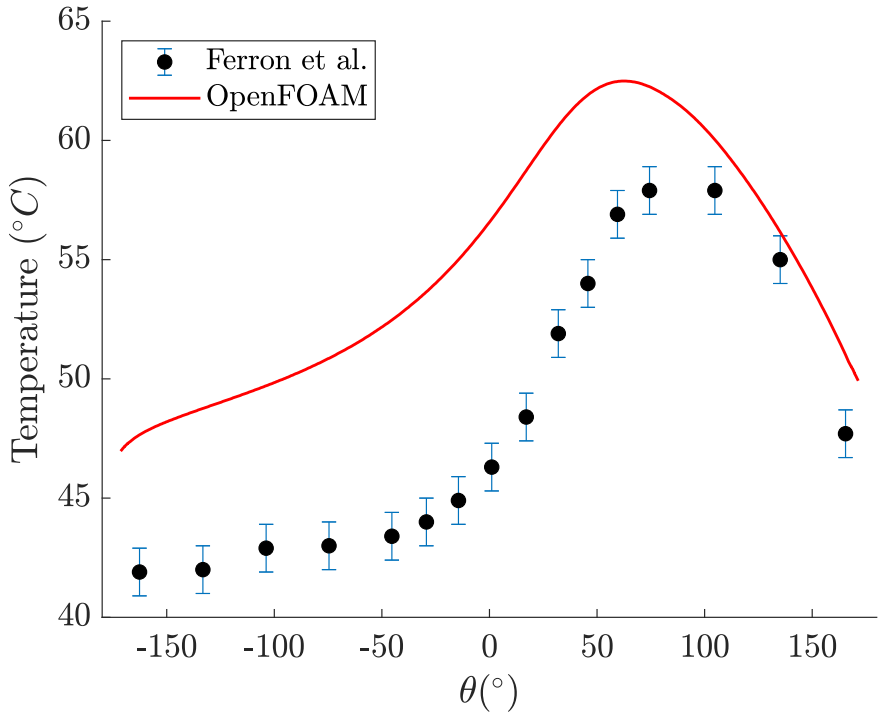

(b)

Figure 3.28: Bush-Film Interface Centerline Temperature Profiles Compared with Ferron *et al.* (1983): a) 2000rpm and 4kN, b) 4000rpm and 6kN.

Temperature of the fluid at the film inlet is calculated in the OpenFOAM model by applying energy continuity between the outlet, inlet and supply using equation 3.34, therefore, approxi-

mating the effect of mixing in the groove without resolving the flow. This temperature boundary is applied as a uniform value across the interface, whereas the flow in the groove could produce a non-uniform profile, affecting the temperature solution in the film. Furthermore, free convection is assumed at the bush-groove interface, however, this heat transfer is not included in the inlet temperature calculation for the film region. As the heat transfer between the bush and supply oil fed into the groove is not incorporated, the energy is not fully conserved in the solution. These factors could affect the film inlet temperature and the temperature solution in the bush given the convection coefficient is estimated from previous studies, which may contribute to the difference in temperature results seen in Figure 3.28. Applying a CFD methodology to resolve the flow in the groove region could provide a physical representation of the fluid mixing between the supply and recirculating oil to improve the inlet temperature of the film and the solution of the bush temperature by better considering the grooves cooling effect.

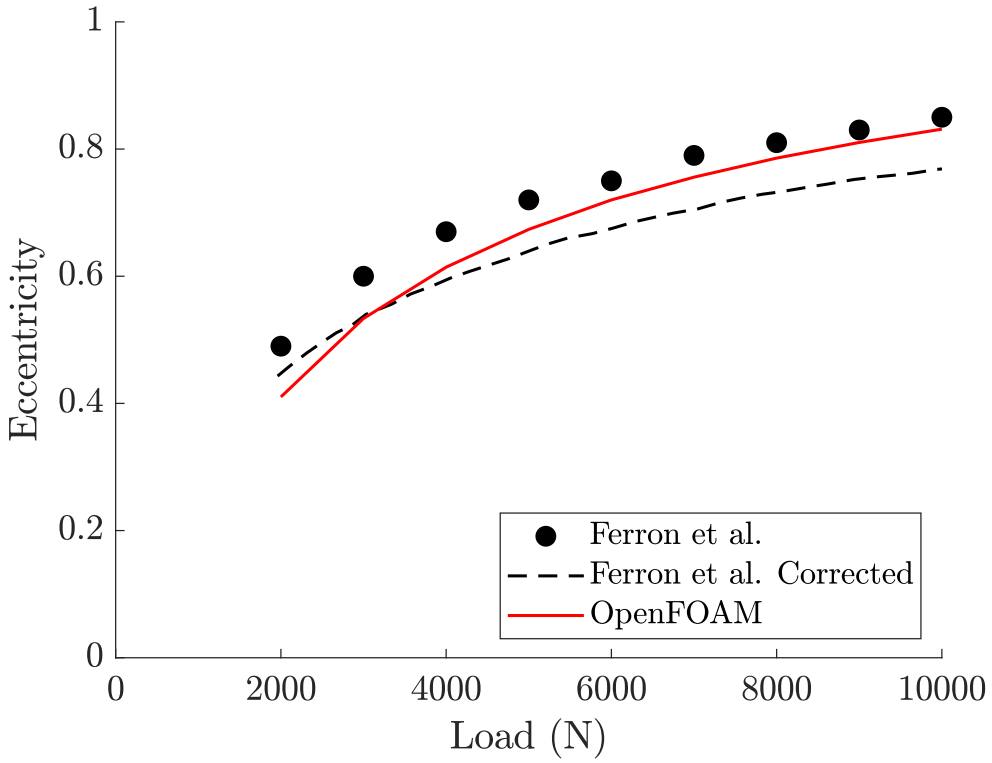

Figure 3.29: Eccentricity Against Load At 2000rpm Compared with Ferron *et al.* (1983)

The relation between eccentricity and load is presented in Figure 3.29 compared against the results from Ferron *et al.* (1983). The experimental eccentricity is calculated using the clearance in the original study and some uncertainty is noted on this values due to the thermal

expansion of the solid components during operation. An adjusted clearance value of $152\mu m$ was estimated in the original study by assuming a higher temperature in the shaft and bush during operation. The adjusted clearance is used in the eccentricity measurements to produced the Corrected eccentricity dataset in Figure 3.29. Details of the adjusted experimental eccentricity is given in Ferron *et al.* (1983). The OpenFOAM eccentricity prediction shows good agreement with the original eccentricity results from Ferron *et al.* (1983) before the correction is applied. The difference in the eccentricity prediction and the corrected values is greater at higher load, however there is significant uncertainty in the measurements of eccentricity in the experimental case. The corrected eccentricity values are used in the experimental results in Figures 3.30 and 3.31. The difference between the numerical and experimental eccentricity is similarly observed to be greater at higher load and explains the horizontal deviation of the results in Figures 3.30 and 3.31.

A comparison of the peak pressure in the film against the shaft eccentricity is shown in Figure 3.30. The peak pressure is predicted generally within 2% where at higher eccentricity, corresponding to higher load, the peak pressure begins to be underestimated. Similarly, the peak temperature values for the bush-film interface are compared with experimental results in Figure 3.31. The trend in maximum bush temperature is in good agreement between the numerical and experimental results. At higher rotational speed the maximum bush temperature shows more deviation with the experimental results, where at 1500rpm the temperature is within 1% while at 4000rpm the temperature is within 6%. There is greater agreement at higher eccentricity, relating to higher loads, which is seen across the range of rotational speeds. The results show that the numerical is less effective for cases with greater heat generation which could reflect the observation of the temperature profile in Figure 3.28 where the inlet temperature is over-predicted. Improving the inlet temperature prediction could bring more alignment with the experimental results at higher rotational speed and load cases where there is an expected higher temperature rise in the film.

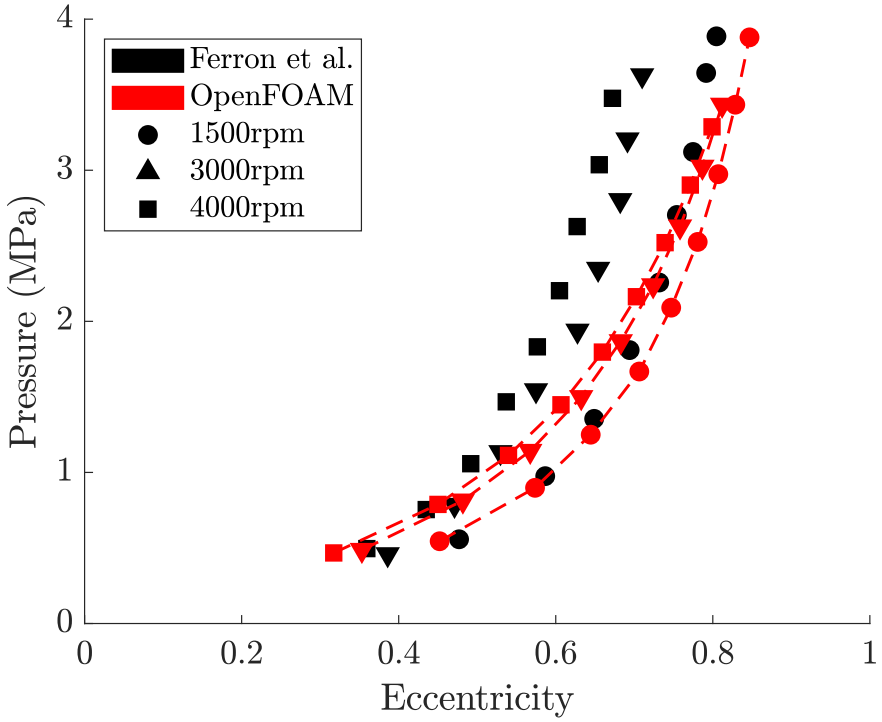

Figure 3.30: Peak Pressure in the Film

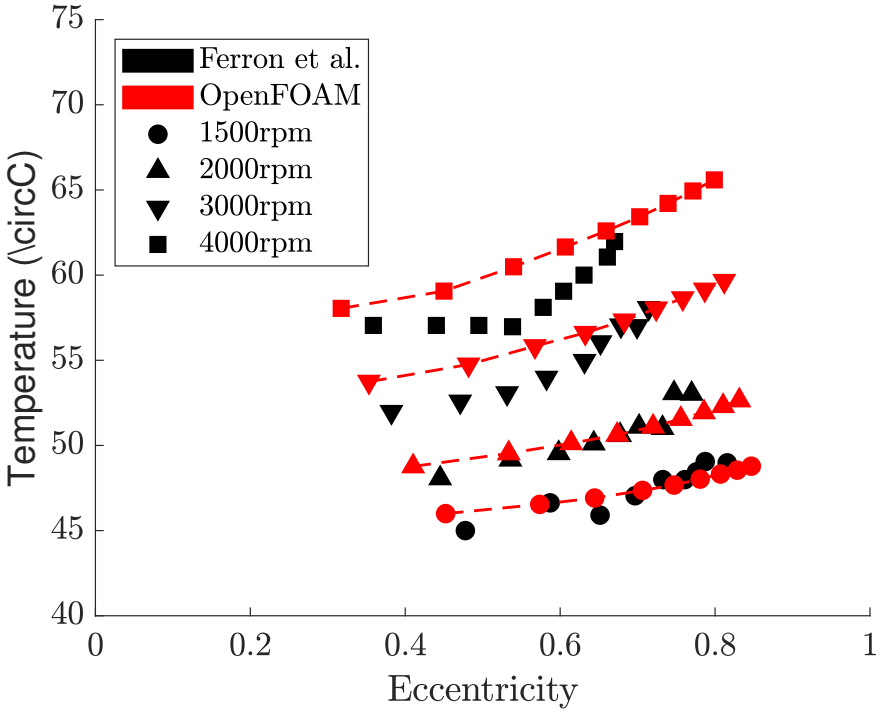

Figure 3.31: Peak Temperature on the Film-Bush Interface

The parametric study comparing the OpenFOAM models results of a single axial groove journal bearing to the experimental results from Ferron *et al.* (1983) validates the model and

demonstrates the performance for the tested parameter range. Good qualitative agreement is observed in the profiles of pressure and temperature with peak value being predicted within 2% and 8% respectively. Temperature at the inlet of the film region is shown to be over-estimated by the TEHL OpenFOAM model which impacts the temperature results at higher rotational speeds and load. Improving the inlet boundary condition to the film by resolving the flow within the supply groove could enhance the accuracy of the model under higher rotational speed and load conditions.

Chapter 4

TEHL-CFD Coupling Methodology

This Chapter describes the CFD methodology implemented in OpenFOAM which interfaces with the TEHL methodology described in Chapter 3 and is applied to simulate a journal bearing with the numerical setup presented in Figure 4.1. The governing equations are presented including the conservation equations, turbulence models, fluid rheology and multiphase methodology. A case study is developed of a two-dimensional journal bearing to investigate the interfacing methodology between the CFD and TEHL regions. A mesh sensitivity study is also performed to demonstrate the effect of cell density on the solution in the two-dimensional setup which can inform the initial setup of three-dimensional cases to follow on from the case study.

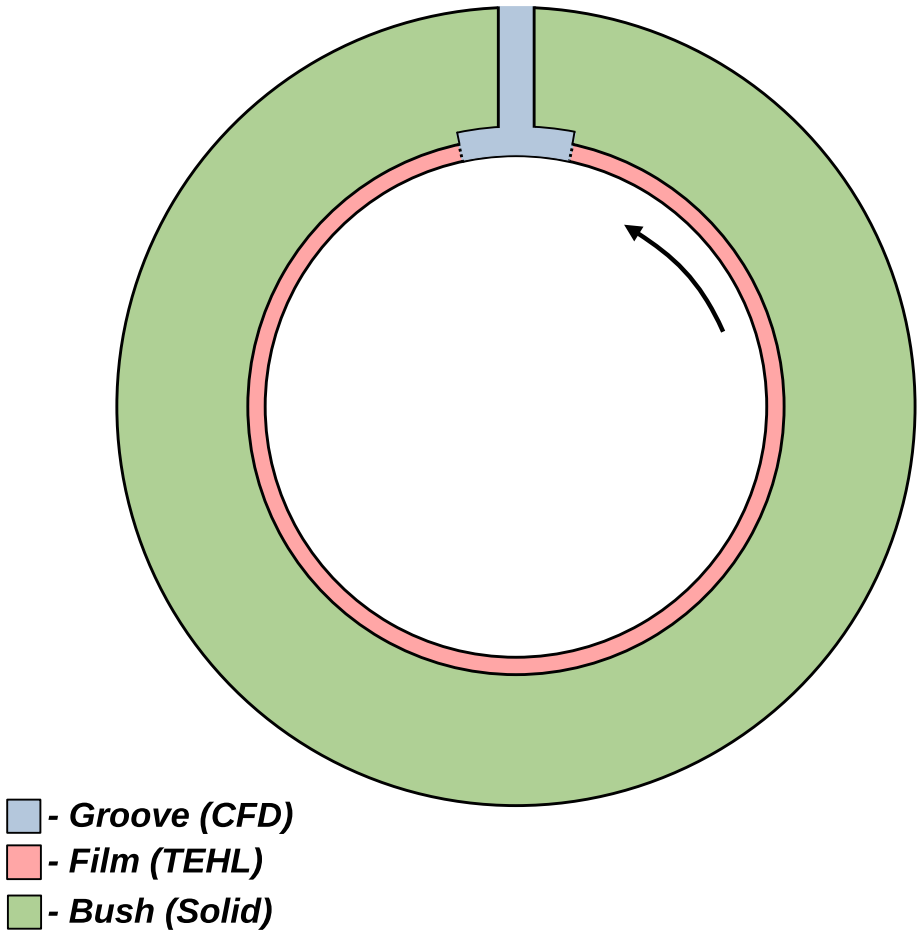

Figure 4.1: Proposed multi-region setup of a journal bearing simulation including the supply groove

4.1 CFD Governing Equations

In this section, the governing equations for the fluid model are presented which are the Navier-Stokes equations. An equation for conservation of energy is also applied which considered the thermal effects in the fluid region. Turbulence models are also presented which are considered later in the chapter. The Volume-of-Fluid (VoF) model is overviewed here as there is a short study towards the end of the thesis which considers multi-phase effects in the fluid model.

4.1.1 Conservation Equations

The behaviour of viscous fluids is governed by the Navier-Stokes equations. Applying the principle of conservation of mass to a control volume derives Equation 4.1 presented in matrix form.

$$\frac{\partial \rho}{\partial t} + \nabla \cdot (\rho U) = 0 \tag{4.1}$$

where ρ is the density of the fluid, U is the fluid velocity and t is the time variable. Similarly, conservation of momentum derives Equation 4.2.

$$\frac{\partial}{\partial t}(\rho U) + \nabla \cdot (\rho UU) = \nabla \cdot (\mu \nabla U) - \nabla P + \nabla \cdot \left(\mu \left(\nabla U\right)^T\right) - \frac{2}{3}\nabla (\mu \nabla \cdot U) \tag{4.2}$$

Conservation of energy is applied for the temperature in the fluid using Equation 4.3:

$$\frac{\partial}{\partial t}(c_p \rho T) = -\nabla \cdot (\rho c_p U T) + \nabla \cdot (k \nabla T) \tag{4.3}$$

4.1.2 Turbulence Models

Turbulence effects have been included in numerical models such as Kosasih & Tieu (2004) in the groove of a journal bearing which showed greater qualitative comparison with the flow observed in the region in experimental investigations. The mixing effects in the groove is a significant factor affecting the temperature of fluid entering the film region, therefore the diffusive effect of turbulent flow could have a significant effect on the solution and should be considered in the numerical model.

The Reynolds Averaged Navier-Stokes (RANS) turbulence methodology is applied in the current model which was originally described in Reynolds (1885). This approach separates the flow into a mean ($\bar{u}(x)$) and fluctuating component ($u'(x,t)$) as shown in Equation 4.4.

$$u(x,t) = \bar{u}(x) + u'(x,t) \tag{4.4}$$

It is also assumed that the mean of the fluctuating component is 0

$$\bar{u'}(x,t) = 0 \tag{4.5}$$

Applying to the Navier-Stokes equations derives Equation 4.6 and 4.7 for mass and momentum continuity in terms of the mean pressure and velocity.

$$\frac{\partial \rho}{\partial t} + \nabla \cdot (\rho \bar{u}) = 0 \tag{4.6}$$

$$\frac{\partial \rho \bar{u}}{\partial t} + \nabla \cdot (\rho \bar{u} \otimes \bar{u}) = g + \nabla \cdot (\bar{\tau}) - \nabla \cdot (\rho R) \tag{4.7}$$

where $\bar{\tau}$ is the averaged stress tensor and R is the Reynolds stress tensor.

The $k-\varepsilon$ and $k-\omega$ models are compared along with the laminar case when validating the CFD model. The $k-\varepsilon$ model presented in Equation 4.8 is a two-equation model for turbulence which models the turbulent kinetic energy, k, and the turbulent dissipation rate, ε:

$$\begin{aligned} \frac{D}{Dt}(\rho k) &= \nabla \cdot (\rho D_k \nabla k) + P - \rho \varepsilon \\ \frac{D}{Dt}(\rho \varepsilon) &= \nabla \cdot (\rho D_\varepsilon \nabla \varepsilon) + \frac{C_1 \varepsilon}{k}\left(P + C_3 \frac{2}{3} k \nabla \cdot U\right) - C_2 \rho \frac{\varepsilon^2}{k} \end{aligned} \tag{4.8}$$

where D_k is the effective diffusivity for k, P is the turbulent kinetic energy production rate, D_ε is the effective diffusivity for ε and C_1, C_2 and C_3 are model coefficients. The $k-\omega$ model is a similar two-equation model for turbulence which models the turbulent kinetic energy, k, and the turbulent specific dissipation rate, ω. Similar to the $k-\varepsilon$ equations, the $k-\omega$ model is widely applied for turbulent regimes and is notable for good performance near walls:

$$\begin{aligned} \frac{D}{Dt}(\rho k) &= \nabla \cdot (\rho D_k \nabla k) + P - \rho \omega \\ \frac{D}{Dt}(\rho \omega) &= \nabla \cdot (\rho D_\omega \nabla \omega)_{\frac{C_1 \varepsilon}{k}}\left(P + C_3 \frac{2}{3} k \nabla \cdot U\right) - C_2 \rho \frac{\omega^2}{k} \end{aligned} \tag{4.9}$$

4.1.3 Multi-phase Volume Of Fluid Methodology

The multiphase flow caused by the ejection of fluid from hydrodynamic lubrication regions in an influential factor in transmission systems. Berthold *et al.* (2018) developed a CFD model for the simulating the disintegration of oil from the sides of journal bearings. The mode of disintegration effects the droplet size produced which influences the aerodynamic and thermal performance of the wider system. The numerical study highlights the oil viscosity, which is dependent on oil temperature, significantly effects the mode of disintegration. The heat generated in the oil as it passes through the bearing is therefore connected to the oil disintegration behaviour in this scenario. This example highlights the connection between hydrodynamic lubrication regions and multiphase flow behaviour in the wider domain, and shows the value for including multiphase modeling capability in the CFD methodology.

The volume-of-fluid (VoF) method assumes there are multiple immisible phases in the domain with a defined interface between them. The density across the domain for a two-phase system is calculated from volume fractions of each phase:

$$\rho = \alpha\rho_1 + (1-\alpha)\rho_2 \tag{4.10}$$

where α is the volume fraction of phase 1, ρ_1 is the density of phase 1 and ρ_2 is the density of phase 2. Surface tension of the liquid phase is included with the equation:

$$f_{\sigma i} = \sigma k \frac{\partial \alpha}{\partial x} \tag{4.11}$$

where $f_{\sigma i}$ is the surface tension force, σ is the surface tension constant and k is the curvature. The curvature k is estimated from the equation:

$$k = -\frac{\partial}{\partial x_i}\left(\frac{\partial \alpha}{|\partial \alpha|}\right) \tag{4.12}$$

The equation for the inter-phase between the fluids is:

$$\frac{\partial \alpha}{\partial t} + \frac{(\alpha u_j)}{\partial x_j} = 0 \tag{4.13}$$

Multi-phase effects are not considered in the journal bearing simulations including the groove region in the following sections. The bearings are assumed to be fully supplied and film reformation occurs upstream of the supply groove in the film. The VoF multiphase model is later introduced into the simulation of a half-journal bearing experimental rig presented in Section 5.2.

4.2 Preliminary Boundary Condition Setup

This section describes the initial boundary conditions applied in the CFD region including justifications for the setup considering the methodology and assumptions of the TEHL model. This setup is formulated by basic assumptions at the interfaces as an initial setup for the coupling between the numerical models. In the following section, a case study is conducted which applies this approach and the solutions are shown not to be smooth across the interface. In Section 4.3, the interface coupling is reformulated but the initial setup is presented here to justify the final numerical setup.

Figure 4.2 shows a schematic of the two-dimensional journal bearing case study used to investigate the coupling methodology. The regions are identified and the boundaries are labelled including the boundaries interfacing CFD and TEHL: Groove to Film Inlet and Groove to Film Outlet.

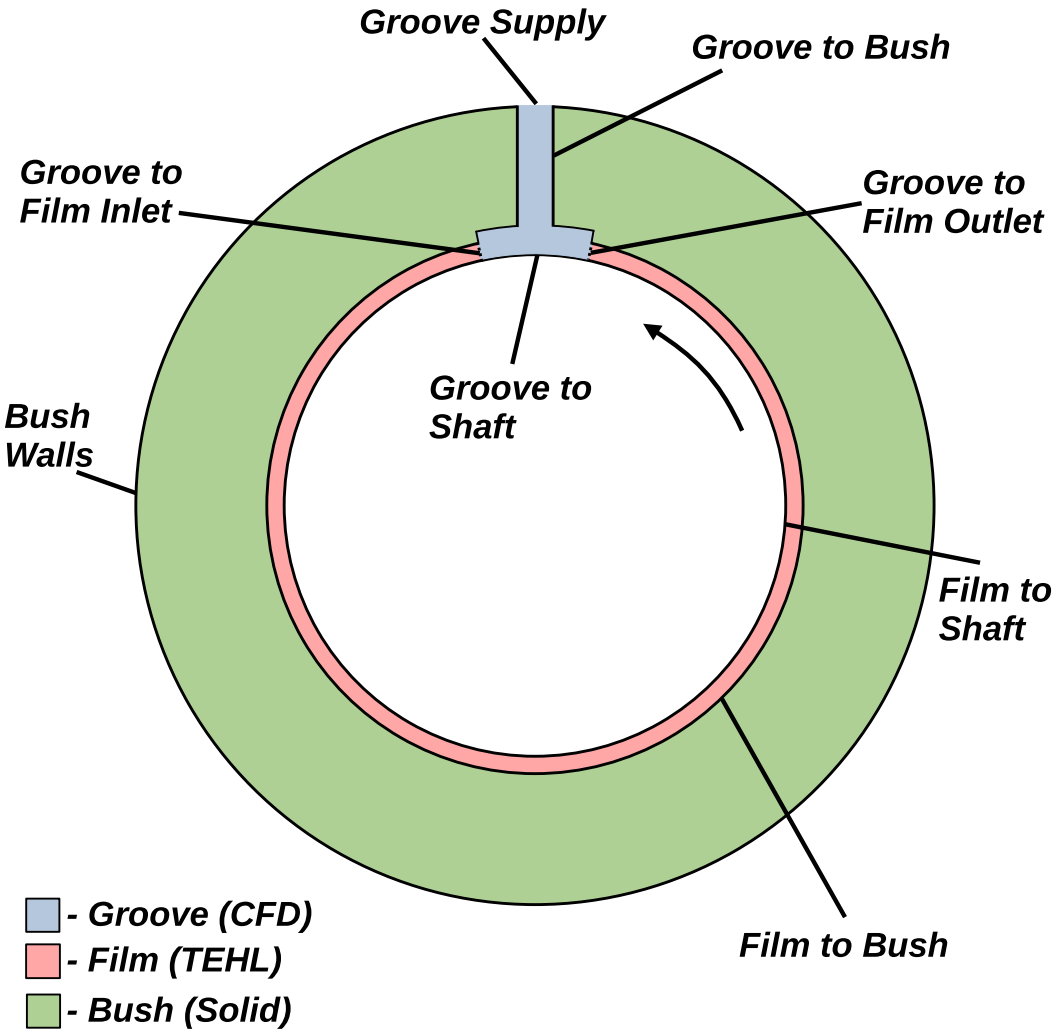

Figure 4.2: Diagram of the 2D journal bearing

4.2.1 CFD to TEHL Interfaces

The interfaces between the CFD and TEHL models interpolate the latest solution from the adjacent region to the boundary faces, as depicted in Figure 4.3. Continuity across these interfaces is important in generating a numerical solution for the system. Continuity of the variables in the CFD region is important for the accuracy of the CFD solution, which includes mass, momentum and energy.

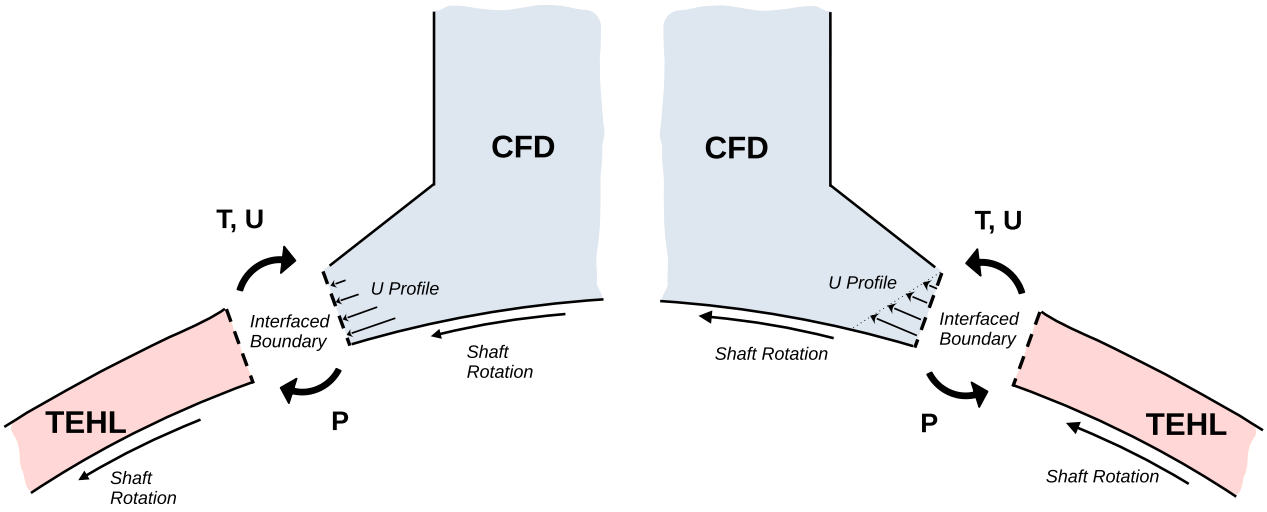

(a) (b)

Figure 4.3: TEHL-CFD coupling setup for; a) Inlet to the TEHL region, b) Outlet from the TEHL region

4.2.1.1 Pressure and Velocity

The information required to be transferred between regions varies with the underlying assumptions which derive the governing equations. The TEHL model produces a solution for the pressure and temperature fields, from which the film thickness, lubricant rheology and velocity field are explicitly calculated. The TEHL model, therefore, is effected by the CFD region primarily through the pressure and temperature fields at the interfaces. Within the CFD methodology, the solution for velocity is found from the three-equations for momentum, Equation 4.2, which means boundary conditions are required for mass flow at the interfaces with the TEHL region. Given the velocity field is based on the pressure solution in the TEHL region (i.e. the velocity field is derived from the solution of the Reynolds Equation 3.1), coupling of the velocity field is applied one-way from the TEHL region to the CFD as a Dirichlet condition, where a value is prescribed to the boundary face:

$$\phi_b = \phi_c \tag{4.14}$$

where ϕ_b is the variable value on the boundary face and ϕ_c is a constant value of the variable ϕ.

The pressure at the interfaces between CFD and TEHL is unknown and a Von Neuman boundary condition for the pressure is applied which defines a fixed gradient to the boundary face:

$$\frac{\partial \phi_b}{\partial \mathbf{n}} = \phi_c' \tag{4.15}$$

where ϕ_c' is a constant gradient value for the variable ϕ. The pressure solution at the boundary is then communicated to the TEHL boundary as a Dirichlet condition where the face has a fixed value in the numerical model. This setup effectively creates an iterative pressure-velocity coupling at the region level between the TEHL and CFD models that converges to a coupled solution.

4.2.1.2 Temperature

The highly advective nature of TEHL regimes means the energy transfer between the TEHL and CFD regions is dominated by convection, and the boundary condition is dependent on the direction of flow across the interface. In the preliminary boundary condition setup the flow direction is assumed at the interfaces, depending on the direction of motion of the shaft wall, and the temperature solution is coupled one-way between the regions depending on the assumed direction. At the inlet to the TEHL region, Figure 4.3a, the direction of flow is assumed to be entirely into the film region from the CFD region, and the temperature boundary condition for the CFD region is a Neuman setup with a gradient of 0, and a Dirichlet setup in the TEHL region where the value is interpolated from the CFD region. Similarly, at the TEHL outlet the direction of flow is assumed to be entirely from the TEHL region to the CFD region, and the temperature boundary condition for the TEHL region is a Neuman setup, and a Dirichlet setup in the CFD region where the value is interpolated from the TEHL region.

4.2.2 CFD to Solid Interface

The temperature is the single variable which is coupled between the CFD and solid regions. The two-way coupled heat flux continuity model from equation 3.35 is applied between these regions to enforce continuity of the temperature solution between the regions.

4.2.3 CFD Oil Supply

Variable	Type	Value
Pressure	Dirichlet	P_{supply}
Temperature	Dirichlet	T_{supply}
Velocity (Tangential)	Dirichlet	0
Velocity (Normal)	Neuman	0

Table 4.1: Boundary condition setup for the oil supply in the CFD region

The Dirichlet condition of velocity at the CFD to TEHL interfaces requires that the flow rate at the oil supply is flexible to prevent over-restricting the velocity field. This is particularly important for the journal bearing cases where the mass flow of the oil supply is determined by the flow into and out of the film. The numerical setup of velocity for this boundary is applied as a mix between Dirichlet and Neuman conditions. The direction of the flow is assumed to be normal to the boundary and a Neuman condition is applied perpendicular to the boundary, while a Dirichlet condition is applied tangentially, as summarised in Table 4.1. This setup gives flexibility for the mass flow to be determined at the lubricant supply boundary.

4.3 CFD To TEHL Coupling Strategy And Evaluation

This section investigates the coupling methodology between the CFD and TEHL regions and the setups effect on the solution. The initial methodology from Section 4.2 is first applied and the results discussed. The methodology is then reformulated to improve the solution across the interface. A grid resolution study is also performed to assess the sensitivity of the CFD solution to the mesh.

4.3.1 Case Setup

A two-dimensional journal bearing case is setup which includes the groove region modelled using the CFD methodology to verify the performance of the coupling approach between the TEHL and CFD regions. A diagram of the geometry is shown in Figure 4.4 with parameters summarised in Table 4.2.

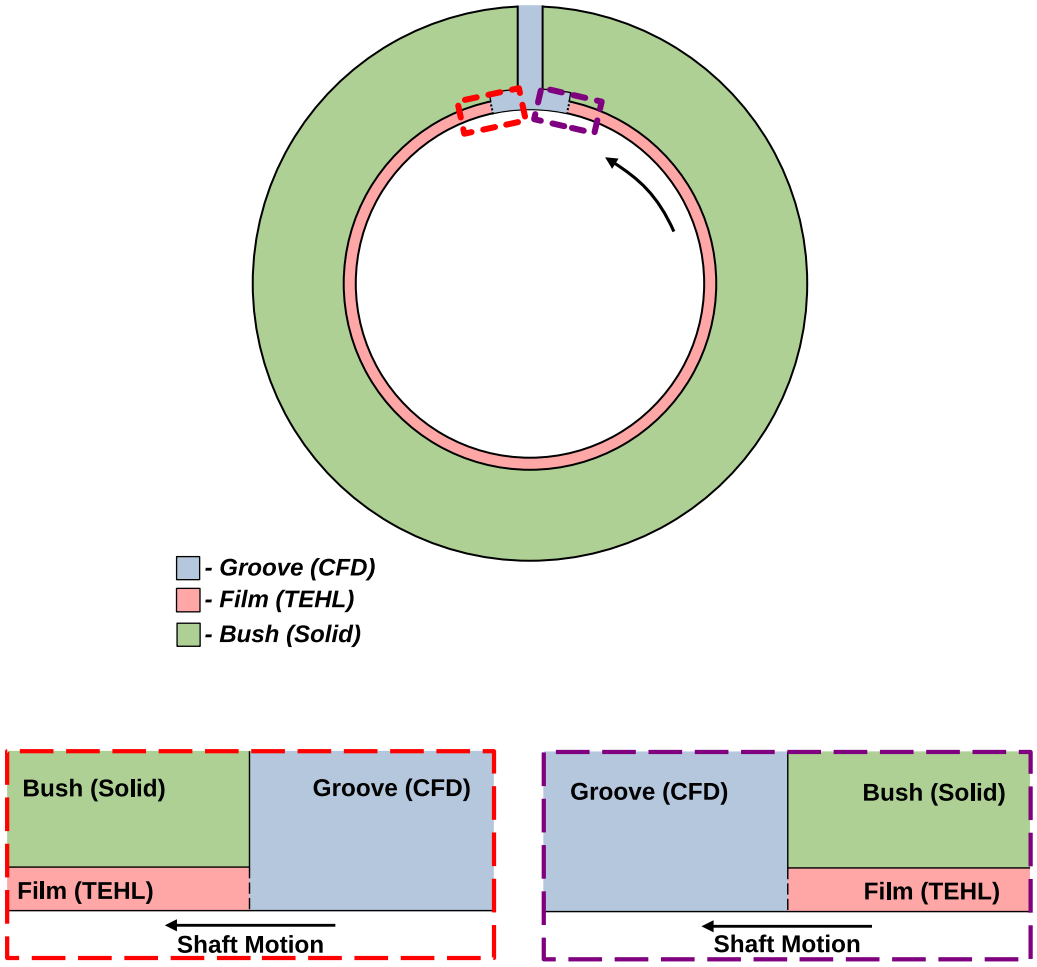

(a) View 1 (Film Inlet) (b) View 2 (Film Outlet)

Figure 4.4: 2D journal bearing with a CFD groove region interfaced with the film (TEHL) and bush regions

The program requires a three-dimensional mesh, therefore, the length of the bearing is noted in Table 4.2 and a single cell discretisation is applied in the axial direction with boundary conditions setup to apply the two-dimensional nature in the simulations. The groove shape is simplified to a rectangular profile as seen in Figure 4.5 to accelerate the mesh generation and

provide flexibility to varying the geometry and mesh parameters.

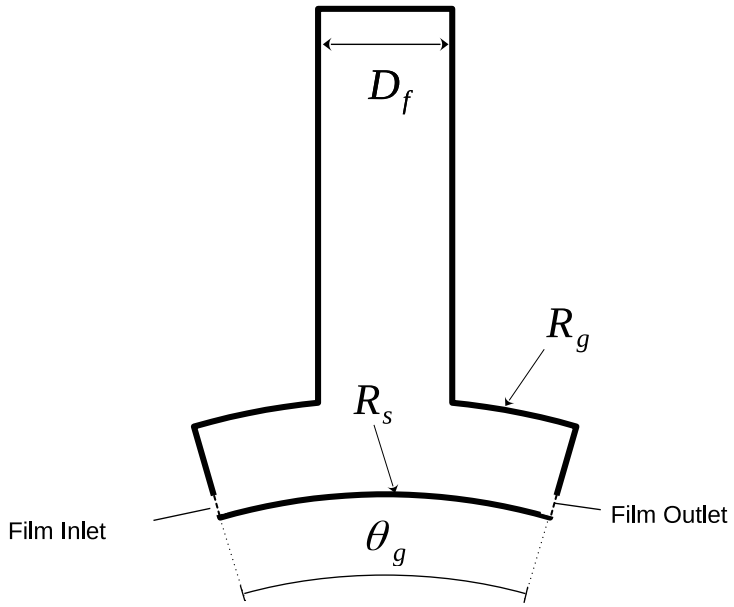

Figure 4.5: Groove geometry parameters

Property	Symbol	Value
Shaft Radius (mm)	R_s	50
Bush Radius (mm)	R_b	100
Bush Length (mm)	L	0.1
Clearance (μm)	c	100
Groove Angle (°)	θ_g	18
Groove Radius (mm)	R_g	54.1
Feed Hole Diameter (mm)	D_f	5

Table 4.2: 2D journal bearing geometric parameters

4.3.1.1 Interface Coupling Results

The two-dimensional journal bearing case study is performed to test the interfacing methodology between the CFD and TEHL regions. The properties of the fluid and solid material are listed in Table 4.3 and the operational parameters in Table 4.4. The initial setup of the operational parameters in Table 4.4 are estimated based on the results of the journal bearing study in Ferron *et al.* (1983) to reflect realistic operating conditions. In the TEHL region, the Elrod-Adam cavitation model is applied assuming vapor cavitation as the primary mechanism, the energy equation is included with temperature dependent viscosity and deformation of the solids is excluded assuming it is insignificant to the performance of the coupling methodology.

Property	Value	Unit
P_{vapor}	$1x10^3$	Pa
β	$1x10^8$	Pa
ρ_l	860	$\frac{kg}{m^3}$
ρ_g	1.225	$\frac{kg}{m^3}$
c_{p_l}	2000	$\frac{J}{kgK}$
c_{p_g}	1000	$\frac{J}{kgK}$
μ_l	0.0277	Pas
μ_g	$1.918x10^{-5}$	Pas
k_l	0.13	$\frac{W}{mK}$
k_g	0.025	$\frac{W}{mK}$
γ	-0.04	K^{-1}
T_{ref}	40	$^\circ C$
k_s	50	$\frac{W}{mK}$
k_b	50	$\frac{W}{mK}$
E_s	200	GPa
E_b	113	GPa
v_s	0.28	-
v_b	0.35	-
h_{walls}	50	$\frac{W}{m^2}$

Table 4.3: Material properties of the lubricant and solids

Parameter	Value
P_{supply}	70 kPa
Rotational Speed	1000 rpm
Eccentricity	0.6
Shaft Angular Offset	0°

Table 4.4: Operational parameters

The interfacing boundaries are categorised as the film inlet boundary, where the rotation of the shaft drives fluid into the film region, and the film outlet boundary, where the rotation of the shaft drives fluid out of the film region. There are 3 variables which are coupled between the groove and film regions: pressure, temperature and velocity. Justification for the boundary condition setup is described in Section 4.2 and a summary of the interfacing is shown in Table 4.5 from the perspective of each region.

Variable	TEHL		CFD	
	Film Inlet	**Film Outlet**	**Film Inlet**	**Film Outlet**
Pressure	Dirichlet *(From CFD)*	Dirichlet *(From CFD)*	Neuman *(Value 0)*	Neuman *(Value 0)*
Temperature	Dirichlet *(From CFD)*	Neuman *(Value 0)*	Neuman *(Value 0)*	Dirichlet *(From TEHL)*
Velocity	N/A	N/A	Dirichlet *(From CFD)*	Dirichlet *(From CFD)*

Table 4.5: Summary of the interfacing boundary conditions between CFD and TEHL regions

4.3.2 Mesh Sensitivity

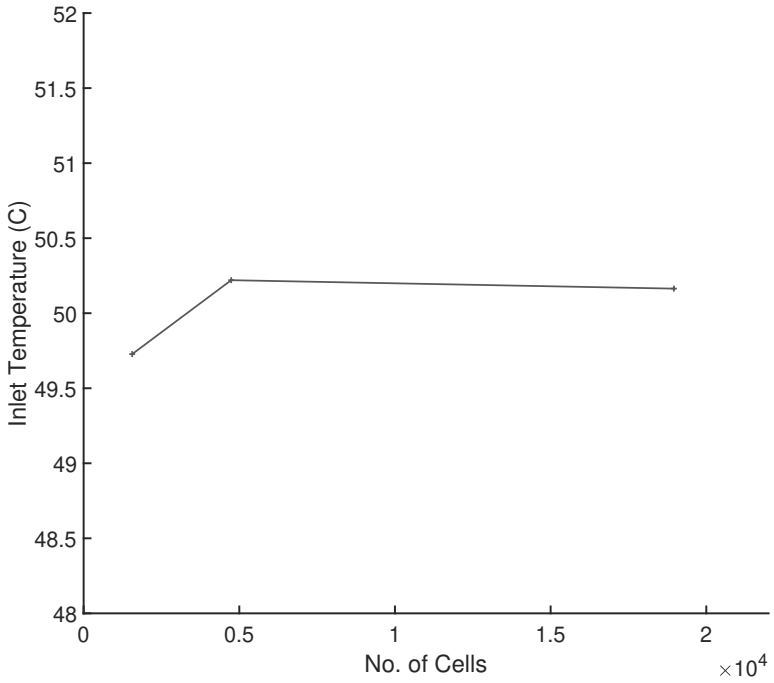

Figure 4.6: Sensitivity study comparing the film inlet temperature against the mesh size for the supply groove

A study of the sensitivity of the solution in the groove region, which applies the CFD methodology, to the mesh is performed on the case described in Section 4.3.1 with the operating parameters in Table 4.4. An ordered mesh is constructed which is more refined towards the interfaces with the film and shaft surface. The film inlet temperature is chosen as the parameter of interest in the study given its influence on the temperature solution in the film and considering the CFD methodology in the groove is to be compared to the approximate method to the

inlet temperature described in Equation 3.34. The number of cells in the mesh is used as the parameter to represent the mesh density in the groove and the results are shown in Figure 4.6. The results show the solution is insensitive to the mesh density at approximately 4740 cells, with a relative error from the lower density mesh of 1560 cells of 1%, and a relative error with the higher density mesh 18960 cells of 0.12%.

4.3.2.1 Initial Boundary Condition Setup Results

The methodology described in section 4.2 is applied to the two dimensional case study which assumes the fluid flows entirely from the groove into the film at the inlet, and from the film to the groove at the outlet. This is reflected in the pressure and temperature boundaries which are Dirichlet conditions with values taken from the latest solution of the CFD region. Figure 4.7a shows the pressure field across the film inlet interface between TEHL and CFD regions. The single cell discretisation in the TEHL region across the height of the film means the pressure value at the interface is the averaged value from the CFD boundary, which can be observed in Figure 4.7a by the non-uniform pressure profile in the groove region tangential to the film interface.

The temperature profile around the film inlet is shown in Figure 4.7c between the film, groove and bush regions. The solution is highly discontinuous at the interface between film and groove regions where there is a high temperature towards the top of the film. The cause of this can be seen in Figure 4.7e showing the magnitude and vector field of velocity around the interface. In the film region, there is a reverse flow from the film into the groove which conflicts with assumptions made on the direction of flow. The Dirichlet setup in the temperature boundary condition is, therefore, inappropriate as the boundary can vary between an inlet and an outlet across the height depending on the velocity field in the film region.

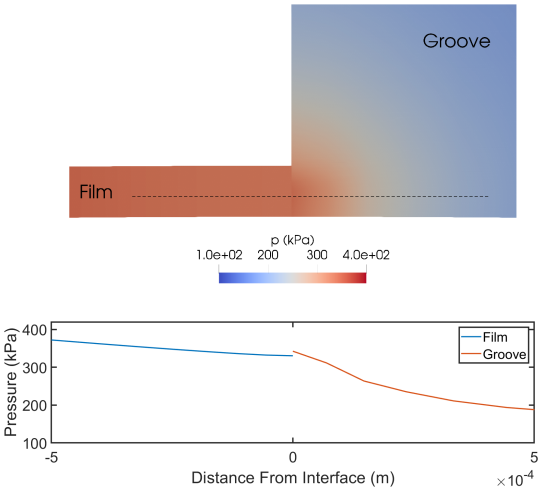

(a) Pressure (Film Inlet)

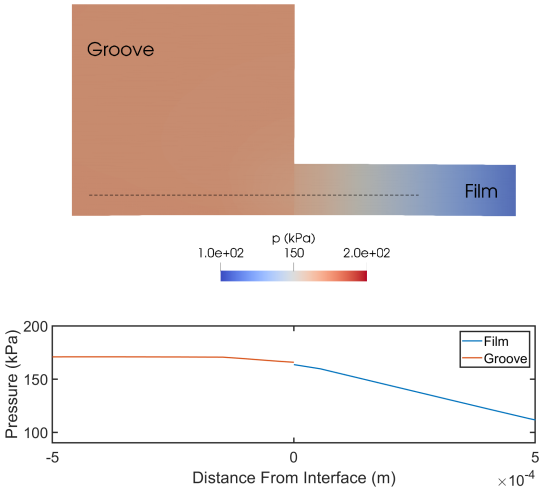

(b) Pressure (Film Outlet)

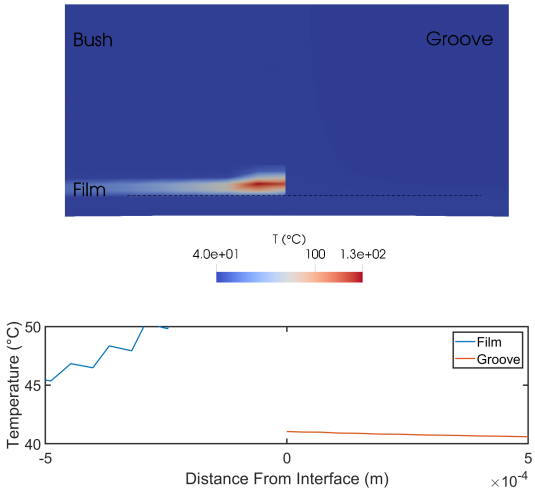

(c) Temperature (Film Inlet)

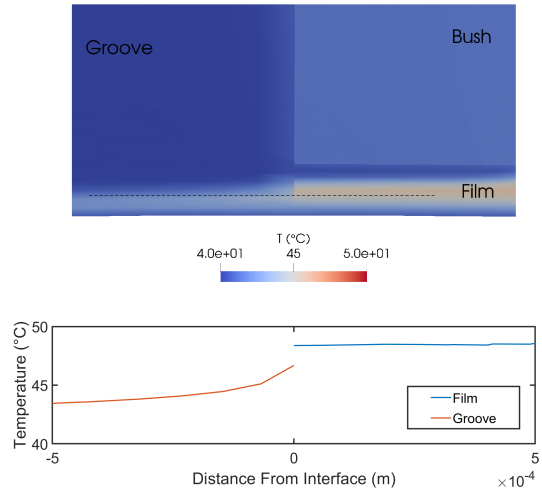

(d) Temperature (Film Outlet)

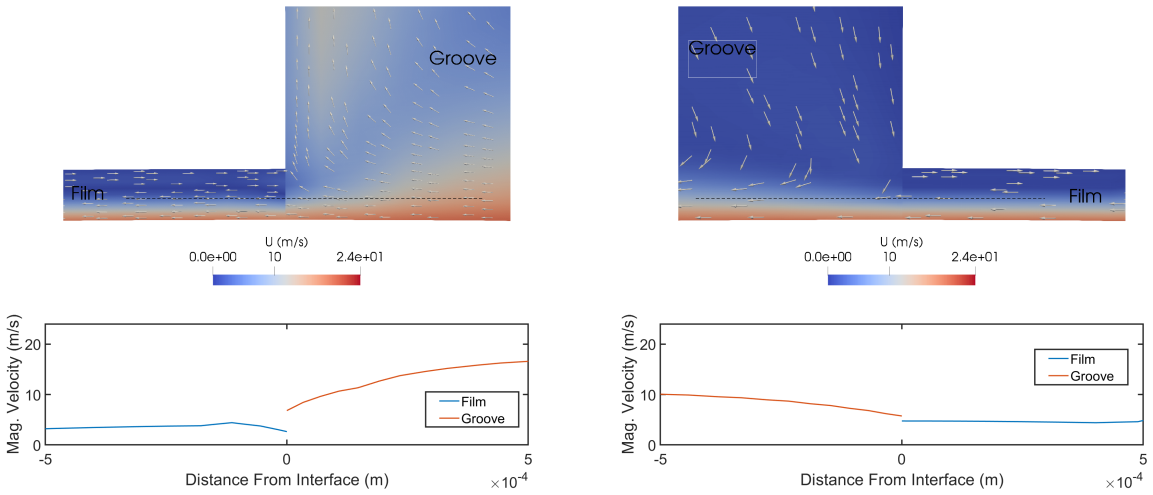

(e) Velocity (Film Inlet)

(f) Velocity (Film Outlet)

Figure 4.7: 2D Journal Bearing at rotational speed 4000rpm and eccentricity 0.6, solutions near the film inlet (a,c,e) and film outlet (b,d,f) using the initial setup for TEHL-CFD interfacing

4.3.2.2 Interfaced Temperature Boundary

To correct the numerical inconsistency causing the high temperature error in the film, a variable setup for the boundary condition is proposed which varies between a Dirichlet and Neuman condition depending the mass flux at each face on the boundary. In the case where the flow at boundary face is into the film domain, a Dirichlet condition is applied in the TEHL model where the value is taken from the temperature solution on the boundary in the CFD solution. When the flow direction is out of the film, a Neuman boundary condition is used with a gradient of 0. This conditions is also applied in the groove region on the film inlet boundary.

Figure 4.8 shows the updated results of pressure, temperature and velocity using the variable direction temperature boundary condition. The temperature solution in Figure 4.8c is now more continuous between the TEHL and CFD solutions and the film inlet is without a higher temperature region. At the film outlet there is some discontinuity in the profile which follows the cross flow tangential to the interface in the groove region. This is shown in the velocity profile at the film outlet in Figure 4.8f where the vectors are directed downwards at the interfaces as the oil is drawn down by the rotation of the shaft.

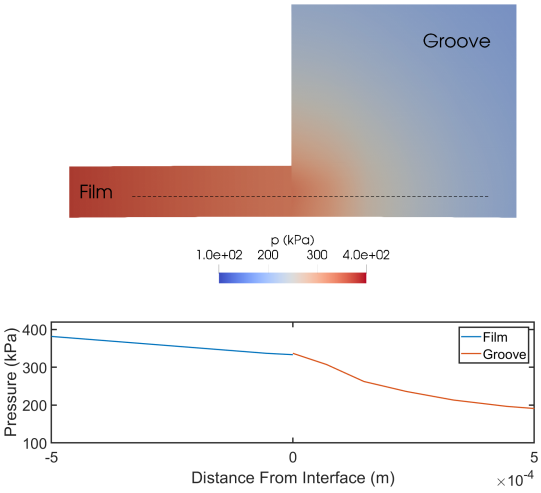

(a) Pressure (Film Inlet)

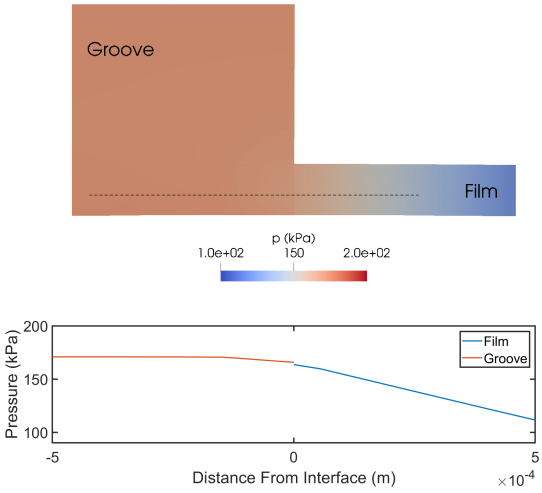

(b) Pressure (Film Outlet)

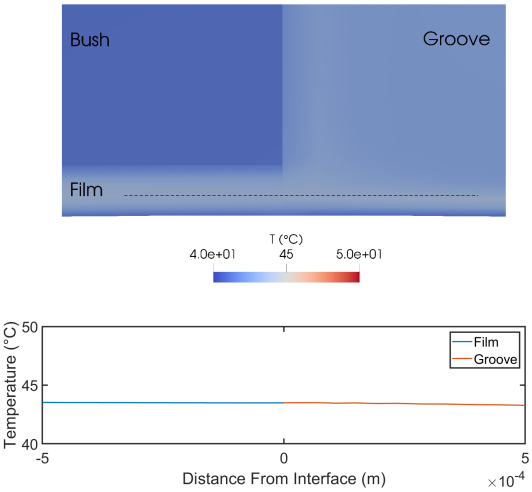

(c) Temperature (Film Inlet)

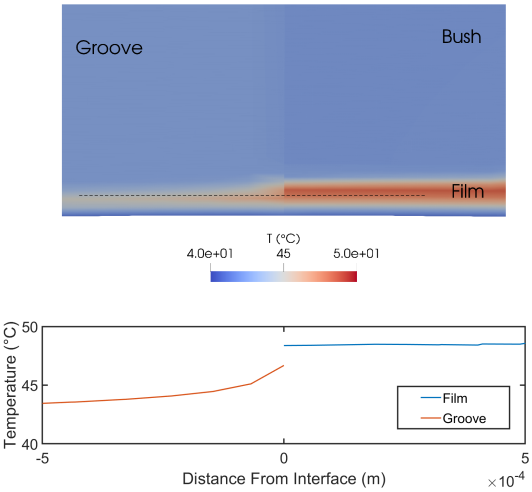

(d) Temperature (Film Outlet)

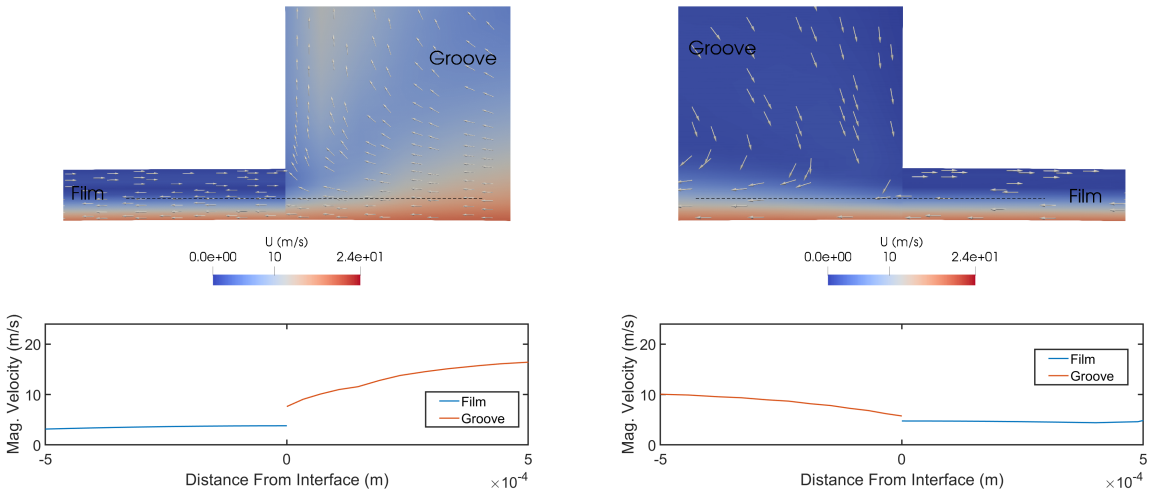

(e) Velocity (Film Inlet)

(f) Velocity (Film Outlet)

Figure 4.8: 2D Journal Bearing at rotational speed 4000rpm and eccentricity 0.6, solutions near the film inlet (a,c,e) and film outlet (b,d,f) using the corrected temperature boundary condition

4.3.2.3 Interfaced Velocity Boundary

A challenge with the integration of the CFD model with the current implementation of the TEHL methodology is the inconsistency between the mesh geometry and the true geometry in the solution. This issue arises due to the film thickness in the TEHL model being treated as a field variable rather than a geometric property incorporated into the mesh. This setup provides the freedom for the TEHL model to vary the film height profile when varying the eccentricity of the shaft and the angular position during the solution procedure without making changes to the mesh. This is particularly influential in cases converging to a specified load where the eccentricity is an unknown variable at the start of the simulation. The mesh of the TEHL region, therefore, has a uniform thickness which does not reflect the true film height in the solution. When interfacing with CFD, the geometry at the coupled boundaries is fixed to match the thickness prescribed in the TEHL mesh. As the shaft position varies in the TEHL solution, the area of these interfaces does not reflect the true area, as is presented in Figure 4.9, which is greater than that in the mesh geometry. Furthermore, as the shafts angular position varies, there is a difference in the film height between the film inlet and outlet boundaries.

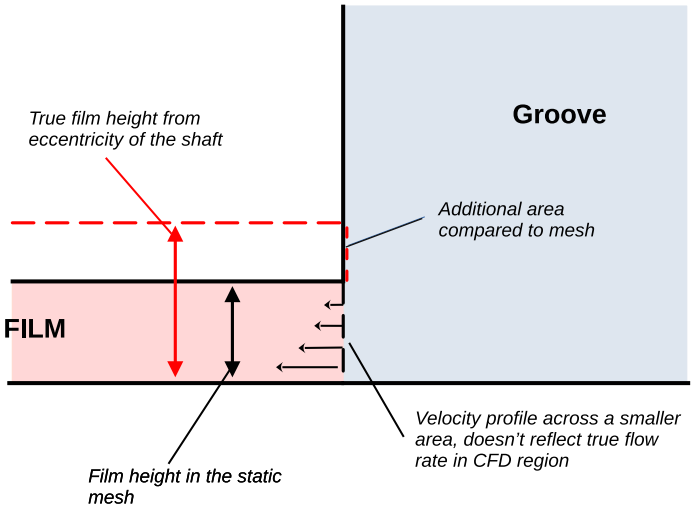

Figure 4.9: Inconsistency of the interface boundary areas between the TEHL and CFD methodologies

The inconsistency between the mesh boundary area and the true interfaces area causes a difference in mass flow between the TEHL and the CFD regions. This difference in compared in Figure 4.10 which shows the mass flow rates on the film inlet and outlet boundaries in the TEHL model and CFD model. The inconsistency in mass flow would particularly affect the temperature solution as heat input from the film region to the groove is incorrect.

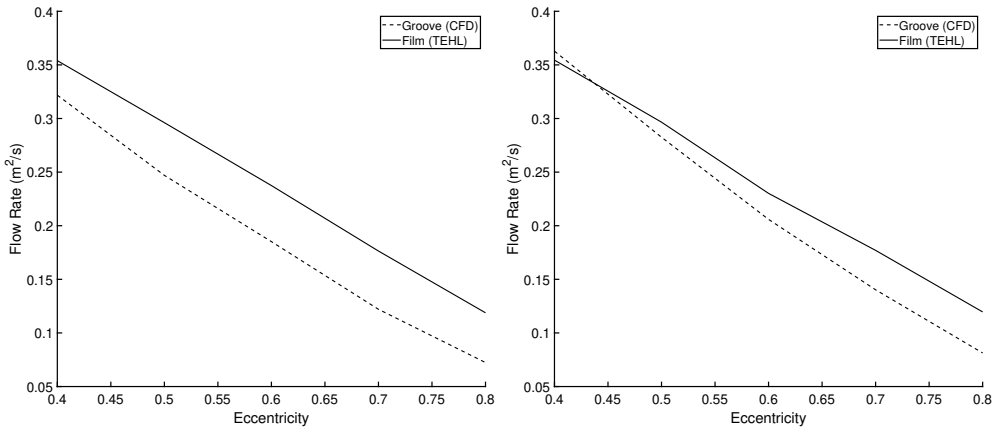

(a) Film Inlet (b) Film Outlet

Figure 4.10: Comparison of 2D flow rates at the film inlet and outlet boundaries between the film (TEHL) and groove (CFD) regions

To reduce the inconsistency of the mass flow between the TEHL and CFD regions, a scaling

factor is proposed here to be applied during the transfer of the velocity field on the interface from the TEHL region to the CFD region. The scaling factor used is the ratio of film height to the mesh clearance, thereby correcting for the inconsistency in the CFD mesh at the film interfaces:

$$U_{cfd} = \frac{h}{C} U_{TEHL} \tag{4.16}$$

where U_{cfd} is the normal velocity on the interfacing boundary face in the CFD region, U_{TEHL} is the velocity on the interfacing boundary face in the TEHL region, h is the film height at the boundary interface and C is the height of the mesh geometry of the film. The velocity profile along the interfaces in the solution of the CFD region will, therefore, not reflect the true velocity profile and the height of the interfaces will also not be reflect the true film height in the solution. However, given the geometry of the film is significantly smaller than the geometry of the groove, the variation in momentum due to the inconsistent area and velocity profiles is less significant to the solution compared to the mass flow rate between the regions, which also affects the heat flow into the CFD from the TEHL region. A comparison of the flow rates on the film inlet and outlet interfaces using scaled velocity setup in Equation 4.16 is presented in Figure 4.11, showing a significantly closer agreement in the flowrates between the regions.

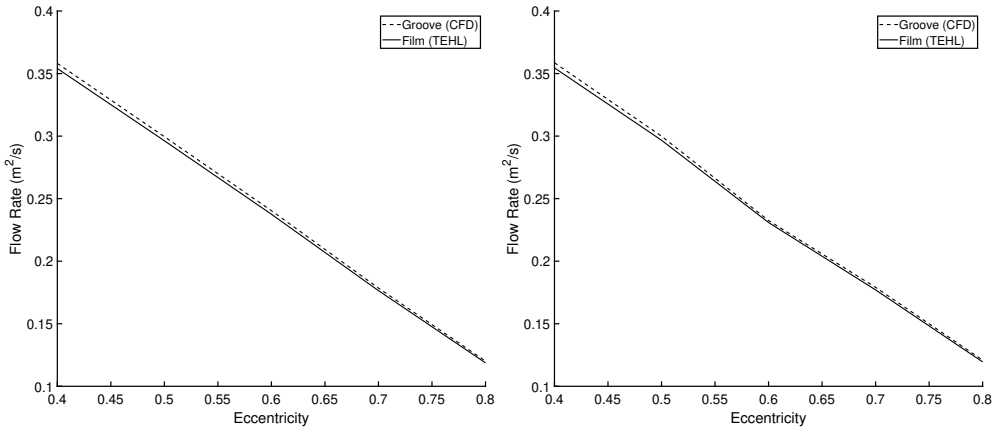

(a) Film Inlet (b) Film Outlet

Figure 4.11: Comparison of flow rates at the film inlet and outlet boundaries between the film (TEHL) and groove (CFD) regions applying the scaled velocity condition in Equation 4.16

A notable error in the proposed methodology is the potential for a large discrepancy in velocity magnitude between the shaft surface and the profile on the interfacing boundary. Figure 4.12 shows the difference in the velocity profile on the interface approaching the shaft wall. This causes the velocity field to contain an apparent acceleration at the interface into the film region which tends to reduce the pressure value adjacent to the interface, therefore affecting the pressure coupling with the TEHL model. This error was found to be significant in the three-dimensional journal bearing cases in Chapter 5, causing divergence of the solution at higher load causes where the eccentricity tends to increase.

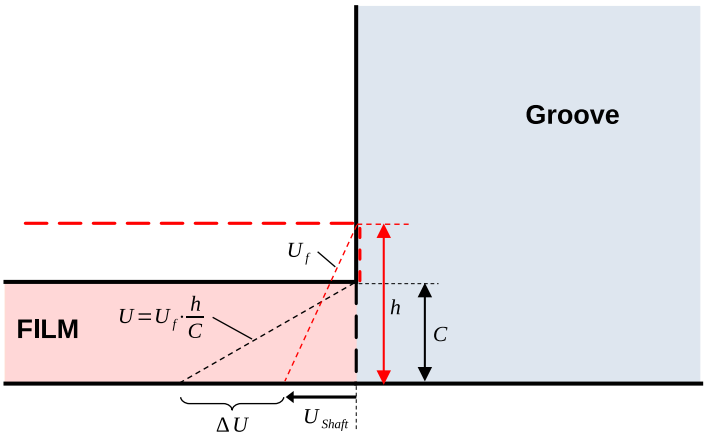

Figure 4.12: Velocity scaled boundary condition.

A proposed solution is to increase the clearance in the film mesh to limit the scaled velocity to the shaft velocity. The mesh clearance value is suggested to be double the clearance, which would be the maximum film height of the interface if the shaft eccentricity were 1. Figure 4.13 shows the velocity scaling boundary with the increase mesh clearance, where the velocity does not exceed the velocity of the shaft wall.

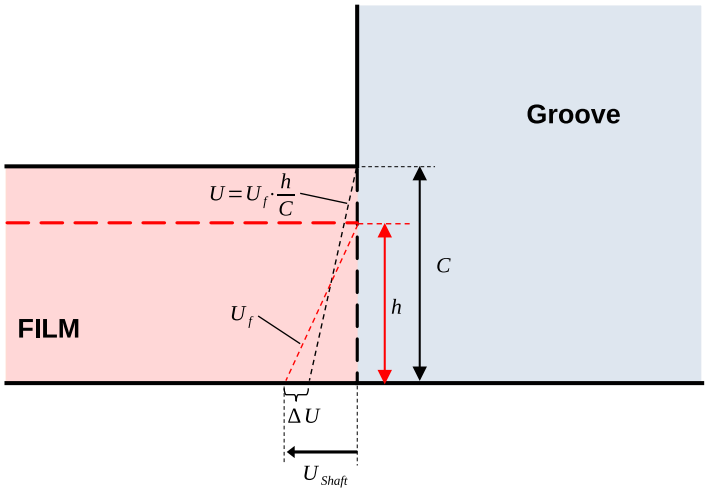

Figure 4.13: Velocity scaled boundary condition with increased mesh clearance.

Figure 4.14 shows the field solutions for the case with operating conditions in Table 4.4 around the film inlet and outlet interfaces with the scaled velocity boundary condition. Continuity across the pressure field in Figures 4.14a and 4.14b is maintained, and the temperature field follows a similar profile to the results in Figure 4.16. The result of the velocity scaling interface setup can be seen in the profiles in Figures 4.14e and 4.14f, where the velocity magnitudes in the groove region are greater than the values field in the film region.

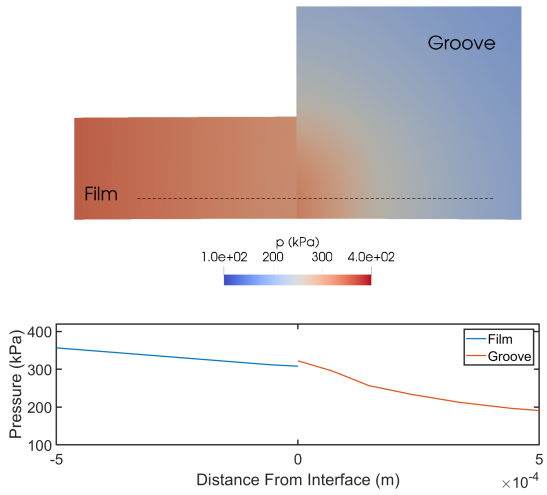
Groove
Film
p (kPa)
1.0e+02 200 300 4.0e+02
Pressure (kPa)
400
300
200
100
Film
Groove
-5
0
5
Distance From Interface (m)
×10-4

(a)

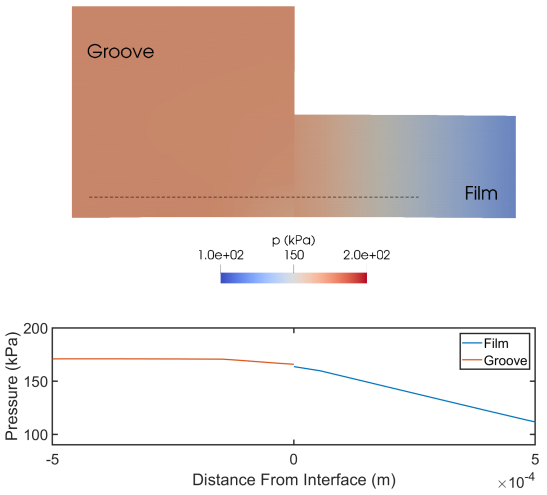
Groove
Film
p (kPa)
1.0e+02 150 2.0e+02
Pressure (kPa)
200
150
100
Film
Groove
-5
0
5
Distance From Interface (m)
×10-4

(b)

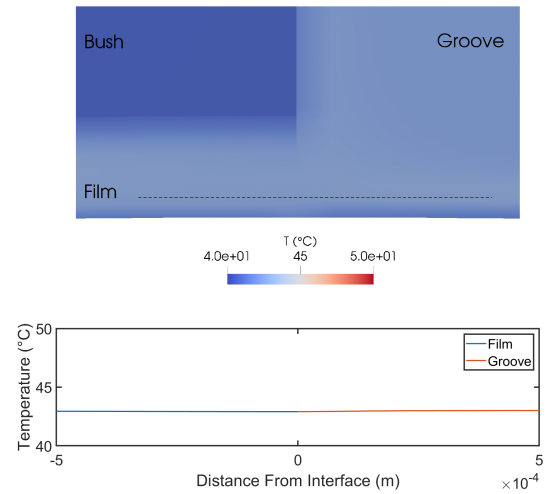
Bush
Groove
Film
T (°C)
4.0e+01 45 5.0e+01
Temperature (°C)
50
45
40
Film
Groove
-5
0
5
Distance From Interface (m)
×10-4

(c)

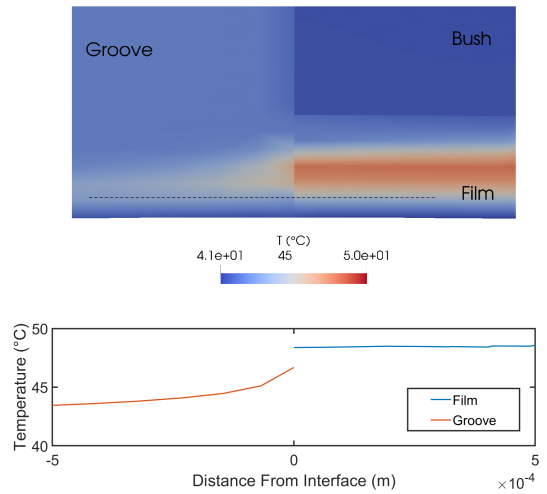
Groove
Bush
Film
T (°C)
4.1e+01 45 5.0e+01
Temperature (°C)
50
45
40
Film
Groove
-5
0
5
Distance From Interface (m)
×10-4

(d)

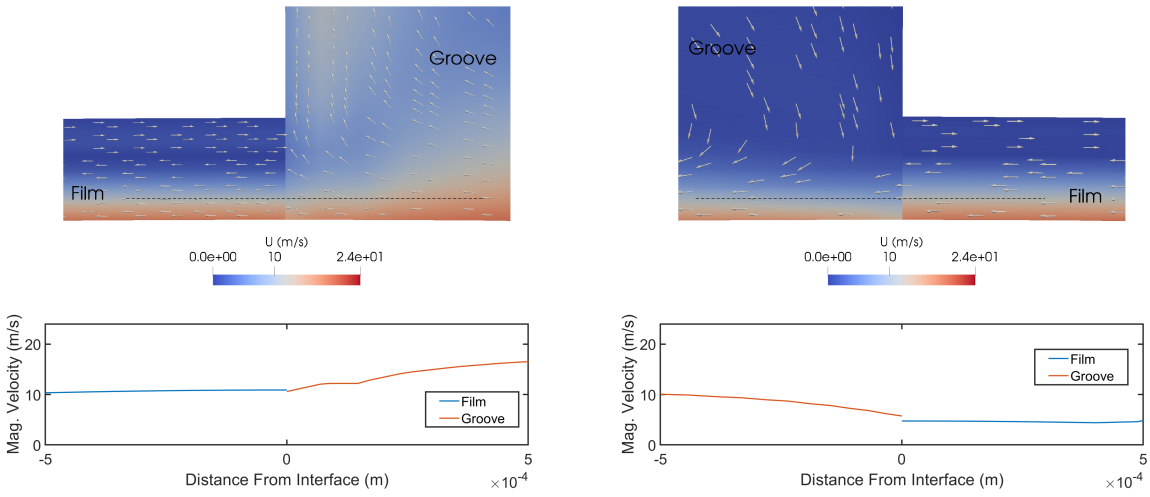

(e) (f)

Figure 4.14: Field interfacing between CFD, TEHL and solid regions at the film inlet (a,c,e) and film outlet (b,d,f) using the scaled velocity boundary condition

The solution to pressure, temperature and velocity in the wider groove (CFD) region is presented in Figure 4.15 from the the same case for the interfaces in Figure 4.14. Pressure in Figure 4.15a and temperature in Figure 4.15b show the solution are mostly uniform in the groove. The pressure mainly varies at the film inlet and outlet faces while the bulk domain is close to the supply pressure of $1.7x10^5 Pa$. The temperature is mostly uniform except near the shaft wall where a clear boundary layer can be seen connecting the film outlet to the film inlet boundaries. This behaviour is understood looking at the velocity solution which further highlights the boundary condition on the shaft wall. The heat from the oil exiting the film region is shown to carry within the shaft wall boundary layer with very minimal observable mixing with the supply oil.

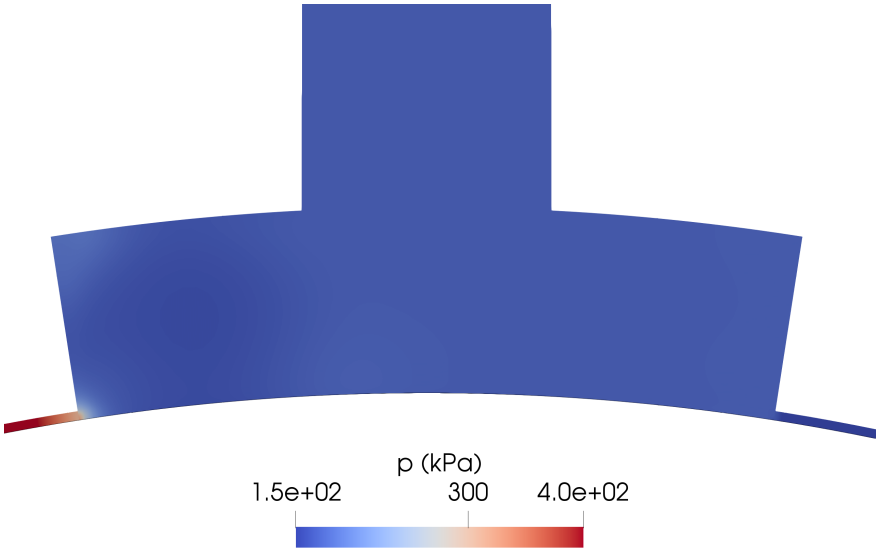

(a) Pressure

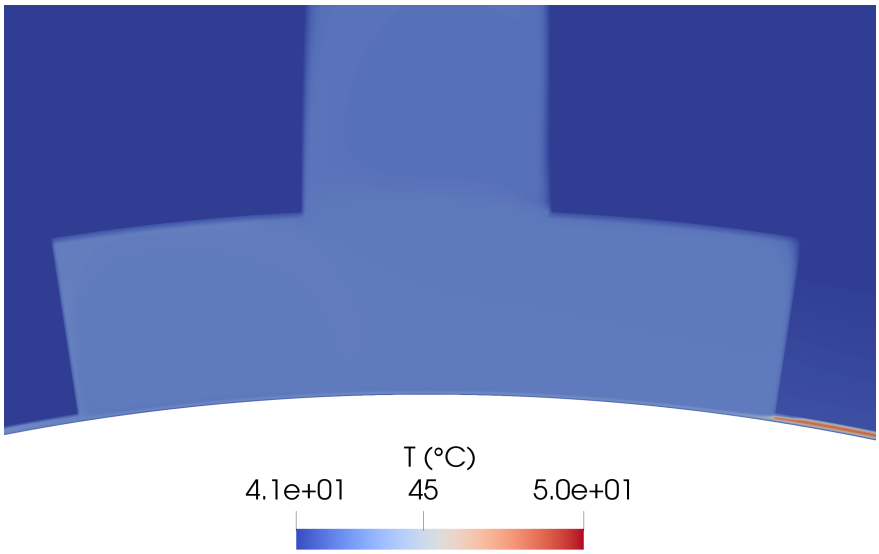

(b) Temperature

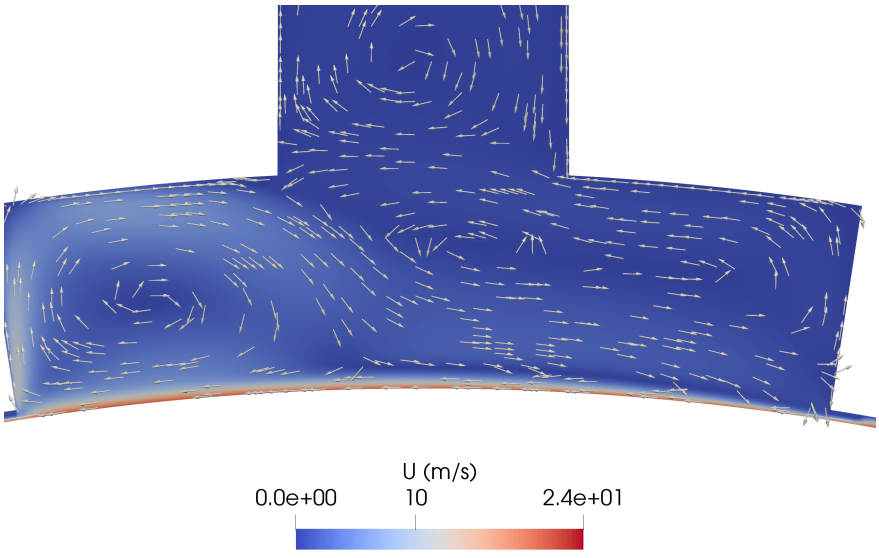

(c) Velocity

Figure 4.15: Groove variable field solutions.

The laminar setup in the CFD model in this case is likely the cause for the heat in the recirculating flow being contained within the boundary layer which can be seen in Figure 4.15c. This behaviour highlights the potential influence the inclusion of a turbulence model would have on the solution, in particular the prediction of the inlet temperature to the film region. The additional mixing behaviour introduced by turbulent flow in the CFD model would increase the mixing between the supply and recirculating oil and reduce the inlet temperature prediction. The following section presents the influence from the introduction of the turbulence models described in Section 4.1.

4.3.2.4 Turbulence Effects

Kosasih & Tieu (2004) investigated the thermal mixing in the groove of a journal bearing and compared the results of laminar and turbulent cases with images of the flow in an experimental rig. The flow field in the turbulent cases qualitatively agreed with images of the physical flow, identifying similarities in the rotational nature of the flow which were not present in the laminar case. These results suggest that turbulence effects will have an impact on the CFD solution in the case of a journal bearing groove and is therefore included in this methodology.

Figure 4.16 shows the variable fields in the groove region for the case study including the $k-\varepsilon$ turbulence model. Similarly to the laminar case, the bulk of the pressure and temperature solutions is uniform except approaching either of the interface boundaries. The pressure solution has the same features as the laminar case where there is a higher pressure at the film inlet compared to the supply and a lower pressure at the film outlet. A small change in the values at the interfaces is seen from the inclusion of the turbulence model; at the film inlet the pressure increased from 217kPa in the laminar case to 219kPa in the turbulent case, and at the film outlet the pressure decreased from 165kPa in the laminar case to 153kPa in the turbulent case. The temperature profile in Figure 4.16b shows a similar trend where most of the heat in the outlet remains in the boundary layer of the shaft. A greater dissipation of the heat is visible in the turbulent case where the temperature decrease is greater across the boundary layer of the shaft. This is also is demonstrated in the change in inlet temperature between the cases; $42.2°C$ in the laminar case and $41.6°C$ in the turbulent case. The greater heat dissipation follows the trend seen in the turbulent kinetic energy and dissipation rate in Figures 4.16d and

4.16e respectively. The turbulent kinetic energy solution shows the most turbulent region is close to the shaft boundary which is also seen in the dissipation rate where much of the heat is transported in the groove region. The greater mixing behaviour from the turbulence model in this region of higher heat transport is likely the primary cause for the change in the temperature at the film inlet interface.

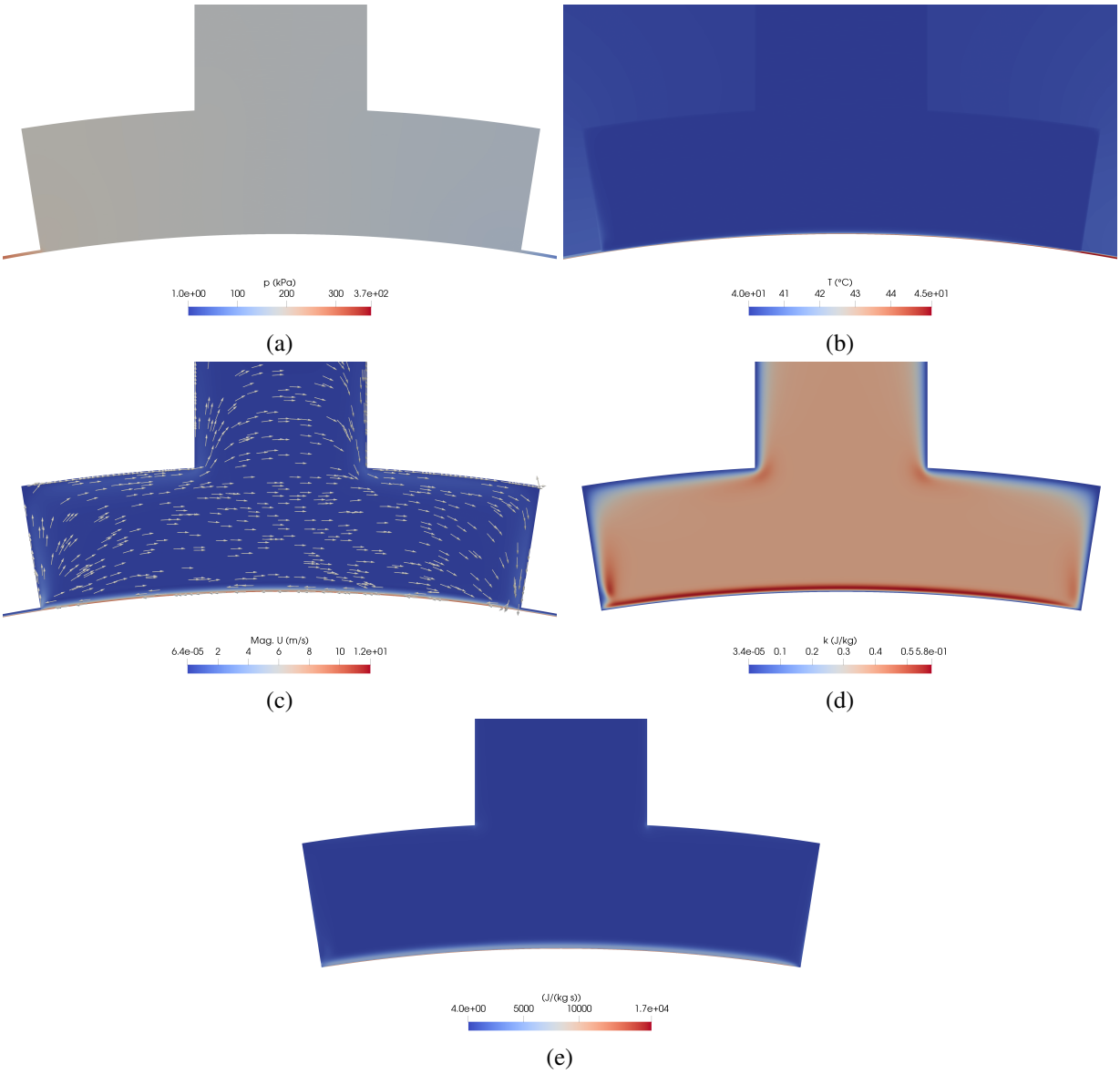

Figure 4.16: 2D Groove solution at 2000rpm and eccentricity 0.6 with $k-\varepsilon$ model: a) Pressure, b) Temperature, c) Velocity, d) Turbulent kinetic energy, e) Turbulent dissipation rate

A parametric study is presented here to investigate the of the turbulence models on the solution in the two-dimensional journal bearing. The $k-\varepsilon$ and $k-\omega$ models are included to observe any difference between the results. The $k-\varepsilon$ is noted to be optimal for bulk fluid flows, which

may be more optimal for consider the mixing in the groove, and the $k-\omega$ is more optimal close to wall boundaries, which could be more appropriate given the interfaces to the film region are close to the shaft wall.

The parameter ranges in the case study are an eccentricity range of 0.4-0.8 with increments 0.1 and rotational speed range of 2000-4000rpm with increments 1000rpm. Figure 4.17 shows the results of the parametric study on the interface with the inlet of the film, with the temperature compared in Figure 4.17a and pressure compared in Figure 4.17b.

The temperature on the film inlet interface shows some variation with the inclusion of the $k-\varepsilon$ turbulence model. In comparison to the laminar cases, the temperature is reduced when the model is considered beneath 0.7 eccentricity, and tends to increase above 0.7 eccentricity. The magnitudes of difference are relatively small, with the greatest being approximately $0.5°C$ at the highest rotational speed. The effect on the pressure at the film inlet is negligible in all cases from the results in Figure 4.17b. The $k-\omega$ model shows no variation in comparison to the laminar case, which could suggest the turbulent effects near the wall are not as significant compared to the bulk flow effects which are better represented in the $k-\varepsilon$ model.

A comparison of the results of the maximum field values in the film region is presented in Figure 4.18. The small variations in temperature at the film inlet from including the $k-\varepsilon$ model are shown to be insignificant to the solution in the film region, as shown with the similarity of results in the maximum film temperature, Figure 4.18a, and maximum film pressure, Figure 4.18b.

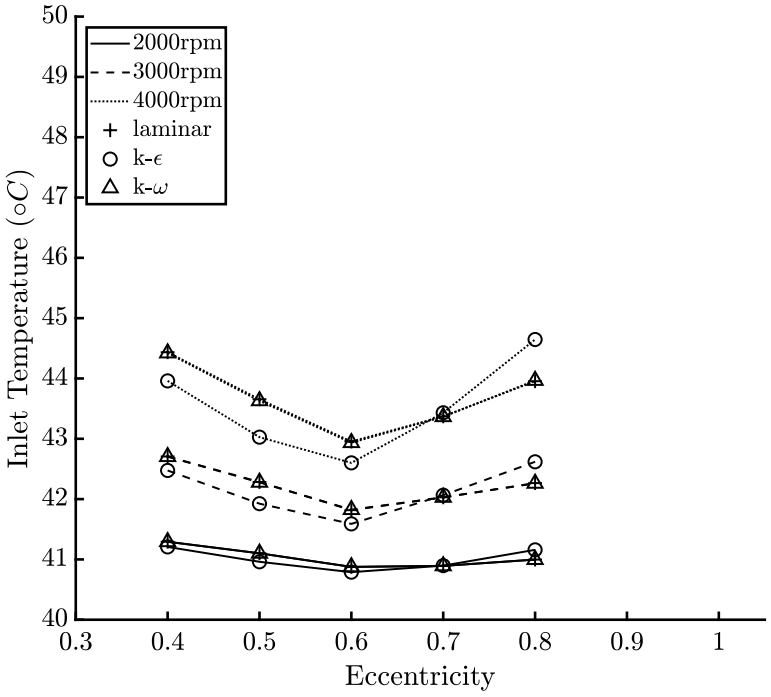

(a) Temperature

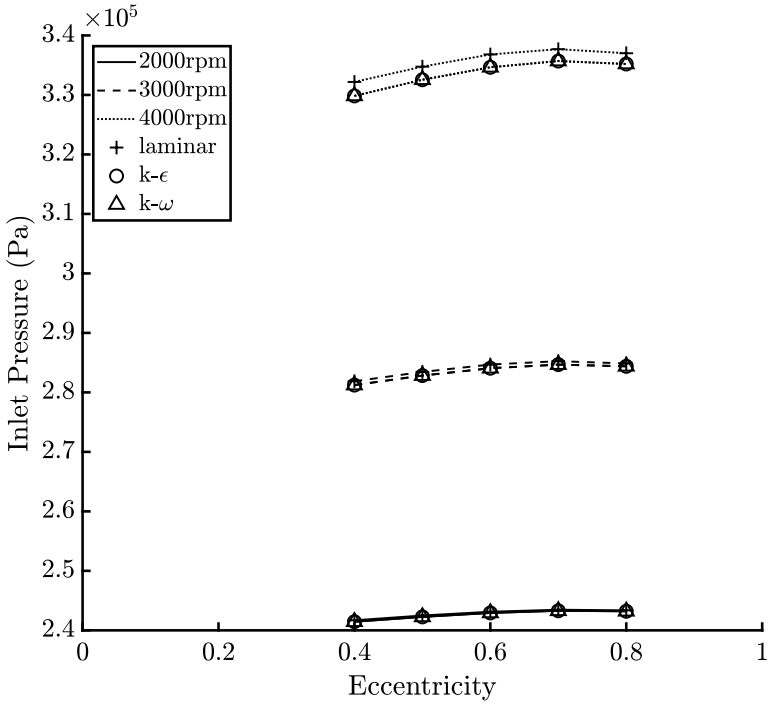

(b) Pressure

Figure 4.17: Comparison of laminar and turbulent results for the solution on the film inlet

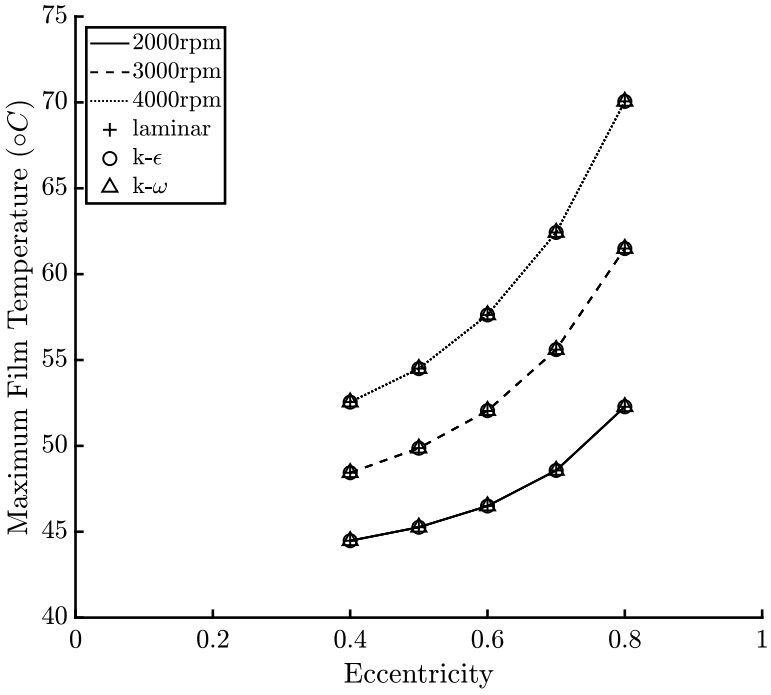

(a) Maximum Film Temperature

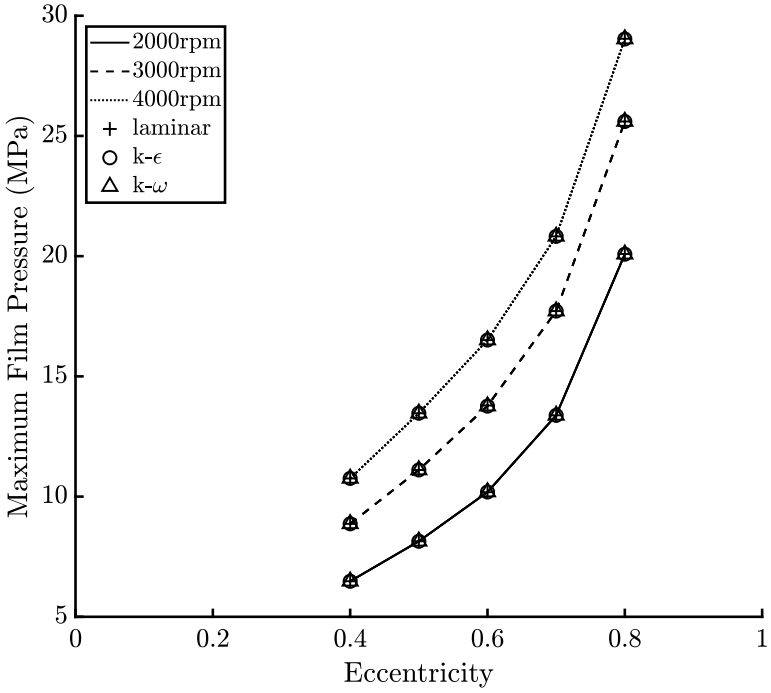

(b) Maximum Film Pressure

Figure 4.18: Comparison of laminar and turbulent results for the solution in the film region

The results in Figure 4.17 and Figure 4.18 show no significant variation between the $k-\omega$ and laminar results. In the two-dimensional case the turbulence effects in the groove region are insignificant to the solution in the film region. The influence on the temperature boundary condition at the film inlet can be observed in Figure 4.17a from including the $k-\varepsilon$ model.

These effects may be more influential in a three-dimensional case which could enhance the turbulence effects in the groove. Furthermore, different groove geometries could effect the degree of turbulent flow in the region and be more influential on the temperature solution in the film. Turbulence effects should therefore be investigated in the three-dimensional case using the $k-\varepsilon$ model.

4.3.3 Summary

The CFD methodology has been described including the energy equation, turbulence models and the VoF multiphase methodology. A two-dimensional case of a journal bearing is described to investigate the CFD coupling methodology with the TEHL model described in Chapter 3. A mesh study is performed on the groove region of the two-dimensional journal bearing case to investigate the sensitivity of the solution, focusing on the inlet temperature to the film as the parameter of interest. The initial version of the coupled boundary conditions between the CFD and TEHL regions are shown to perform poorly, attributed to assuming the flow direction at the coupled interfaces. An alternative setup allowing the flow direction to inform the temperature boundary condition significantly improves the models performance and shows good continuity in the fields across the interfaces. Further analysis of the mass continuity between the regions highlights an inconsistency due to the numerical approach in the TEHL region. A boundary condition is proposed for the velocity coupling condition which scales the velocity profile to match the flow rates between the region, therefore prioritising mass continuity between the region over the velocity profile. The interfacing boundary conditions are applied to a two-dimensional journal bearing case study to verify the numerical implementation. A turbulence modeling investigation showed that incorporating turbulence modeling into the journal bearing case study influence the inlet temperature prediction to the lubrication region. The inlet temperature varied by approximately $1^{\circ}C$ at the highest rotation speed in the investigation. This suggests turbulence modeling in the supply region will effect the prediction of thermal mixing and therefore the temperature field solution. This ill be considered in case studies in the following chapter which presents a three-dimensional case study of the journal bearing previously described in Chapter 3. The study is shown to validate the verify the solution from interfacing the CFD and TEHL models against experimental results.

Chapter 5

Coupled Methodology Results

In this Chapter the TEHL-CFD methodology is validated against experimental results using the journal bearing case study from Ferron *et al.* (1983) used to validate the numerical methodology in Chapter 3. An additional region incorporating the CFD methodology is included in the numerical model to simulate the fluid flow in the groove of the bearing. The results in the film region of the numerical model are compared to the experimental measurement to validate the coupling methodology. This method of validation is indirect, however verifies the CFD solution by comparing the results near the groove region.

A second case study is presented to show the potential of the current methodology for modeling hydrodynamic lubricated components by simulating an experimental rig developed by the Mechanical and Aerospace Systems (MAS) research group. The results verify the performance of the CFD module in a more complex context and shows the multiphase functionality. The incorporation of the multiphase model expands the potential application for the TEHL-CFD methodology to modelling cases such as the side leakage from a journal bearing, thrust bearing lubrication including the supply pockets, and the oil flow through rolling element bearings. These applications are beyond the scope of this research which aims to validate the coupling methodology between TEHL and CFD.

5.1 Validation Against Journal Bearing Cases

To validate the CFD-TEHL coupling approach described in Chapter 4, the journal bearing case study from Section 3.7 is expanded to include a groove region where a CFD model is applied to simulate the mixing between the supply and recirculating oil. The CFD model predicts the conditions at the inlet of the film, affecting the results in the lubrication region which are compared with the measurements from Ferron *et al.* (1983) to verify the CFD coupling methodology. The results are further compared to the original TEHL model results from Chapter 3 to show the effect from including the CFD methodology to resolve the supply groove flow.

5.1.1 Case Setup

Figure 5.1 shows a diagram of the case geometry with 3 defined regions: film (blue) which applies the TEHL methodology described in Section 3.1, bush (green) which is the solid region applying Equation 3.20 and groove (red) which applies the CFD methodology detailed in Section 4.1.

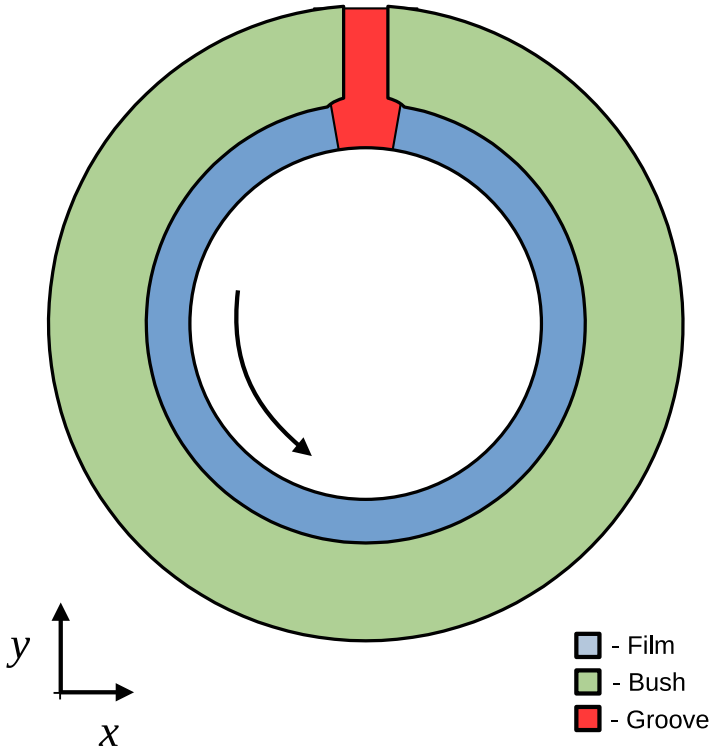

Figure 5.1: Journal Bearing Regions

Figure 5.2 shows the geometry of the groove with 3 supply holes leading to a slit at the bottom which interfaces with the film region in the journal bearing.

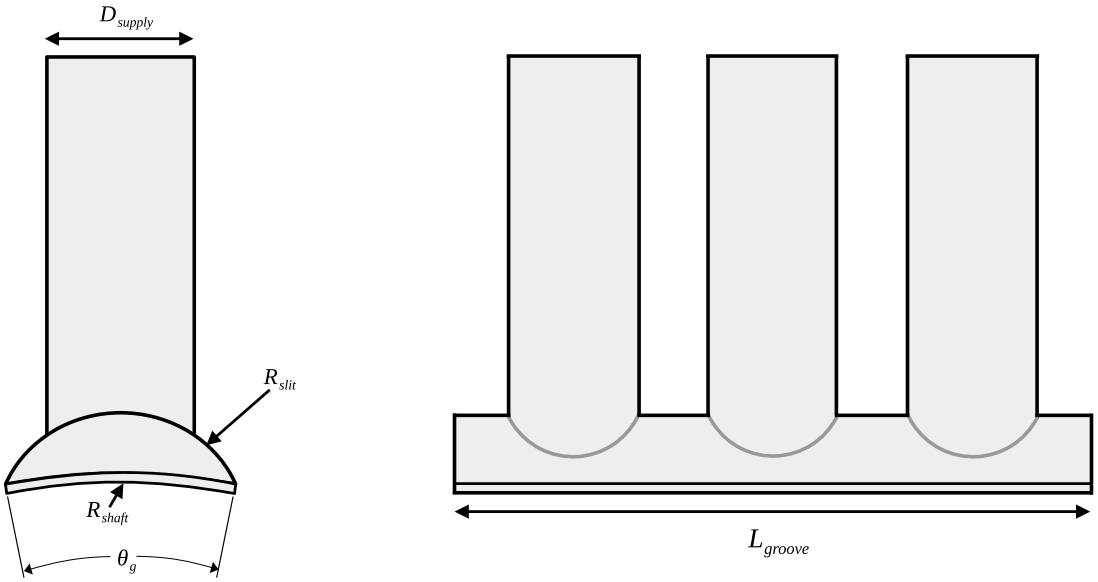

(a) Front

(b) Side

Figure 5.2: Groove Geometry

The dimensions of the groove are summarised in Table 5.1. The original study does not provide information on the groove geometry however, some information is available in subsequent experimental work using the same journal bearing rig. The number of supply holes, their diameter, the groove length and angular width is taken from Bouyer & Fillon (2002). No information on the depth of the groove is found in literature and is estimated in this work.

Symbol	Description	Value
D_{supply}	Diameter of the supply holes	14mm
L_{groove}	Length of the groove	70mm
R_{slit}	Radius of the groove slit	8.6mm
R_{shaft}	Radius of the shaft	50mm
θ_g	Angle swept by the groove	18°

Table 5.1: Groove Dimensions

5.1.2 Groove Mesh Sensitivity

The sensitivity of the solution to the groove mesh is tested using a series of cases run using the compressibleInterFoam solver from OpenFOAM (Weller Henry, 2020), which is the basis of the CFD module in the coupled solver. The VoF technique is used for the multiphase effects and includes an energy equation with compressibility modelling available for the phases. The groove is assumed to be entirely filled with the lubricant oil in this case, where the value for volume fraction is uniformly 1 across the domain. The boundary conditions for all the field are over-viewed in Table 5.2 which describes the boundary conditions type and associated value.

Boundary Name	Velocity		Pressure		Temperature		Volume-Fraction	
	Type	value	Type	value	Type	value	Type	value
Film Inlet	Neumann	0	Neumann	0	Neumann	0	Neumann	0
Film Outlet	Neumann	0	Neumann	0	Dirichlet	$60°C$	Dirichlet	1
Oil Supply	Neumann	0	Dirichlet	1.7e5Pa	Dirichlet	$40°C$	Dirichlet	1
Shaft wall	Dirichlet	$20m/s(Tangent)$	Neumann	0	Dirichlet	$41°C$	Neumann	0
Bush wall	Dirichlet	$0m/s$	Neumann	0	Neumann	0	Neumann	0

Table 5.2: Groove Mesh Sensitivity Test Boundary Conditions

The meshing approach is depicted in Figure 5.3. A structured boundary layer is used along the shaft wall to ensure a highly conformal interface with the film region, whereas an unstructured tetrahedron mesh is used in the slit to map to the more complex geometry and allow the cells to grow to a larger size compared to the size of the cells interfacing with the film region.

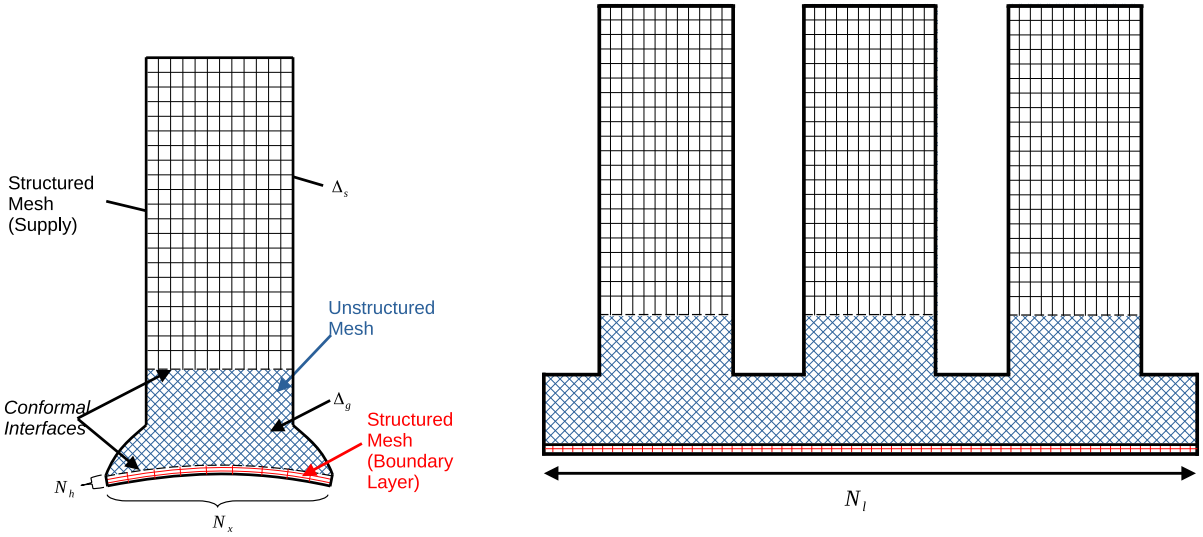

(a) (b)

Figure 5.3: Groove region mesh generation setup.

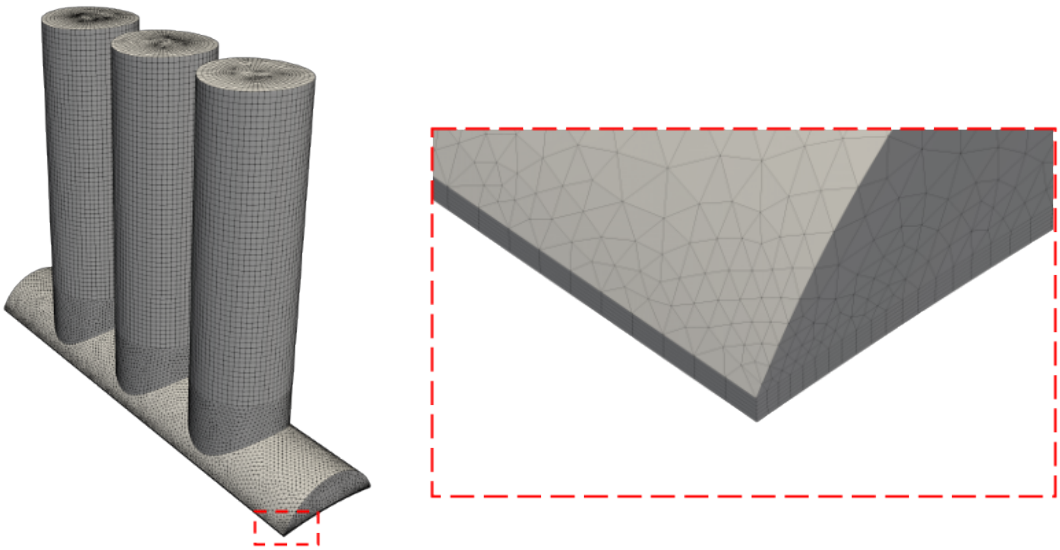

Figure 5.4: Groove region mesh

Table 5.3 presents the meshing parameters in each case of the sensitivity study in reference to

variables in Figure 5.3 and the averaged temperature across the film inlet to groove boundary, T_{inlet}. The film inlet temperature is used as the test parameter given the CFD region is primarily replacing the film temperature estimation in Equation 3.34:

$$T_{inlet} = \frac{\left(\dot{M}_{outlet} T_{outlet} + \dot{M}_{supply} T_{supply}\right)}{\dot{M}_{inlet}} \tag{5.1}$$

which is used by the TEHL model in Section 3.7. The results of the sensitivity study are shown in Figure 5.5.

Case	**No. Cells**	N_h	N_x	N_l	Δ_g	Δ_s	$T_{inlet}(^\circ C)$
1	264905	3	30	112	0.75mm	1mm	59.8
2	466759	4	45	168	0.65mm	0.9mm	59.7
3	796061	6	60	224	0.55mm	0.8mm	59.3
4	1064070	6	80	224	0.5mm	0.8mm	59.2

Table 5.3: Boundary condition setup for the oil supply to the CFD region

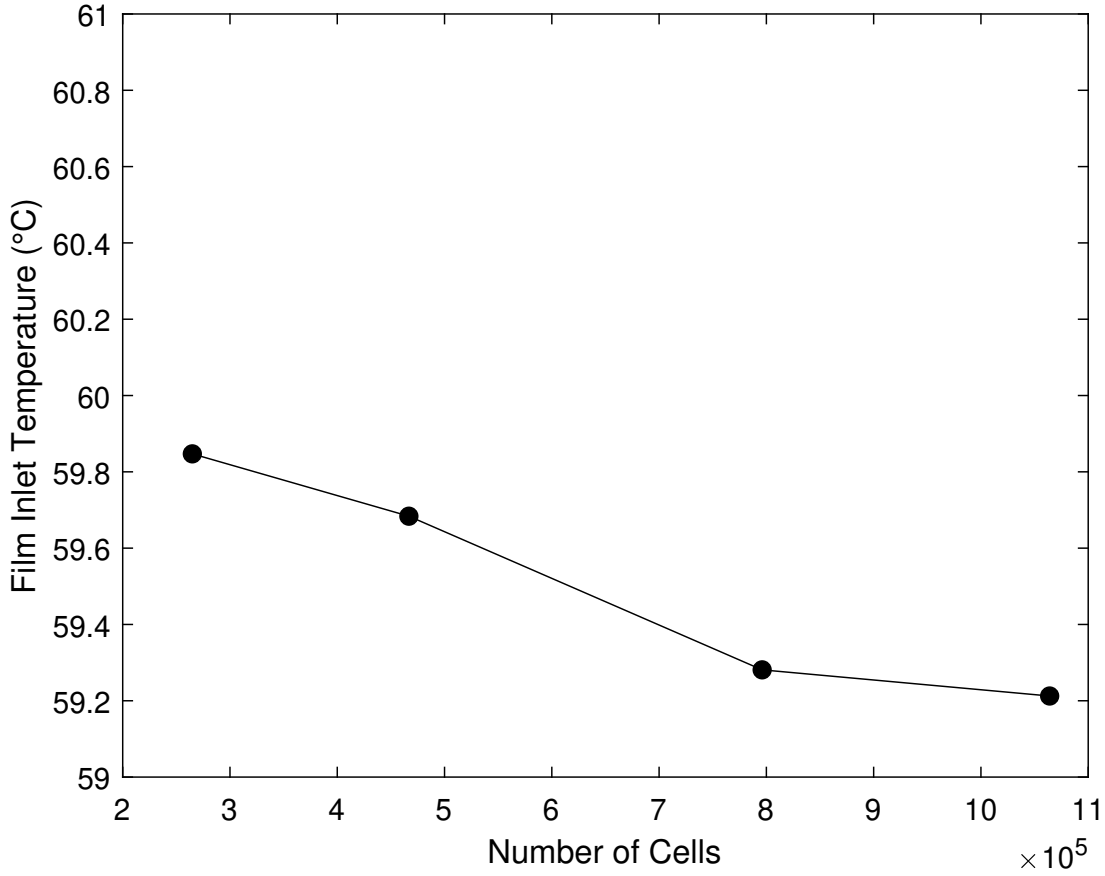

Figure 5.5: Groove Mesh Sensitivity

The results of the sensitivity study show a mesh of size of approximately 80000 is sufficient to reduce the error in the solution to $< 1\%$. The final mesh sizes in the three-dimensional journal bearing cases are summaries in Table 5.6 which shows the number of cells in each region. The bush is conformal with the film meshes and non-conformal with the groove mesh. At the film-groove interfaces the meshes are partially conformal, in the radial direction the groove mesh matches the film (3D) mesh having 6 cells, in the axial direction the groove mesh contains 224 cells, which is $x4$ the number of cells in the film region along this boundary.

Region	Mesh Size (No. Cells)
Film	19350
Film (3D)	116100
Bush	614979
Groove	1122211

Table 5.4: Mesh sizes in each region

5.1.3 Results

The parametric study parameters are repeated from the experimental study in Ferron *et al.* (1983) using a normal load range of 2-10kN in increments of 1kN and rotational speeds of 1500rpm, 2000rpm, 3000rpm and 4000rpm. The results are compared against the experimental results from Ferron *et al.* (1983) and the numerical results from Section 3.7 (TEHL). The cases are performed on an 40 cores of AMD 'Genoa' CPUs. The maximum simulation time was 34 minutes with an average simulation time across the parametric study of 24 minutes. The total time required to complete all 36 simulations was 14hrs. In comparison, the full 3D CFD simulation from Martin *et al.* (2024) of a journal bearing required 34 days on 36 cores to reach convergence, showing a significant reduction in computational load using the coupling methodology.

5.1.3.1 Validation And Comparison Of Models

Figure 5.6 compares the eccentricity of the shaft in the numerical solution with the experimental results from Ferron *et al.* (1983). Included in the comparison is the corrected experimental results from Ferron *et al.* (1983), and the results from the isolated TEHL model from Chapter

3 labelled as ”TEHL”.

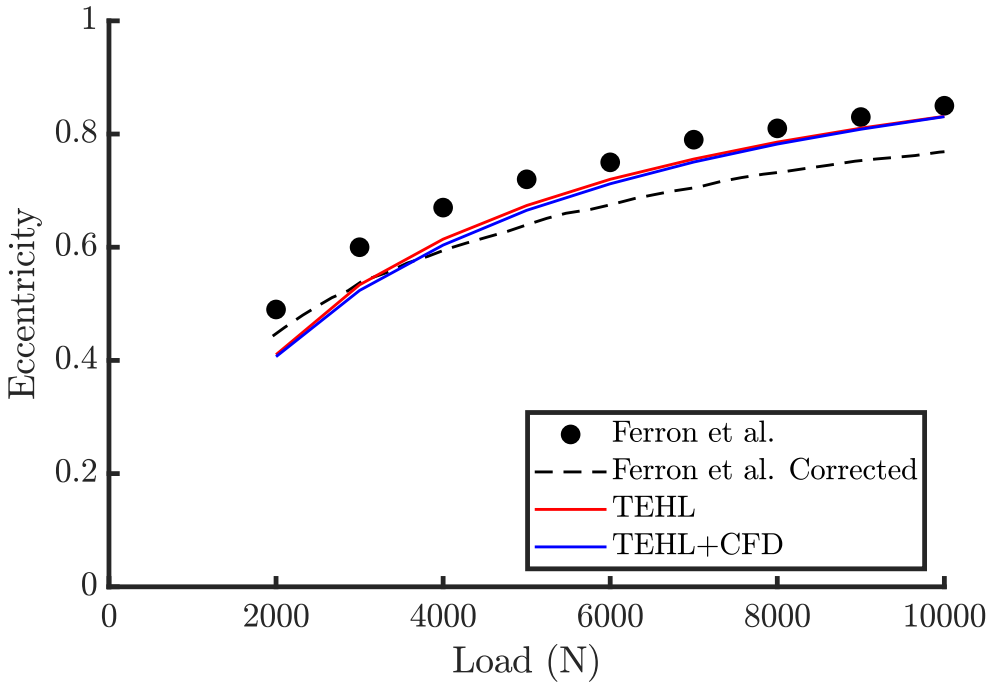

Figure 5.6: Eccentricity prediction using the CFD model in the journal bearing supply groove (TEHL+CFD) at 2000rpm

Figure 5.7 shows a comparison of the centerline pressure profiles in the film for the numerical models compared to the experimental results. The ”TEHL” data sets are the results from Chapter 3 and the ”TEHL+CFD” are the results including the CFD methodology to resolve the groove region. The pressure prediction at the inlet to the film is higher in the ”TEHL+CFD” model in each case, approximately 16kPa increase in case a, Figure 5.7a, and a 33kPa increase in case b, Figure 5.7b. Given the supply pressure is 70kPa, this is a relative pressure difference at the inlet of 22% in case a and 47% in case b, showing there is a significant increase in pressure at the film inlet caused by the geometry of the groove. However, the affect of the difference in pressure at the inlet is insignificant to the pressure profiles in the film which are similar in the TEHL and TEHL+CFD numerical setups. Case a shows no significant difference in peak pressure when the CFD methodology is included, and for case b there is a small reduction in the peak pressure, approximately 5.4% compared to the experimental results. In the current cases the difference in pressure between the ”TEHL” and ”TEHL+CFD” methodologies at the inlet is small compared to the peak value and has no significant affect on the pressure profiles.

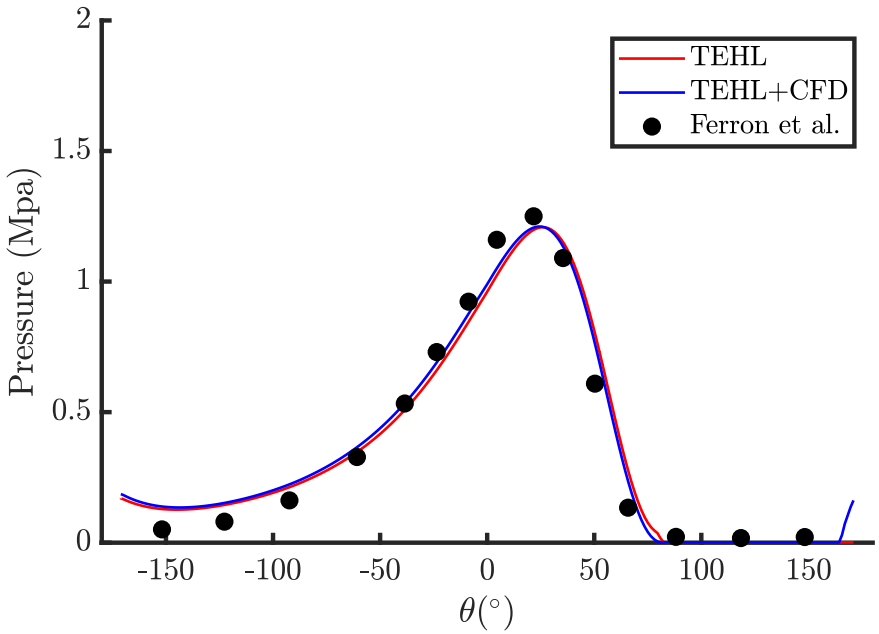

(a) a) 2000rpm and 4kN

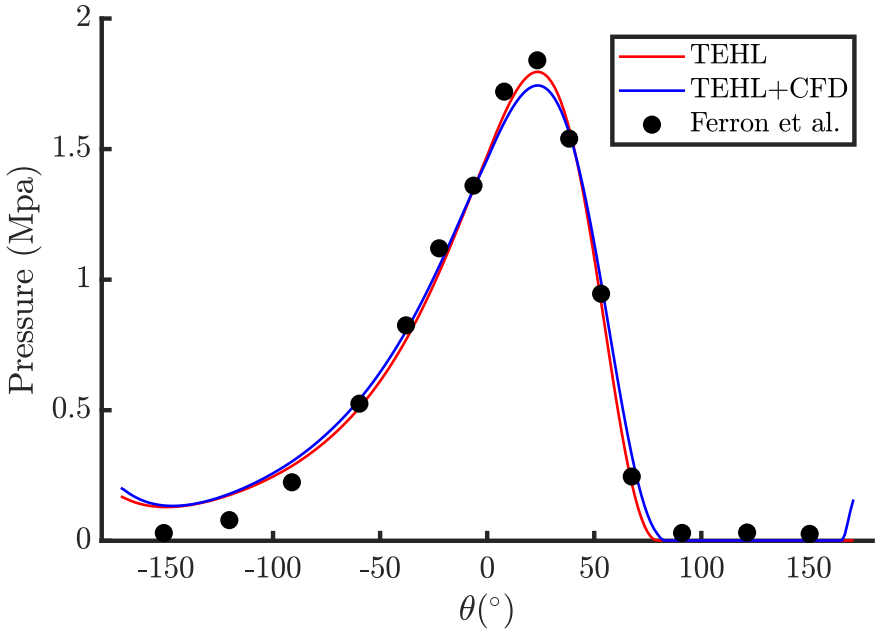

(b) b) 4000rpm and 6kN

Figure 5.7: Centreline film pressure for a journal bearing using the TEHL-CFD methodology.

The peak pressure in the film across the entire range of parameters explored is presented in Figure 5.8. The difference in peak pressure and eccentricity between the ”TEHL” and ”TEHL+CFD” models is insignificant, $< 1\%$.

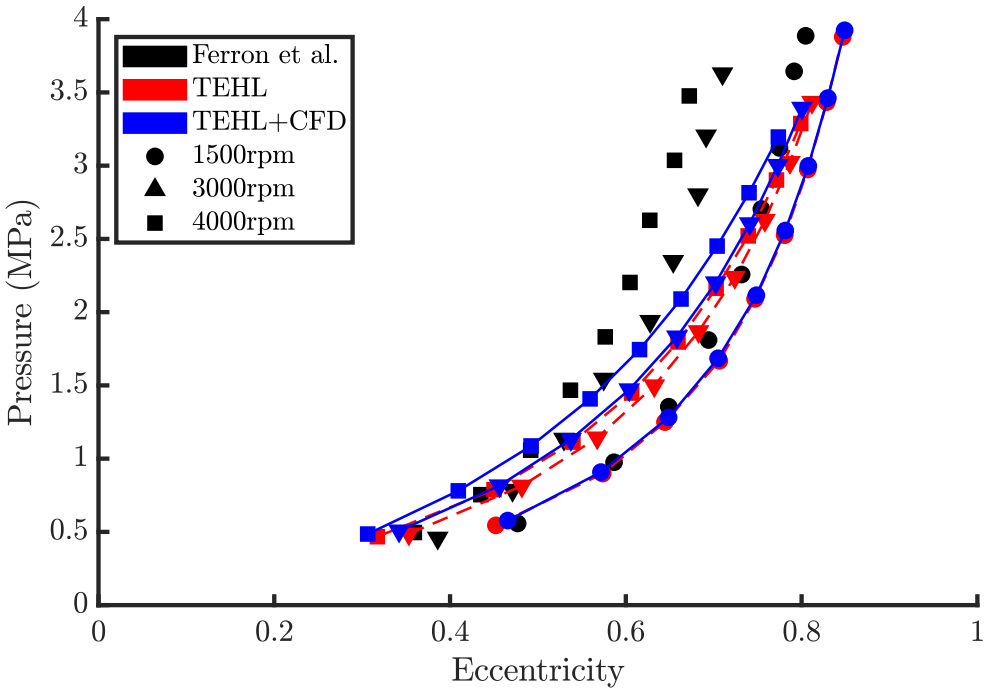

Figure 5.8: Maximum bush temperature

A comparison of the temperature centerline profiles is presented in Figure 5.9. There is a significant change in the temperature profiles when the flow in the groove is resolved with the CFD methodology where peak temperature for the "TEHL+CFD" methodology is within 0.5% for case a and 3.7% in case b. The improvement in the inlet temperature prediction is clearly observed in Figure 5.9b with an error of approximately 6.7%, compared to the "TEHL" error of 12%. This improvement in the temperature prediction highlights the benefit of incorporating the CFD methodology in the supply groove.

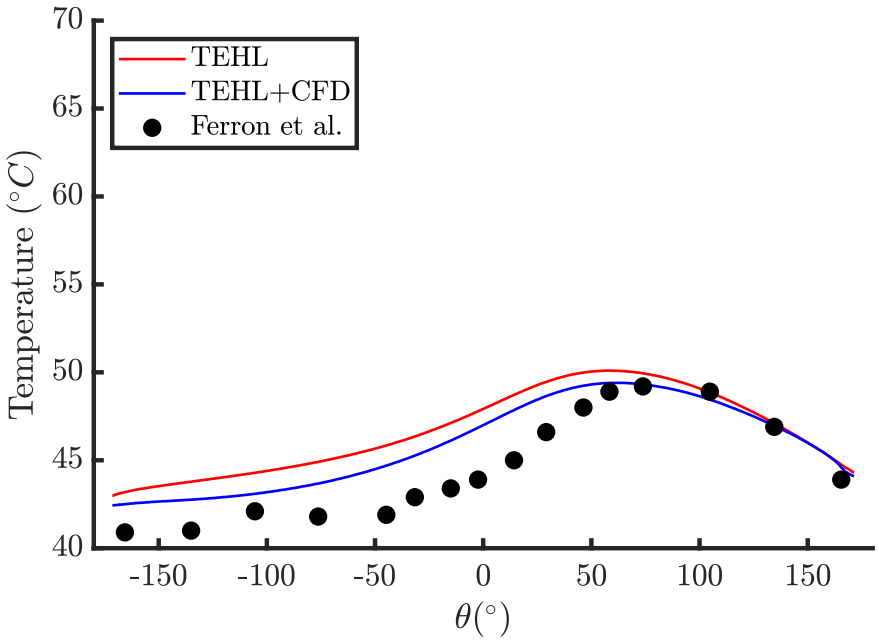

(a) a) 2000rpm and 4kN

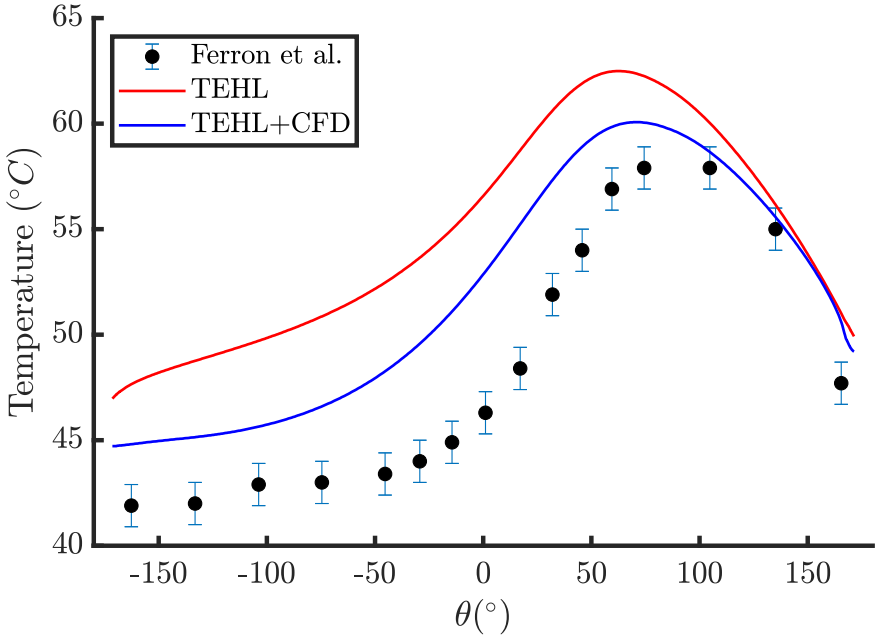

(b) b) 4000rpm and 6kN

Figure 5.9: Comparison of centerline temperature profiles along the film-bush interface

The results are further compared across the entire parameter range in Figure 5.10 for the maximum temperature on the film-bush interface. Including the CFD methodology has a more significant effect with increasing rotational speed, reduced the maximum temperature by approximately $2°C$ at 4000rpm and between $1-2°C$ at 3000rpm. This further highlights the inclusion of the CFD methodology improves the temperature prediction in the lubrication

model for cases with a greater temperature rise. The change in the solution for lower rotational speeds, ¡2000rpm in this experimental setup, is insignificant, $< 0.5°C$. In these case the approximate inlet temperature prediction using Equation 3.34 is sufficient.

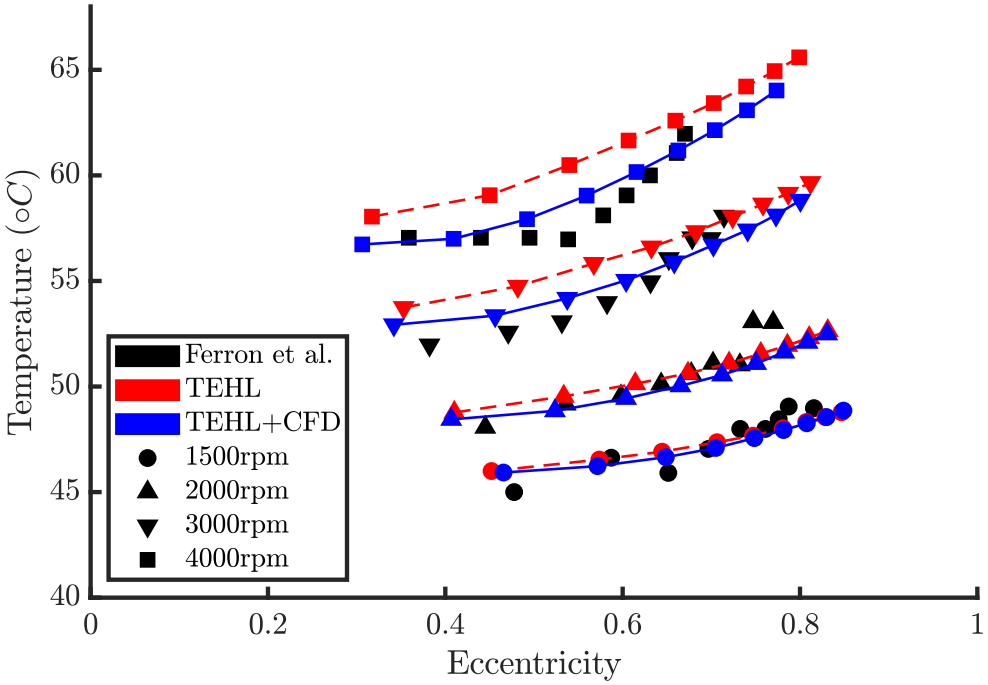

Figure 5.10: Maximum bush temperature

5.1.3.2 Groove CFD results

This section presents the results within the groove region for the three-dimensional journal bearing case at 4000rpm and 6kN. This is aimed to verify the solution in the groove qualitatively and highlight the coupling of the solution between the regions. Figure 5.11 shows the temperature along the center of the length of the bearing across all regions: film, bush and groove. The cooling effects from the groove region can be seen at TDC in Figure 5.11a of the bearing where the region is predominantly a constant temperature. Figure 5.11b shows the domain around the groove-film interfaces, where the heat from the film enters the groove. The interfacing between the regions can be seen at the interfaces where heat is carried by the film into and through the groove region within the boundary layer of the shaft. Conduction of heat can be seen in the solution across the groove-bush interfaces.

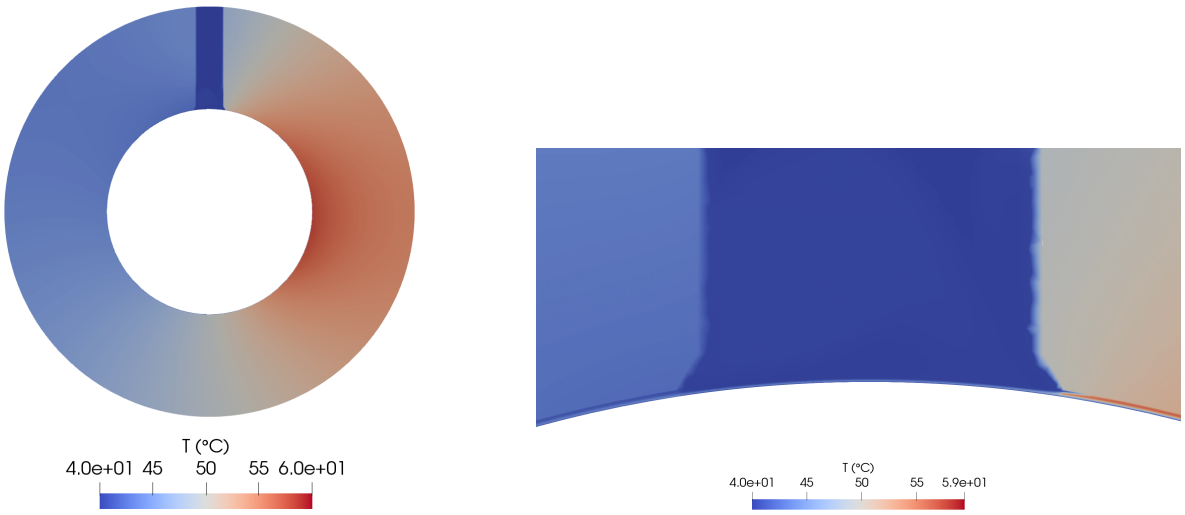

(a) (b)

Figure 5.11: Centerline temperature contour across the Film, Groove and Bush regions at 4000rpm and 6kN.

The pressure and temperature across the groove and film region is shown in Figure 5.12a and Figure 5.12b respectively. The small difference in pressure between the groove and cavitated film region can be seen in Figure 5.12a, approximately 160kPa, which causes the reverse flow of oil and reformation of the film upwind of the groove. Cooling of the oil can be observed in Figure 5.12b by the lower temperature in the groove region, reducing the oil temperature by approximately across the walls of the groove region, approximately $50°C$.

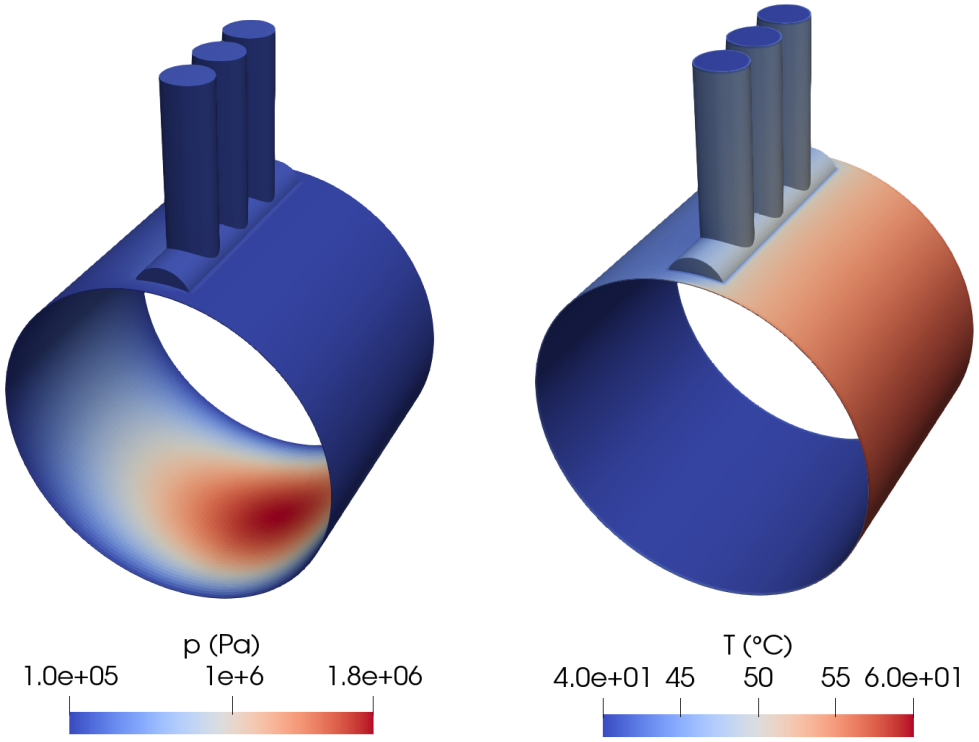

(a) Pressure (b) Temperature

Figure 5.12: Pressure and temperature between the film and groove at 4000rpm and 6kN.

Figure 5.13 shows unwrapped profiles of oil fraction, Figure 5.13a, and temperature, Figure 5.13b. These profiles are taken as a surface through the film that is half-way across the film height and unwrapped such that in Figure 5.13 the horizontal direction is the circumferential position and the vertical is the axial position along the bearing. The images are oriented around the supply groove where the boundary is indicated in black in Figure 5.13. The oil fraction in Figure 5.13a shows the reformation near the groove which is delayed along the edges of the groove because of the highly advective flow. The temperature follows a similar profile where the effects of the oil supply on the temperature are clearly seen by the reducing in the temperature as fresh oil is supplied to the film. Interestingly, the temperature profile is not uniform in the axial direction across the supply groove and streams of higher temperature oil are visible. These streams occur at approximately 0.015m, 0.022m, 0.034m, 0.043m, 0.052m and 0.065m in the axial direction. The number of streams and their distribution appear to align with the edges of the supply holes which are located axially at approximately 0.0155m, 0.03m, 0.033m, 0.047m, 0.0505m and 0.065m. The streamline patterns could, therefore, be caused by flow patterns in the supply region that are influencing the temperature distribution in the

CFD region and are being transfered into the TEHL model at the interface. The consistency of the streams across the boundary between the CFD and TEHL regions highlights the smooth solution between the numerical models. Furthermore, the non-uniform profile emphasises the potential influence that mixing properties in the supply region could have on the predictions in the lubrication region.

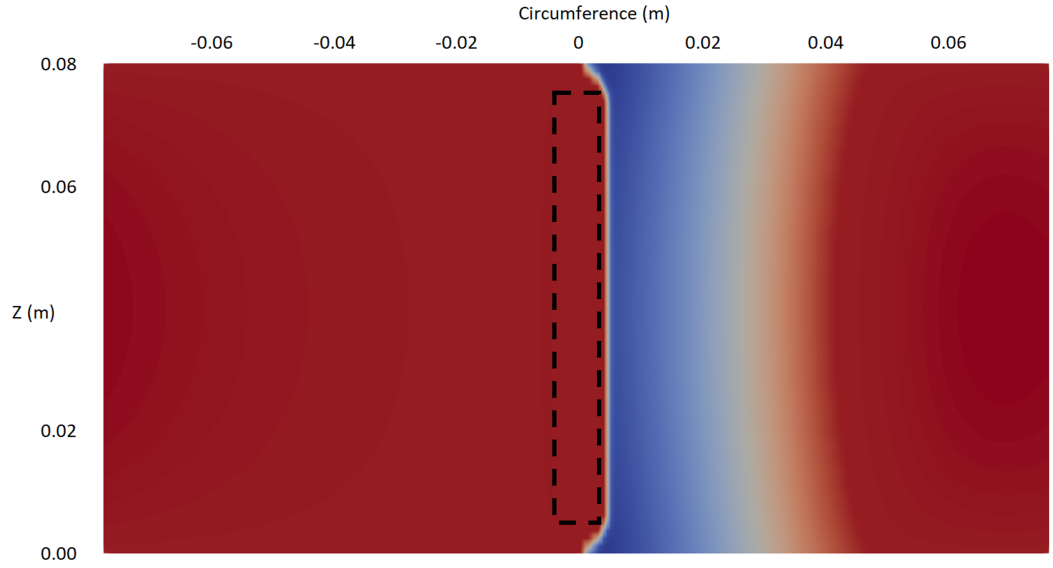

(a)

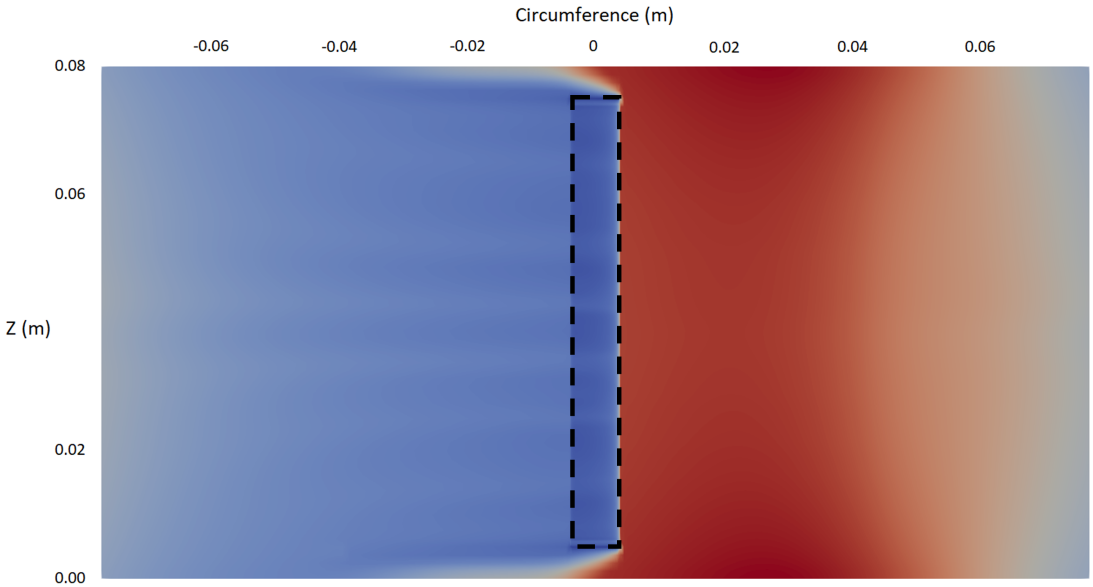

(b)

Figure 5.13: Profile along the centerline of the film height across the circumference of the bearing at 4000rpm and 6kN.

A combined image of the oil fraction in the film and streamlines of the flow in the groove is presented in Figure 5.14. The streamlines are contoured by the fluid velocity which shows the greater flow speed near the shaft wall. The rotational flow in the groove is consistent with the results of Kosasih & Tieu (2004) which observed similar vortices.

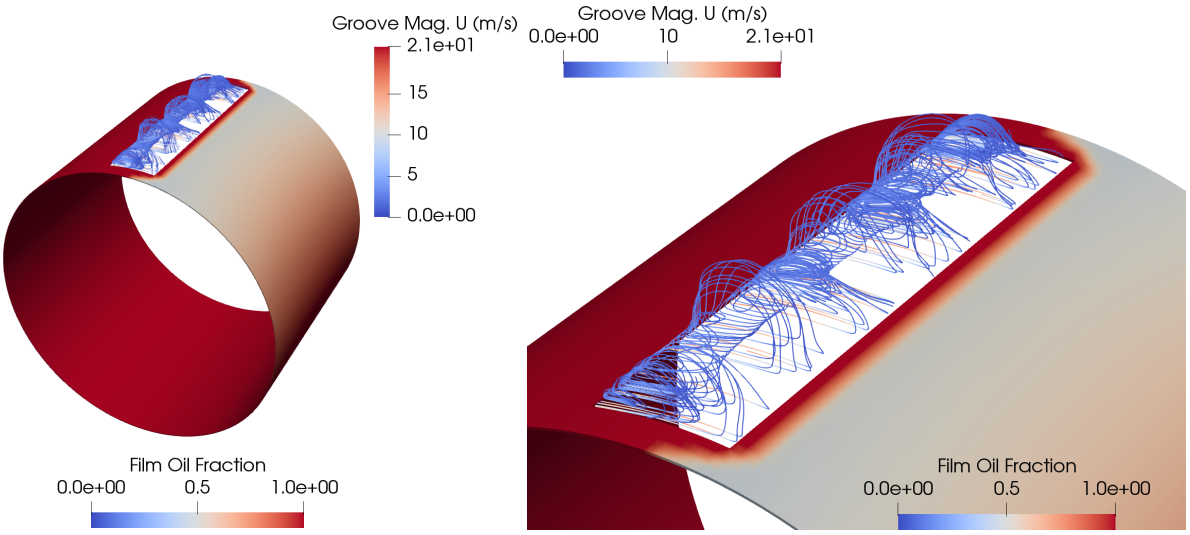

(a) (b)

Figure 5.14: Oil fraction in the Film and streamlines in the Groove contoured with velocity magnitude at 4000rpm and 6kN.

These results in the CFD region verify the solution and shows qualitatively the results are consistent with expected flow behaviour. The solution of pressure is very similar, ¡1%, between the ”TEHL” and ”TEHL+CFD” methodologies. Including the CFD methodology to resolve the flow in the supply groove and a significant effect on the temperature solution, improving the peak temperature prediction from 12% to 6.7%. This provides initial validation of the interfacing methodology proposed in Chapter 4 and verification of the solution from the CFD model. The next section presents a case where the multiphase functionality is shown in the solution, and highlights the potential applications for this numerical model.

5.2 High Pressure Contact Rig

This section presents a preliminary model for a half-journal experimental rig developed by the Mechanical and Aerospace Systems (MAS) research group. The CFD-TEHL OpenFOAM

model is applied for a two-dimensional setup of the experimental configuration with the aim to initially investigate implementing a multiphase model in the CFD methodology and consider the behaviour at the interface with the lubrication model.

5.2.1 Experimental Rig

An experimental rig of a half-journal, High Pressure Contact Rig (HPCR), has been built at the Mechanical and Aerospace Systems (MAS) research group to investigate the hydrodynamic lubrication phenomena in parallel with the development of the TEHL-CFD numerical methodology. A schematic of the experimental setup is shown in Figure 5.15 where a rotating shaft is positioned in a semi-circular block, the bush, to form a thin gap between them where a hydrodynamic lubrication film is formed. Oil is supplied down an angled slope towards the shaft to be drawn into the lubrication region by the downward motion of the shaft surface.

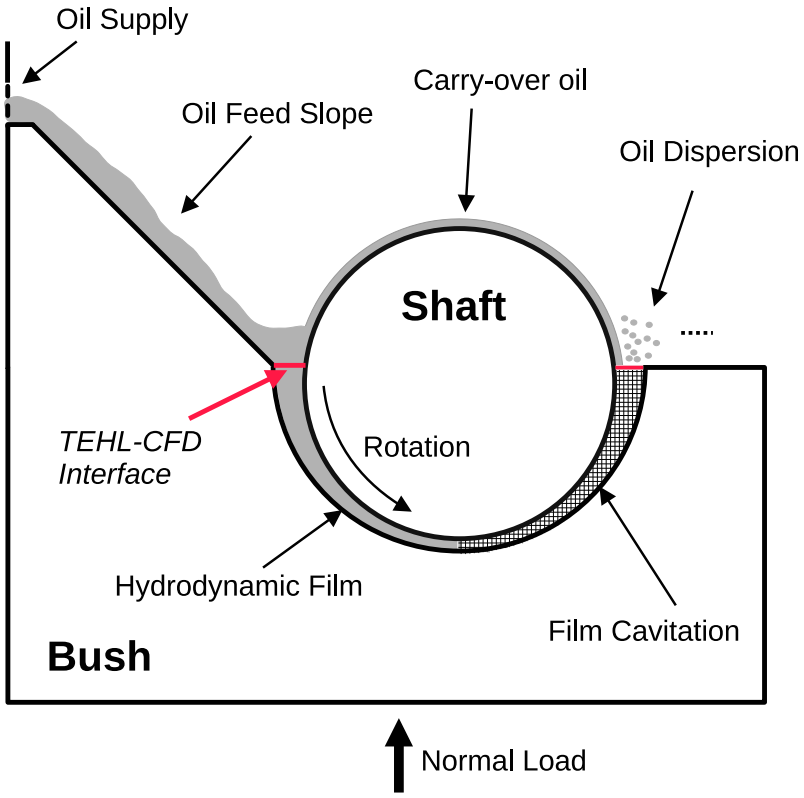

Figure 5.15: Half-journal bearing experimental rig schematic

The dimensions of the experimental rig are listed in Table 5.5

Dimension	Value
Shaft Diameter (mm)	100
Bush Diameter (mm)	100.2
Bush Length (mm)	70
Clearance (μm)	100
Slope Angle ($\circ$)	45

Table 5.5: Half-journal Rig Dimensions

5.2.2 2D Simulation

A two dimensional case study of the experimental rig described in Section 5.2.1 is developed to test the interfacing setup between the TEHL and CFD module including multiphase behaviour. The interfacing with the lubricating film is the primary interest and flow off the sides of the rig is beyond the scope of this study, therefore a 2D setup is used. Figure 5.16 shows the case geometry with the region types highlighted to show the interfacing boundaries.

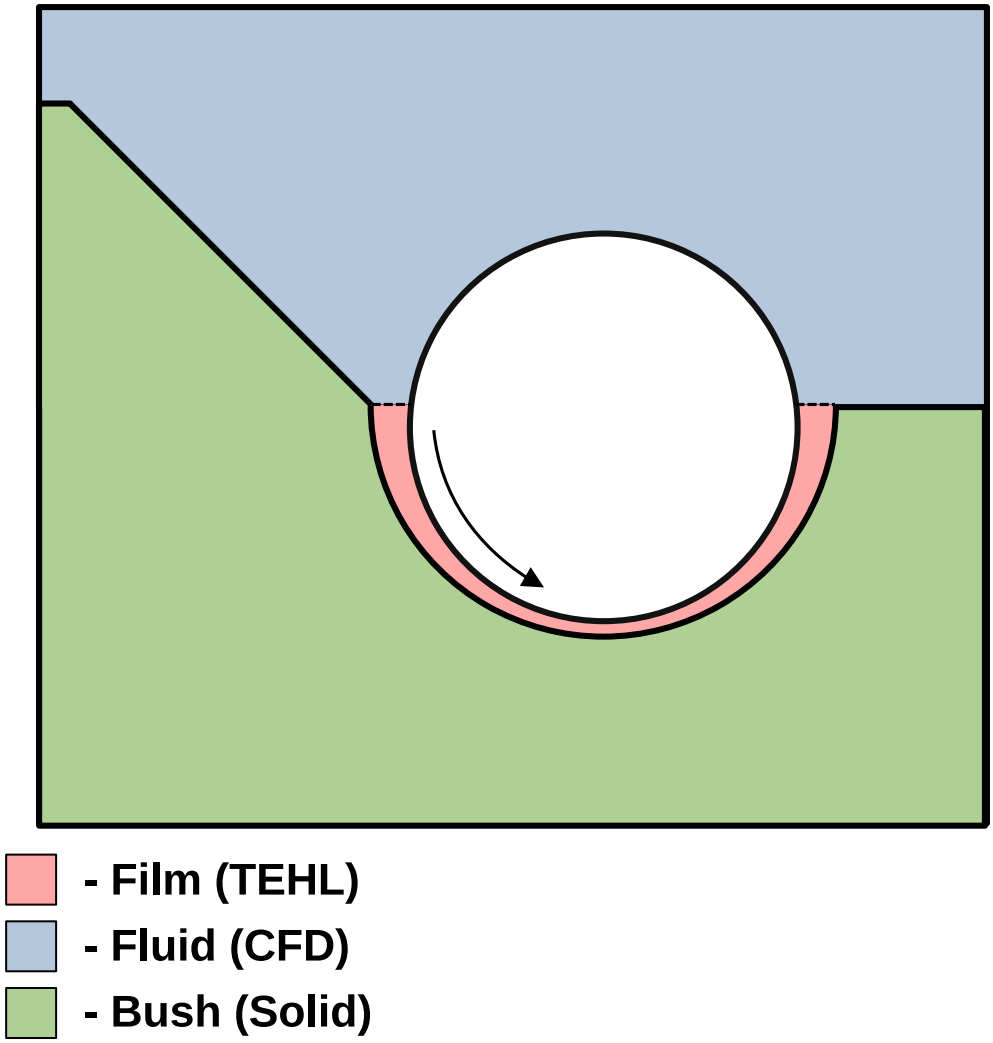

Figure 5.16: Diagram of 2D Case half-Journal

5.2.2.1 Mesh

The dimensions of the hydrodynamic lubrication region creates a multi-scale situation where the CFD region scale is generally of the order of 10mm, whereas the film region is of the order of $100\mu m$, create a difference of a factor of 100. This is particularly influential to the meshing in the CFD region where the cells must reduce to the order of the film region, while also having multiple cells across the height of the film to capture the velocity profile. In the 2D case, the element size is locally reduced in the regions near the inlet and outlet of the film region, which grows towards the bulk of the CFD region to accommodate this change in scale. Figure 5.17 shows the fluid region mesh with the refinement near the interfaces with the film.

A discretisation of 6 cells is enforced across the height of the film at the interface, and a cell size of $70\mu m$ and $150\mu m$ is enforced in the region around the film inlet and outlet interfaces respectively. A finer refinement is applied in the inlet region because of the greater rotational flow in the region as the oil in driven into the narrow gap. In the bulk of the fluid region the cell size is

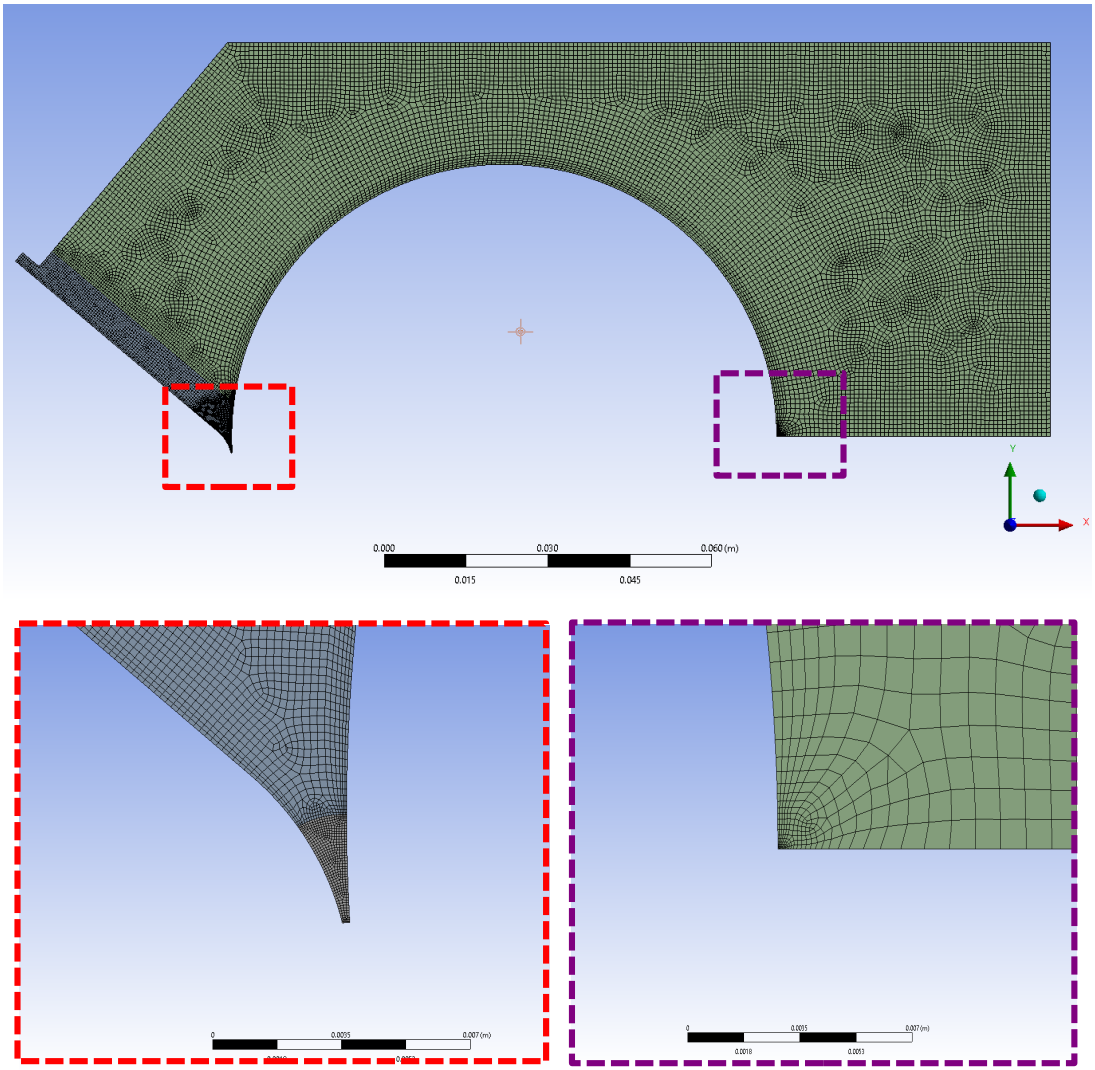

Figure 5.17: Fluid region mesh with the refinement highlighted near the film interfaces.

The multi-scale nature highlights the requirement for careful meshing in the CFD regions for cases with more complex CFD domains. In addition to the refinement towards the film region, a smaller cell size is used across the oil supply slope to approaching the shaft surface where the fluid-air interface is expected. Boundary layers are also applied to the solid walls including the shaft boundary.

Region	Mesh Size
film (TEHL)	160
film 3D (TEHL)	960
bush (Solid)	45899
fluid (CFD)	16783

Table 5.6: HPCR region mesh sizes

The mesh sizes in each region are summarised in Table 5.6. The number of cells across the film height in the 3D film mesh is 6. The bush mesh is made conformal with the film mesh, given the large temperature gradients across this interface is significant, and is non-conformal with the fluid region. The bush region cell size is 0.8mm in the bulk of the domain.

5.2.2.2 Boundary Conditions

The boundary conditions for the TEHL-CFD interfaces at the film inlet and outlet are the same as the journal bearing case in Section 5.1 for the pressure, temperature and velocity fields. In the half-journal model, the CFD region includes the VoF multi-phase model which also needs to be coupled with the TEHL solution. In the TEHL model, the cavitation in the diverging region generates a multi-phase flow which is contained in the relative density field, Θ. This solution given a mixture ratio across the film height, however, the shape of the cavitation region is not a homogeneous mixture and generally regions of gaseous and liquid phase, such as in finger-like cavitation, where the lubricating film arranges into streams, which is assumed in the derivation of the cavitation model. In the current methodology, a method is proposed whereby an assumed distribution of the phases is applied at the film outlet where the lubrication flows out of the TEHL model. The assumed profile is a two layered liquid-gas profile where the liquid phase is attached to the shaft boundary. This profile is assumed based on the results of Hajishafiee *et al.* (2017) which show this distribution in their solutions at the outlet of a EHL point contact. The ratio of liquid phase at the outlet is taken from the solution of Θ in the TEHL model, which estimates the height of the liquid layer. Figure 5.18 shows a schematic of the boundary condition setup between the TEHL model and the VoF model in the CFD region.

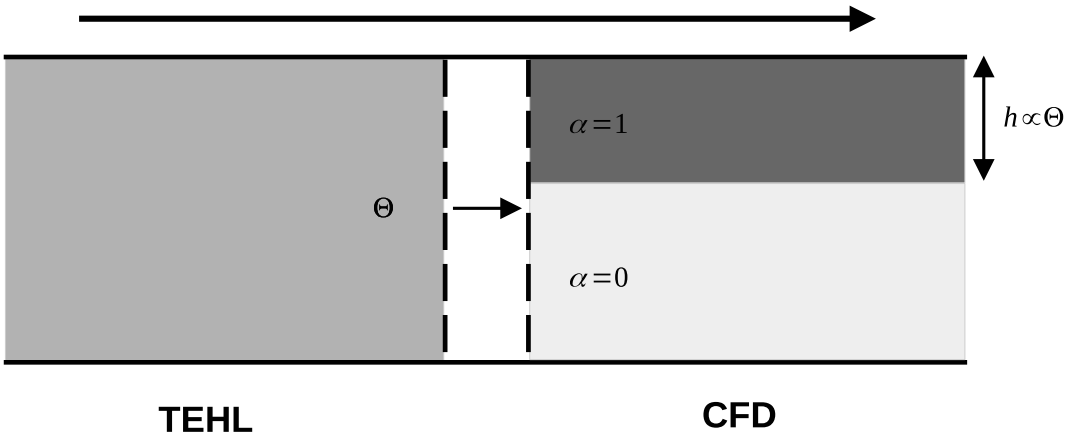

Figure 5.18: Radial distribution boundary condition setup

5.2.2.3 Initialisation

The VoF model requires that the CFD has a transient setup. If this case is started with static initial conditions in the fields an error occurs at the film inlet interface. The TEHL model assumes the lubricating film is fully developed and because of the velocity coupling boundary will prescribe a velocity profile to the film inlet interface. If the initial velocity field is static, the defined velocity profile at the film inlet interface causes the pressure solution to reduce significantly approaching the film inlet. The low pressure at the film inlet effects the pressure solution in the film and causes the solution to diverge. A solution to the inlet pressure problem is to generate an initial solution in the fluid region to develop a velocity profile near the film inlet. The initialisation is performed using the interFOAM solver from OpenFOAM 8 Weller Henry (2020) in the fluid region. The flow of the oil down the supply ramp over 0.052s is shown in Figure 5.19.

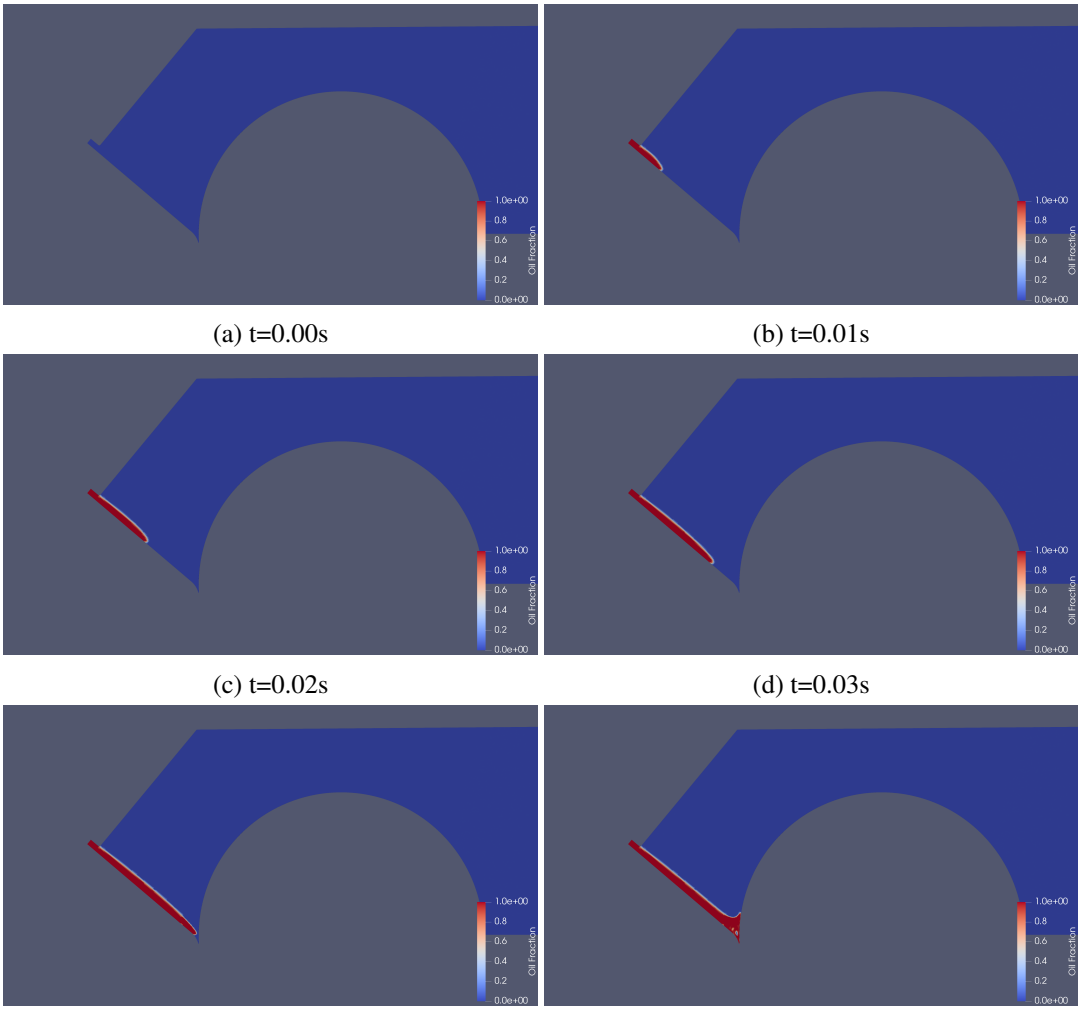

(a) t=0.00s (b) t=0.01s

(c) t=0.02s (d) t=0.03s

(e) t=0.04s (f) t=0.05s

Figure 5.19: Initialisation of the supply oil flow

Figure 5.20 shows the initialised velocity, pressure and oil fraction fields in the fluid region which are used as the initial solution in the multi-region case.

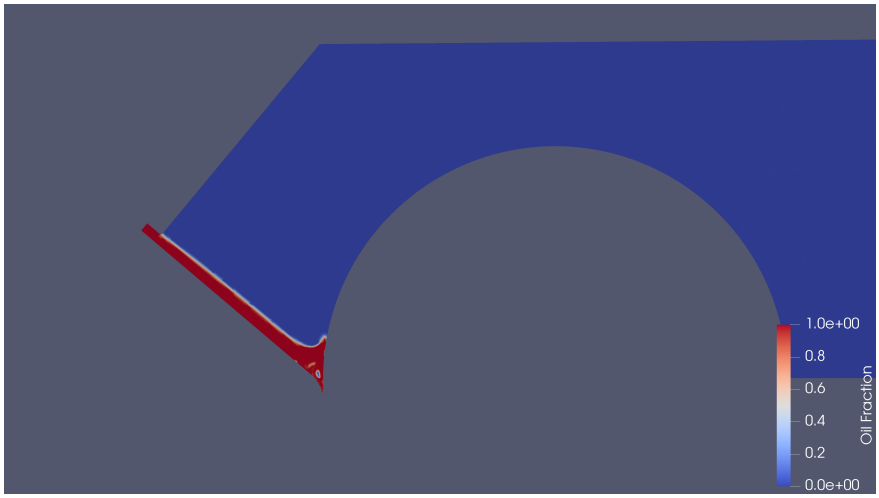

(a) Oil Fraction

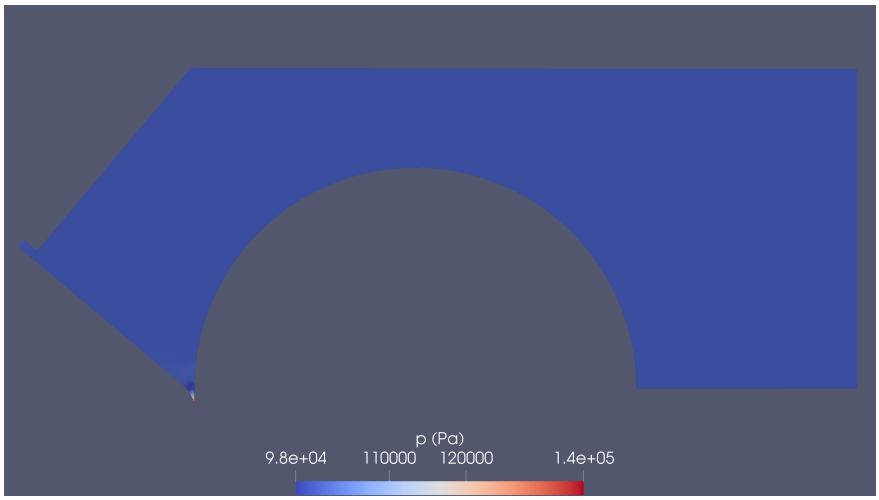

(b) Pressure

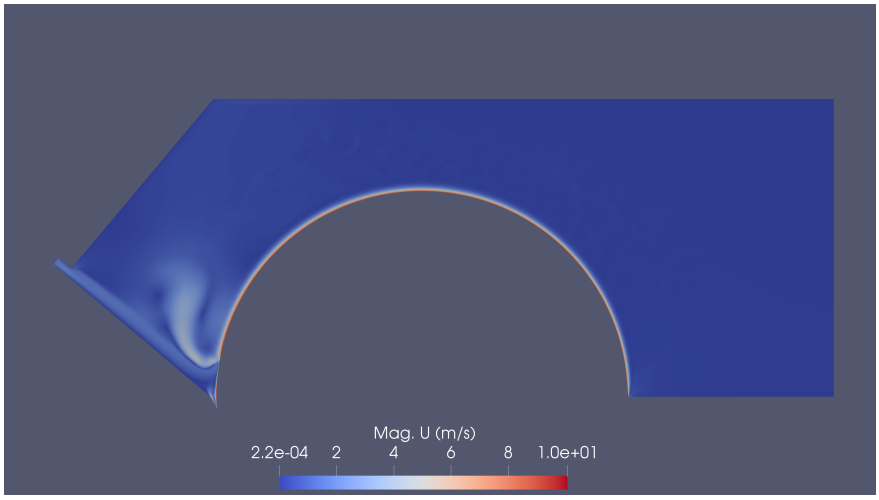

(c) Velocity

Figure 5.20: Initialised fluid region solution.

5.2.2.4 Results

The material properties are summarised in Table 5.7.

Symbol	Value	Units
P_{cav}	1e5	Pa
β	$1x10^8$	Pa
ρ_l	860	$\frac{kg}{m^3}$
ρ_g	1.127	$\frac{kg}{m^3}$
c_{p_l}	2000	$\frac{J}{kgK}$
c_{p_g}	1000	$\frac{J}{kgK}$
μ_l	0.0293	Pas
μ_g	$1.918x10^{-5}$	Pas
k_l	0.13	$\frac{W}{mK}$
k_g	0.025	$\frac{W}{mK}$
γ	-0.04	K^{-1}
T_{ref}	40	$^\circ C$
k_s	50	$\frac{W}{mK}$
k_b	100	$\frac{W}{mK}$
h_{walls}	50	$\frac{W}{m^2}$

Table 5.7: Material and Lubricant Properties

The operating conditions of the case are a rotational speed of the shaft of 2000rpm, the eccentricity of the shaft is fixed at 0.8 and with an angular offset of 0. The elastic and thermal deformation effects are excluded from the numerical procedure, therefore the minimum film height is at BDC of the bush. The simulation is run for a time of 0.0314s, which corresponds to a full rotation of the shaft at 2000rpm. The oil flow around the inlet to the film is shown in Figure 5.21 across the simulation time. The flow shows the pooling of the oil near the inlet as the oil supply feed rate (2D equivalent of 15 l/min in the experimental case) is greater than the flow rate into the film region, approximately 2 l/min. The pooling would be less significant in a 3D case where there would be a side flow off the inlet ramp. The air flow around the shaft is shown to disturb the oil pool that forms, Figure 5.21c, causing the oil to recirculate. The air boundary layer on the shaft is held near the surface as it meets the oil pool and partially reaches the film inlet interface. Preliminary runs of the experimental rig showed that a feed rate of the supply greater than the expected intake of the film was required to develop the lubricating film. The initial results of the 2D simulation could suggest the cause where air is also driven into the film region, thereby disrupting the development of the lubricating film. Capability to investigate the flow of the oil preceding the film region is key advantage to the

coupling methodology.

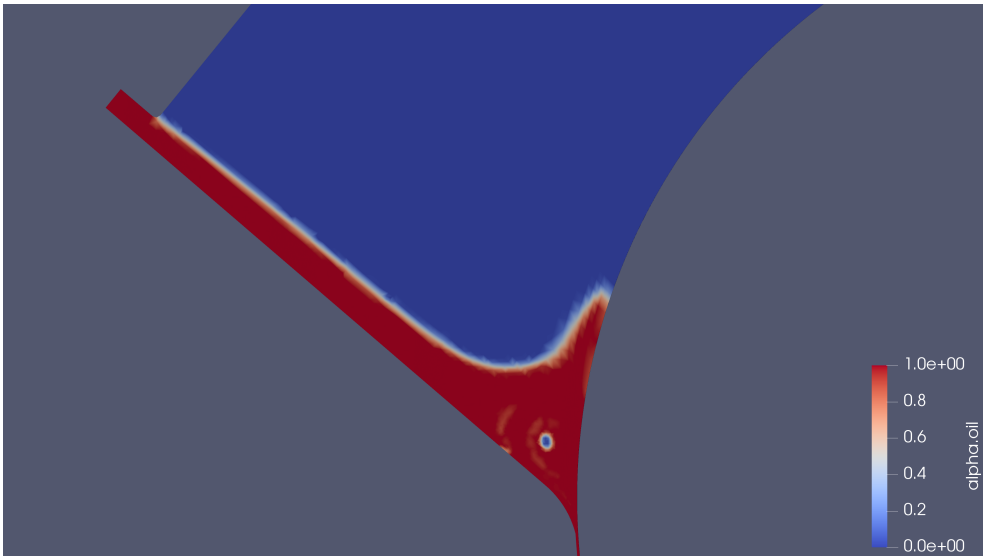

(a) t=0.008s

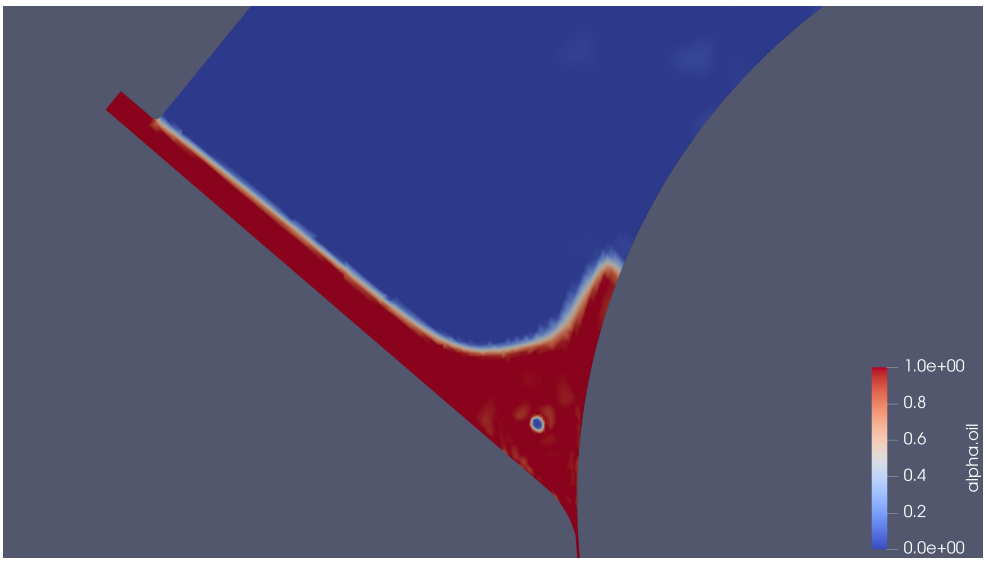

(b) t=0.016s

Figure 5.21: Oil fraction solutions near the film inlet

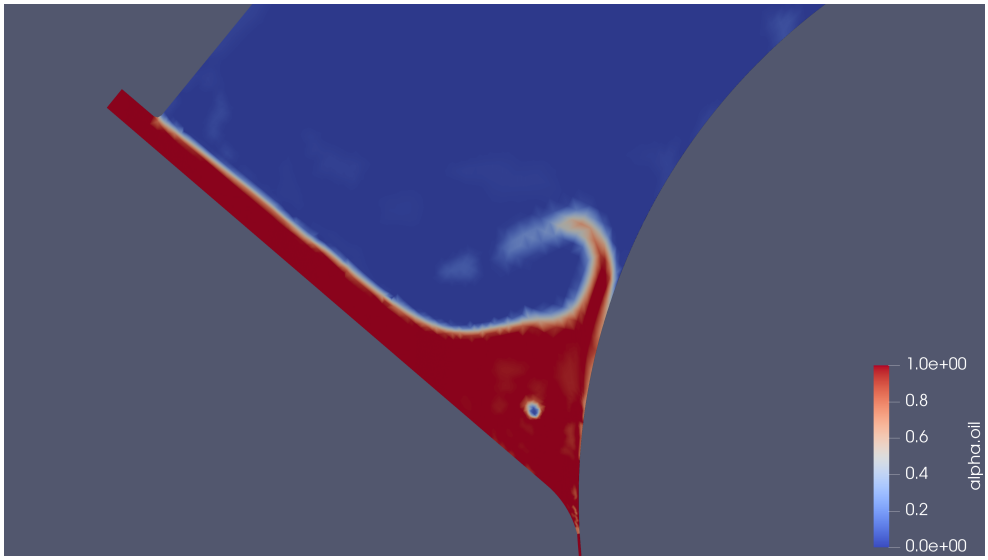

(c) t=0.024s

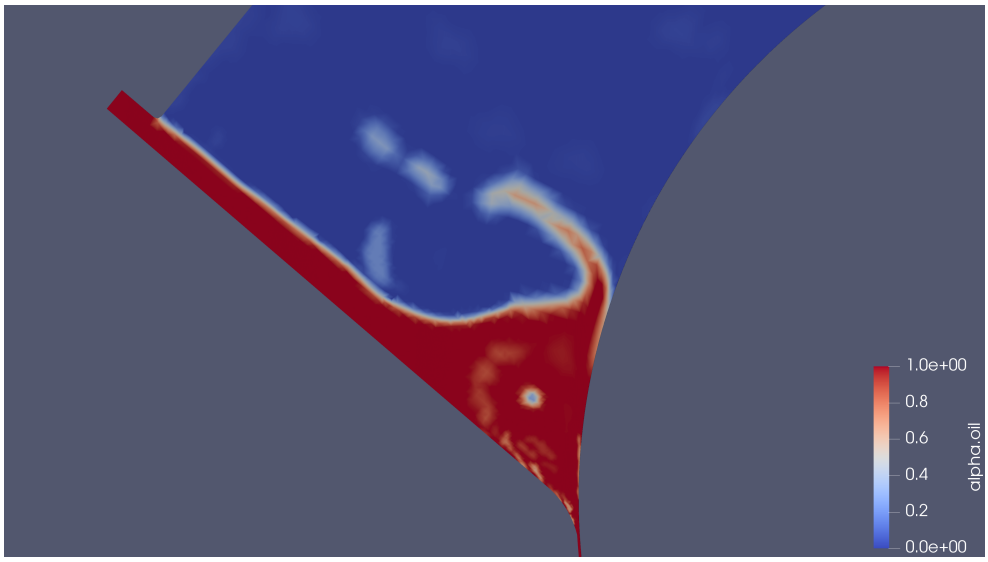

(d) t=0.031s

Figure 5.21: Oil fraction solutions near the film inlet (cont.)

Figure 5.22 shows the solutions in the fluid domain at time 0.031s for the oil fraction, Figure 5.22a, and the velocity, Figure 5.22b. The oil fraction in Figure 5.22a shows some recirculating flow of the oil from the film outlet which is carried on the shaft surface, however the values are < 1 with no clear interfaces between the phases. The amount of fluid phase from the film outlet is small, occupying a fraction of the film outlet area, and the growth of the cell adjacent to the shaft wall means the thin oil layer on the shaft could not be accurately captured in the current setup. A greater refinement near the shaft wall would be required to accurately account for the carried over oil from the film outlet. The velocity field clearly shows a flow adhering to

the shaft wall from the outlet, which forms a boundary layer on the surface until it meets the supply oil.

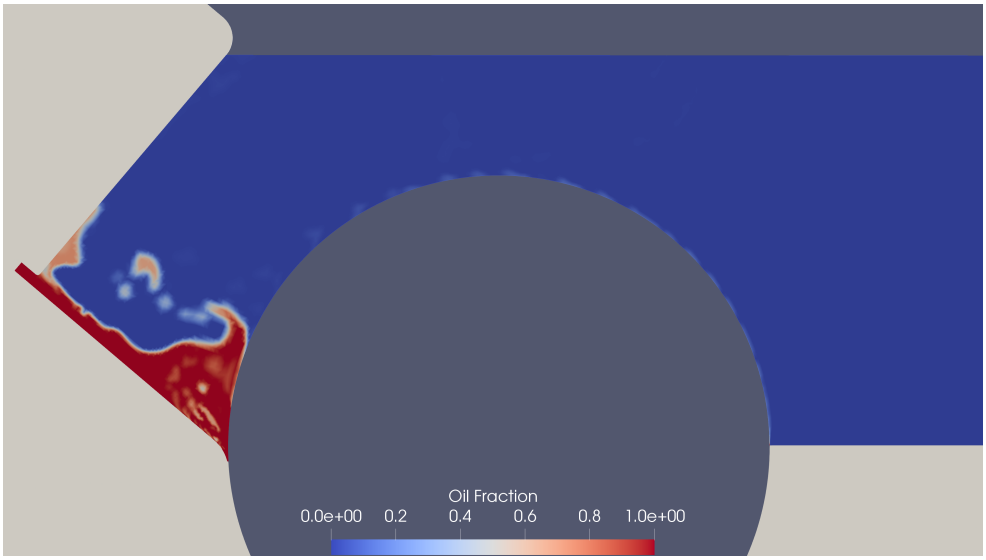

(a) Oil Fraction

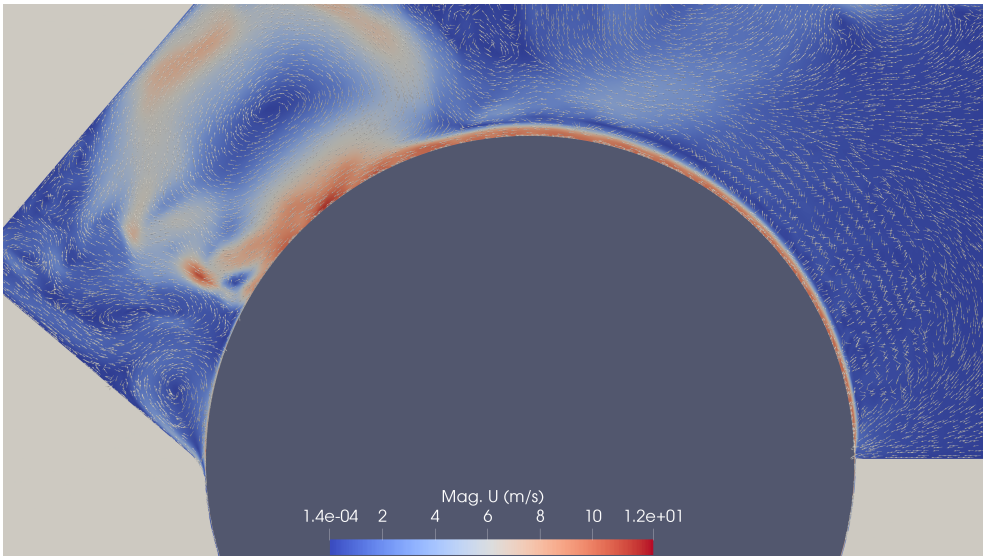

(b) Pressure

Figure 5.22: Field solutions at time 0.031s

The field solution near the film inlet at time 0.031s are presented in Figure 5.23. The air boundary layer that remains attached to the wall is clearly shown in Figure 5.23a, and appears to be the dominant phase Advent to the interface and highlights a problem with the current coupled boundary condition setup. In the TEHL model, the value for Θ, relative density in the cavitation model, is calculated from the pressure solution in the CFD region using Equation 3.5. However, this assumes a full supply of oil which is clearly not shown in the fluid

regions results and causes the disconnect of the solution with the film region shown in Figure 5.23a. To improve the continuity of the solution of the oil fraction across the interface is this case would require the coupling with the TEHL model to be dependent of on the oil fraction solution in the fluid region. However, this will affect the continuity of the pressure solution, shown in Figure 5.23b because the Elrod-Adam cavitation algorithm used in the TEHL model would associate an oil fraction of < 1 as being at the cavitation pressure, therefore creating a disconnect in the pressure solution. This challenge in the coupling between the region because of the assumption behind the Elrod-Adams cavitation model could highlight a limitation in this cavitation approach. Coupling approaches with alternative cavitation models deserves further investigation.

The velocity solution near the interface Figure 5.23c shows good continuity between the CFD and TEHL models. The complex flow near the film inlet is also highlighted with two large vertices forming in the domain. The temperature field, Figure 5.23d is predominantly uniform in the fluid solution and the heat generating in the film region is as it is sheared is clearly seen.

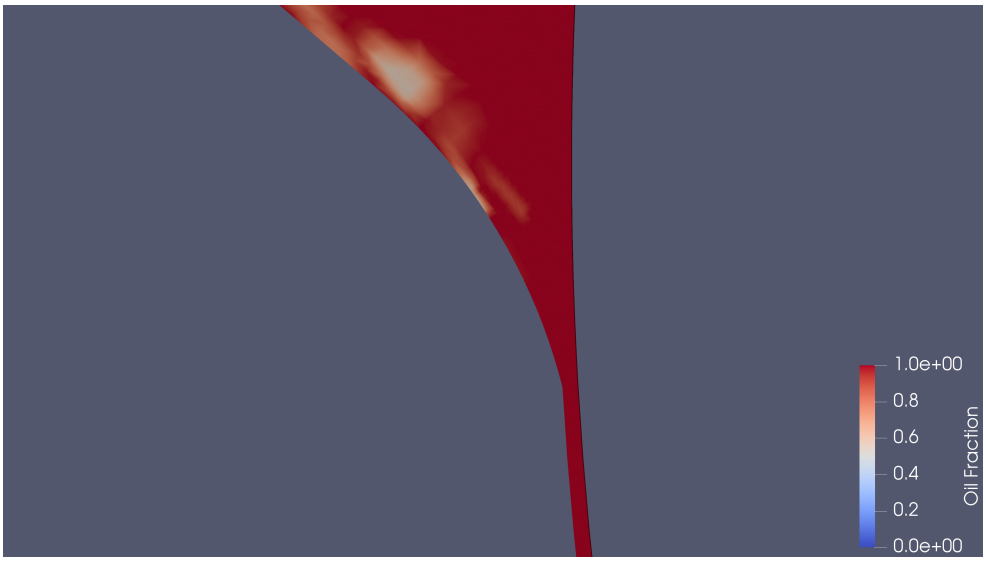

(a) Oil Fraction

Figure 5.23: Solution near the film inlet at time 0.031s

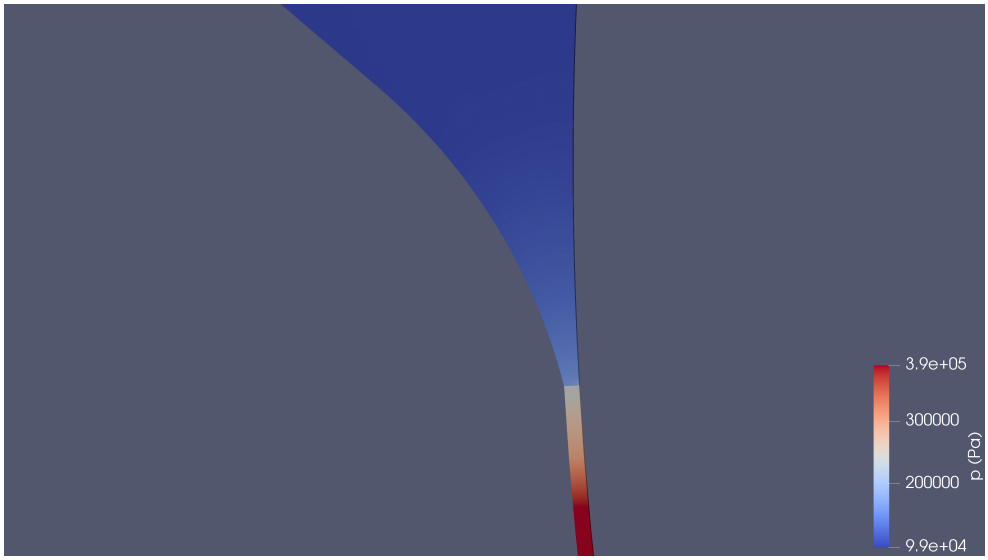

(b) Pressure

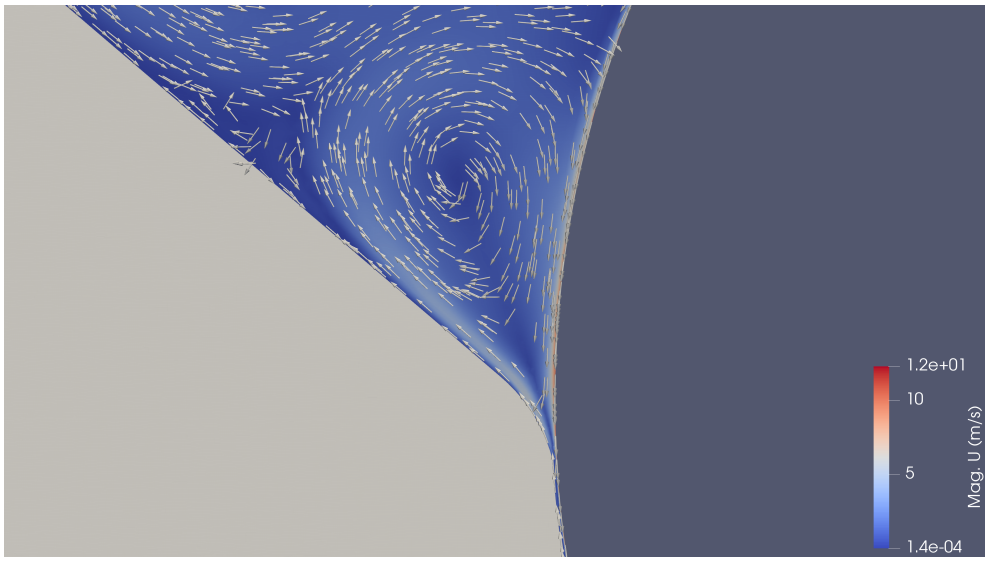

(c) Velocity

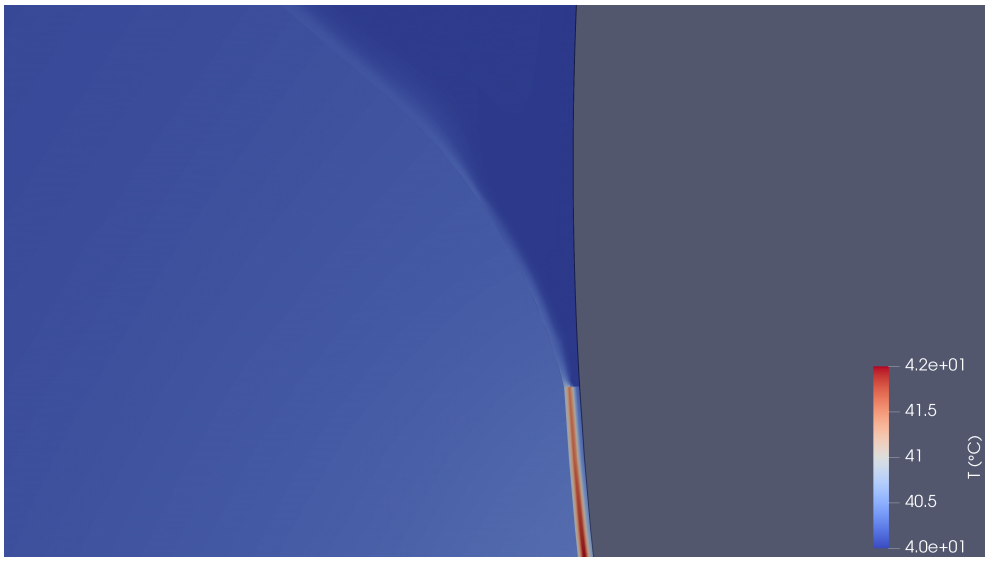

(d) Temperature

Figure 5.23: Solution near the film inlet at time 0.031s (cont.)

The solutions near the outlet of the film are shown in Figure 5.24. The oil fraction coupling boundary is clearly shown in Figure 5.24a where the value in the film region is approximately 0.3, which is reflected in the portion of the outlet boundary which is occupied by oil. The dispersion of the oil phase as the mesh size increases along the shaft boundary is also clearly shown which suggests a greater refinement is required along the boundary. The velocity field near the outlet, shown in Figure 5.24b highlights the boundary layer which forms on the shaft wall which would carry round the oil phase from the outlet, which is also reflected in the temperature field, Figure 5.24c.

(a) Oil Fraction

Figure 5.24: Solution at the film outlet at time 0.031s with the shaft boundary on the left side rotating anti-clockwise.

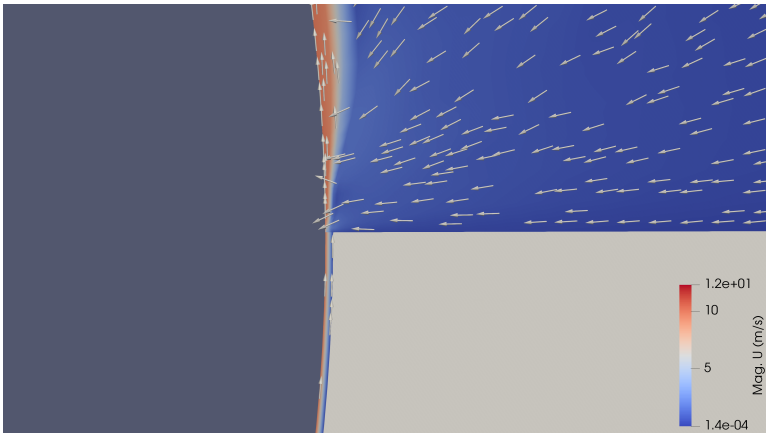

(b) Velocity

(c) Temperature

Figure 5.24: Solution at the film outlet at time 0.031s with the shaft boundary on the left side rotating anti-clockwise. (cont.)

The progression of the temperature field in the case is shown in Figure 5.25. The heat from the film outlet is carried around by the flow around the shaft until it meets the supply oil and dissipates into the bulk of the domain around the oil supply. The temperature in the film and bush is constant across the simulation because of the steady-state setup.

(a) t=0.008s

(b) t=0.016s

Figure 5.25: Temperature solution across the domain

(c) t=0.024s

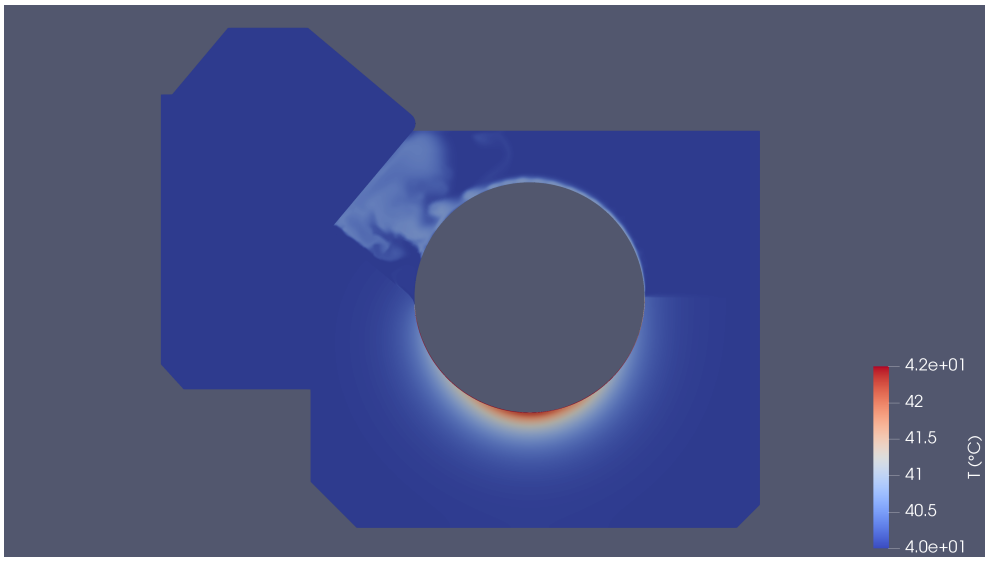

(d) t=0.031s

Figure 5.25: Temperature solution across the domain (cont.)

This section presents a preliminary case for the CFD-TEHL coupled methodology which incorporates multiphase flow. The case highlights a uncertainty from the TEHL methodology which is that the exact regime of flow in the cavitation region is unknown. A profile is assumed at the interface which reflects results from CFD models of hydrodynamic lubrication regimes, however it is uncertain if this is appropriate for all operating conditions. Furthermore, a inconsistency in the coupling with the film inlet is identified due to the cavitation algorithm's pressure density function. Cavitation models based on fluid rheology offer a more complete description of the fluids state, and could therefore improve the coupling of the solution at the

interface for multi-phase cases.

5.3 Summary

In this chapter the TEHL-CFD coupling methodology described in Chapter 4 is applied to two cases; a journal bearing which provides some initial validation for the numerical model, and a half-journal rig with a broader CFD region with multi-phase effects. In the journal bearing case, the solution shows good agreement with the experimental results when comparing the profiles of temperature and pressure, and when comparing key variables across a range of operating conditions. Qualitatively, the flow patterns observed in the CFD groove region show good agreement with the expected behaviour from previous results from literature which investigate the flow in the groove. Direct quantitative validation of the CFD model in the case of the journal bearing is challenging because of low availability of validation data for the groove region. The agreement of the solution in the lubrication region gives an indirect validation of the CFD regions solution, however more cases comparing to experimental results are need to fully validate the coupling methodology. The half-journal experimental rig provides an opportunity to validate the coupled model at higher load and speed conditions in future studies. The capability of the rig to capture the film thickness profile offers further variable to compare and investigate but is not presented here. The visibility of the wider domain can also provide an opportunity for qualitative comparison of the outflow from the lubrication region and the interface in the numerical model. Further work to extend the numerical model of the half-journal rig to a three-dimensional case is needed, as was conducted for the journal bearing case, which can then be compared to the results of the experimental case. Future applications could also include modelling the side leakage from a journal bearing which includes the effects from the lubrication region to improve the prediction of the oil disintegration behaviour.

Chapter 6

Conclusions

This thesis describes a novel numerical methodology for thermal elasto-hydrodynamic lubrication simulation within OpenFOAM which is coupled within a CFD framework. The methodology uses a multi-region setup which applies the systems of equations separately in a sequential procedure to converge towards a coupled solution. Coupling between the TEHL and CFD resolved regions is applied using boundary conditions detailed in Chapter 4. The proposed method of coupling is to prescribe the pressure at the interface using the CFD solution and the velocity using the TEHL solution, creating a two-way coupling by inversely one-way coupling the pressure and velocity solutions. A scaling factor is introduced during the velocity coupling to scale the profile such that the mass flow between the solution is consistent, as shown in Chapter 4.2. The temperature coupling setup between the region is dependent on the flow direction, varying between inlet and outlet setups across the boundary faces.

The complete methodology is validated against experimental results from literature using a journal bearing case study in Chapter 3. The results show excellent agreement in the pressure field within the film and the peak values are generally within 2% across the tested parameter range. The temperature field is shown to be predicted within approximately 8% at high speed and load compared to the experimental results. This is attributed to the overestimation of the inlet temperature to the film, approximately 12%, from using the mixing approximation between the supply and recirculating oil.

The coupled TEHL-CFD numerical framework is validated on a full journal bearing case in

Chapter 5 to verify the solution of the CFD methodology. The results show an improvement of the peak temperature prediction in the bush from 8% to 3.7%. This is largely attributed to the improvement in the inlet temperature prediction which changed from 12% to 6.7% after including the CFD methodology in the supply groove. A qualitative validation of the model is shown by the continuity of the fields solution across the interfaces. In addition to the journal bearing cases, a study of a half-journal experimental rig is presented in Chapter 5 which is used to verify the performance of the numerical model is an additional case which includes the multiphase model. The case incorporates the proposed multiphase coupling approach which requires as assumed distribution of phases in the two-phase cavitation region. The field solutions at the interfaces also show good continuity which provide qualitative validation on the numerical model performance.

6.1 Contributions

1. This study implements the Reynolds based lubrication model within an open-source CFD software, OpenFOAM, using the finite-volume method which is detailed in Layton et al. [2023]. While other studies have implemented the methodology in OpenFOAM, this study incorporates more physical behaviour including temperature and elastic deformation.

2. This research extends the hydrodynamic lubrication modelling methodology by coupling the model with a CFD methodology. This is the first study to consider coupling between Reynolds based lubrication modelling and CFD which has been presented at the UK Heat Transfer conference Layton *et al.* (2024). This novel numerical setup provides a foundation for incorporating hydrodynamic lubrication modelling techniques within CFD frameworks for applications in transmissions system simulations.

3. The interfacing between the lubrication model and CFD is investigated and validated. This provides confidence in the coupled numerical methodology to be applied to practical cases in industry.

4. The implementation in OpenFOAM provides a flexible software which is capable for modelling cases beyond those investigated in this study

6.2 Future Work

A limitation for the TEHL-CFD methodology is the uncertainty in the phase distribution in the cavitation region which is not available from the solution of the Elrod-Adam algorithm. This could be improved with alternative cavitation models from the field of Tribology which are based on fluid Rheology, for example the recent study by Palavecino *et al.* (2024) which incorporated the the Rayleigh Plesset equation to develop a cavitation model for Reynolds based simulation. Investigating alternative cavitation models for the TEHL-CFD simulation could provide a more accurate physical representation at the outlet in multiphase cases, which would have particular applications in simulation the lubrication through rolling elements.

The scope of this study is primarily focused towards journal bearings neglecting other hydrodynamic lubrication components such as thrust and rolling element bearing. The magnitude of pressure in the journal bearing cases investigated in this project are lower compared to other region such as the point contacts in rolling element bearings which can reach the GPa range. At this magnitude the pressure dependence of viscosity and the deformation effects are more significant. The performance of the OpenFOAM TEHL model developed in Chapter 3 is not validated for this range and requires further study investigate the performance for these cases.

The journal bearing study in Chapter 5 provides a basis to study the effect of the groove shape on the lubrication performance as the fluid flow dynamics can be incorporated into the same simulation as the Reynolds lubrication model. This could identify primary design parameters for the oil supply of journal bearing to optimise the shape to the operating conditions. The journal bearing model could also be interfaced with a domain adjacent to the sides of the bearing to model the side leakage and following disintegration behaviour of the oil. The temperature of the oil and a non-uniform velocity profile would be provide by the TEHL solution and improve the prediction of the oil disintegration in comparison to models such as Berthold *et al.* (2018).

Developing the solid region in the CFD-TEHL OpenFOAM to incorporate an elastic model to solve for the displacement of the surface would improve the accuracy of the deformation prediction. The influence of complex geometries and features, such as measurement equipment embedded in the bush of a journal bearing, could not be accurately modeled by the half-space

approximation while an elastic solid model would be more applicable and be able to incorporate thermal expansion effects. The temperature dependence of the solid properties could also be incorporated into the TEHL-CFD methodology to improve the solution for cases with higher variations of temperature.

Future work would also include applying the TEHL-CFD model to new scenarios. Following validation of the model for higher pressure case such as rolling elements, the coupled model can be applied to investigate the ejection of the oil from the point contacts. This would be similar to investigation the side leakage from the journal bearing in Berthold *et al.* (2018). Thrust bearings are also a potential application for the model to investigate. The flow of oil supplied between the pads could be effectively modelled by the CFD methodology to investigate the lubrication performance of the bearing. Furthermore, the ejection of the oil from the sides of the thrust bearing could be investigated with simulated solutions of the velocity and temperature profiles from the lubrication region.

Bibliography

Ahmad, Mohamad Ali, Kasolang, Salmiah, & Dwyer-Joyce, R S. 2014. Experimental study on the effects of oil groove location on temperature and pressure profiles in journal bearing lubrication. *Tribology International*, **74**(1), 79–86.

Alakhramsing, Shivam, van Ostayen, Ron, & Eling, Rob. 2015. Thermo-Hydrodynamic Analysis of a Plain Journal Bearing on the Basis of a New Mass Conserving Cavitation Algorithm. *Lubricants*, **3**(2), 256–280.

Albahrani, S. M.B., Philippon, D., Vergne, P., & Bluet, J. M. 2016. A review of in situ methodologies for studying elastohydrodynamic lubrication. *Proceedings of the Institution of Mechanical Engineers, Part J: Journal of Engineering Tribology*, **230**(1), 86–110.

Almqvist, T, & Larsson, R. 2002. The Navier-Stokes approach for thermal EHL line contact solutions. *Tribology International*, **35**(3), 163–170.

Almqvist, T, Almqvist, A, & Larsson, R. 2004. A comparison between computational fluid dynamic and Reynolds approaches for simulating transient EHL line contacts. *Tribology International*, **37**(1), 61–69.

Ardah, Suhaib, Profito, Francisco J, & Dini, Daniele. 2023. An integrated finite volume framework for thermal elasto-hydrodynamic lubrication. *Tribology International*, **177**(1), 107935.

Bair, S., Qureshi, F., & Winer, W. O. 1993. Observations of Shear Localization in Liquid Lubricants Under Pressure. *Journal of Tribology*, **115**(3), 507–513.

Banwait, S. S., & Chandrawat, H. N. 1998. Study of thermal boundary conditions for a plain journal bearing. *Tribology International*, **31**(6), 289–296.

Barus, C. 1893. Isothermals, Isopiestics and Isometrics relative to Viscosity. *American Journal of Science*, **3**(266), 87–96.

Bayada, G., & Chupin, L. 2013. Compressible fluid model for hydrodynamic lubrication cavitation. *Journal of Tribology*, **135**(4), 041702.

Berthold, Martin, Morvan, Hervé, Young, Colin, & Jefferson-Loveday, Richard. 2018. Toward Investigation of External Oil Flow From a Journal Bearing in an Epicyclic Gearbox. *Journal of Engineering for Gas Turbines and Power*, **140**(6), 062501.

Berthold, Martin, Jefferson-Loveday, Richard, Young, Colin, Rothwell, Benjamin C, & Ambrose, Stephen. 2019. Multiphase Computational Fluid Dynamics Modelling of External Oil Flow From a Journal Bearing. *ASME. J. Eng. Gas Turbines Power*, **141**(5), 051002.

Bouyer, J, & Fillon, M. 2002. An Experimental Analysis of Misalignment Effects on Hydrodynamic Plain Journal Bearing Performances. *ASME. J. Tribol.*, **124**(2), 313–319.

Bouyer, J., & Fillon, M. 2004. On the Significance of Thermal and Deformation Effects on a Plain Journal Bearing Subjected to Severe Operating Conditions. *Journal of Tribology*, **126**(4), 819–822.

Bouyer, J, & Fillon, M. 2011. Experimental measurement of the friction torque on hydrodynamic plain journal bearings during start-up. *Tribology International*, **44**(7-8), 772–781.

Brewe, D E. 1986. Theoretical Modeling of the Vapor Cavitation in Dynamically Loaded Journal Bearings. *ASME. J. Tribol.*, **108**(4), 628–637.

Bruyere, V., Fillot, N., Morales-Espejel, G. E., & Vergne, P. 2012. Computational fluid dynamics and full elasticity model for sliding line thermal elastohydrodynamic contacts. *Tribology International*, **46**(1), 3–13.

Bruyere, V., Fillot, N, Morales-Espejel, G E, & Vergne, P. 2017. A two-way FSI analysis of multiphase flow in hydrodynamic journal bearing with cavitation. *J Braz. Soc. Mech. Sci. Eng.*, **39**(3), 3399–3412.

Cameron, A, & Wood, Mrs W L. 1949. The Full Journal Bearing. *Proceedings of the Institution of Mechanical Engineers.*, **161**(1), 59–72.

Chen, Yu, Sun, Yu, & Cao, Chunping. 2018. Investigations on influence of groove shapes for the journal bearing in high-speed and heavy-load press system. *Industrial Lubrication and Tribology*, **70**(1), 230–240.

Chen, Yu, Sun, Yu, Qiang He, ·, & Feng, Jun. 2019. Elastohydrodynamic Behavior Analysis of Journal Bearing Using Fluid-Structure Interaction Considering Cavitation. *Arabian Journal for Science and Engineering*, **44**(1), 1305–1320.

Cheng, H. S. 1965. A refined solution to the thermal-elastohydrodynamic lubrication of rolling and sliding cylinders. *ASLE Transactions*, **8**(4), 397–410.

Costa, L., Miranda, A. S., Fillon, M., & Claro, J. C.P. 2003. An analysis of the influence of oil supply conditions on the thermohydrodynamic performance of a single-groove journal bearing. *Proceedings of the Institution of Mechanical Engineers, Part J: Journal of Engineering Tribology*, **217**(2), 133–144.

Crook, A. W. 1961. The lubrication of rollers II. Film thickness with relation to viscosity and speed. *Philosophical Transactions of the Royal Society of London. Series A, Mathematical and Physical Sciences*, **254**(1040), 223–236.

Dawson, P H. 1984. Windage loss in larger high-speed gears. *Proceedings of the Institution of Mechanical Engineers*, **198**(1), 51–59.

De Boer, Gregory, & Dowson, Duncan. 2018. An Arbitrary Lagrangian-Eulerian Formulation for Modelling Cavitation in the Elastohydrodynamic Lubrication of Line Contacts. *Lubricants*, **6**(13), 13.

Department For Transport. 2022. *Jet Zero Strategy: Delivering net zero aviation by 2050*. Tech. rept. Department For Transport.

Dhande, D Y, & Pande, D W. 2018. Multiphase flow analysis of hydrodynamic journal bearing using CFD coupled Fluid Structure Interaction considering cavitation. *Journal of King Saud University - Engineering Sciences*, **30**(4), 345–354.

Dhande, D Y, & Pande, · D W. 2017. A two-way FSI analysis of multiphase flow in hydrodynamic journal bearing with cavitation. *Journal of Brazilian Society of Mechanical Sciences and Engineering*, **39**(9), 3399–3412.

Diab, Y., Ville, F., & Velex, P. 2006. Investigations on power losses in high-speed gears. *Proceedings of the Institution of Mechanical Engineers, Part J: Journal of Engineering Tribology*, **220**(3), 191–198.

Dobrica, Mihai B, Fillon, Michel, & Maspeyrot, Patrick. 2006. Mixed Elastohydrodynamic Lubrication in a Partial Journal Bearing-Comparison Between Deterministic and Stochastic Models. *Journal of Tribology*, **128**(4), 778–788.

Dowson, D., & Higginson, G. R. 1959. A Numerical Solution to the Elasto-Hydrodynamic Problem. *Journal of Mechanical Engineering Science*, **1**(1), 6–15.

Dowson, D., & Higginson, G. R. 1966. *Elasto-hydrodynamic lubrication the fundamentals of roller and gear lubrication* . Oxford: Pergamon Press.

Dowson, D, & Taylor, C M. 1979. Cavitation in Bearings. *Ann. Rev. Fluid M echo*, **11**(1), 35–66.

Dowson, D., & Whitaker, A. V. 1965. A Numerical Procedure for the Solution of the Elasto-hydrodynamic Problem of Rolling and Sliding Contacts Lubricated by a Newtonian Fluid. *Proceedings of the Institution of Mechanical Engineers, Conference Proceedings*, **180**(2), 57–71.

Dwyer-Joyce, R. S., Drinkwater, B. W., & Donohoe, C. J. 2003. The measurement of lubricant-film thickness using ultrasound. *Proceedings of the Royal Society A: Mathematical, Physical and Engineering Sciences*, **459**(2032), 957–976.

Dwyer-Joyce, R S, Reddyhoff, T, Drinkwater, B W, & S1, Sheffield. 2004. Operating Limits for Acoustic Measurement of Rolling Bearing Oil Film Thickness Operating Limits for Acoustic Measurement of Rolling Bearing Oil Film Thickness. *Tribology Transactions*, **47**(3), 366–375.

Dyson, A. 1966. Investigation of the Discharge-Voltage Method of Measuring the Thickness of Oil Films Formed in a Disc Machine under Conditions of Elastohydrodynamic Lubrication. *Proceedings of the Institution of Mechanical Engineers*, **181**(1), 633–652.

Dyson, A, Naylor, H, & Wilson, A R. 1965. The Measurement of Oil-film Thickness in

Elastohydrodynamic Contacts. *Proceedings of the Institution of Mechanical Engineers, Conference Proceedings.*, **180**(2), 119–134.

Eastwick, Carol N, & Johnson, Graham. 2008. Gear Windage: A Review. *Journal of Mechanical Design*, **130**(3), 034001.

Elrod, H. G. 1981. A Cavitation Algorithm. *Journal of Lubrication Technology*, **103**(3), 350–354.

Elrod, H. G., & Adam M. L. 1974. A Computer Program for Cavitation and Starvation Problems. *Cavitation and Related Phenomena in Lubrication*, **37**(1), 37–41.

European Commission, Directorate-General for Mobility and Transport, & Directorate-General for Research and Innovation. 2011. *Flightpath 2050-Europe's vision for aviation-Maintaining global leadership and serving society's needs*. Tech. rept. Publications Office.

Ferron, J., Frene, J., & Boncompain, R. 1983. A Study of the Thermohydrodynamic Performance of a Plain Journal Bearing Comparison Between Theory and Experiments. *Journal of Lubrication Technology*, **105**(3), 422–428.

Fesanghary, M, & Khonsari, M M. 2011. A Modification of the Switch Function in the Elrod Cavitation Algorithm. *Journal of Tribology*, **133**(2), 024501.

Floberg, L. 1974. Cavitation boundary conditions with regard to the number of streamers and tensile strength of the liquid. *Cavitation and Related Phenomena in Lubrication*, 31–36.

Giacopini, Matteo, Fowell, Mark T., Dini, Daniele, & Strozzi, Antonio. 2010. A mass-conserving complementarity formulation to study lubricant films in the presence of cavitation. *Journal of Tribology*, **132**(4), 041702.

Glahn, A, Busam, S, Blair, M F, Allard, K L, & Wittig, S. 2002. Droplet Generation by Disintegration of Oil Films at the Rim of a Rotating Disk. *Journal of Engineering for Gas Turbine and Power*, **124**(1), 117–124.

Gumbel, L K R. 1921. Vergleich der Ergebrusse der rectiner-ischen Behandling des Lagerschmierangsproblem mit neueren Versuchsergebrussen. *Monatsbl. Berliner Bez. Verh. Dtsch. Ing.*, 125–128.

Guo, Feng, Yang, Peiran, & Qu, Shiyue. 2001. On the Theory of Thermal Elastohydrodynamic Lubrication at High Slide-Roll Ratios-Circular Glass-Steel Contact Solution at Opposite Sliding. *Journal of Tribology*, **123**(1), 816–821.

Habchi, W. 2014. A numerical model for the solution of thermal elastohydrodynamic lubrication in coated circular contacts. *Tribology International*, **73**(1), 57–68.

Habchi, W, Eyheramendy, D, Vergne, P, & Morales-Espejel, G. 2008a. A Full-System Approach of the Elastohydrodynamic Line/Point Contact Problem. *Journal of Tribology*, **130**(2), 021501.

Habchi, W., Eyheramendy, D., Bair, S., Vergne, P., & Morales-Espejel, G. 2008b. Thermal elastohydrodynamic lubrication of point contacts using a Newtonian/generalized Newtonian lubricant. *Tribology Letters*, **30**(1), 41–52.

Hajishafiee, A, Kadiric, A, Ioannides, S, & Dini, D. 2017. A coupled finite-volume CFD solver for two-dimensional elasto-hydrodynamic lubrication problems with particular application to rolling element bearings. *Tribology International*, **109**(5), 258–273.

Hamrock, B. J., & Dowson, D. 1976a. Isothermal Elastohydrodynamic Lubrication of Point Contacts: Part 1—Theoretical Formulation. *Journal of Lubrication Technology*, **98**(2), 223–228.

Hamrock, B. J., & Dowson, D. 1976b. Isothermal Elastohydrodynamic Lubrication of Point Contacts: Part II—Ellipticity Parameter Results. *Journal of Lubrication Technology*, **98**(3), 375–381.

Hamrock, B. J., & Dowson, D. 1977. Isothermal Elastohydrodynamic Lubrication of Point Contacts: Part III—Fully Flooded Results. *Journal of Lubrication Technology*, **99**(2), 264–275.

Hartinger, Markus, & Reddyhoff, Tom. 2018. CFD modeling compared to temperature and friction measurements of an EHL line contact. *Tribology International*, **126**(10), 144–152.

Hartinger, Markus, Dumont, Marie-Laure, Ioannides, Stathis, Gosman, David, & Spikes, Hugh. 2008. CFD Modeling of a Thermal and Shear-Thinning Elastohydrodynamic Line Contact. *Journal of Tribology*, **130**(4), 041503.

Havaej, Peyman, Degroote, Joris, & Fauconnier, Dieter. 2023. Sensitivity of TEHL Simulations to the Use of Different Models for the Constitutive Behaviour of Lubricants. *Lubricants*, **11**(3), 151.

Hersey, M. D. 1914. The laws of lubrication of horizontal journal bearings. *Journal of the Washington Academy of Sciences*, **4**(19), 542–552.

Hertz, H. 1881. On The Contact Of Elastic Solids. *J. Reine Angew. Math*, **92**(110), 156–171.

Horvat, F E, & Braun, M J. 2011. Comparative Experimental and Numerical Analysis of Flow and Pressure Fields Inside Deep and Shallow Pockets for a Hydrostatic Bearing. *Tribology Transactions*, **54**(4), 548–567.

Ibrahim, M. 1962. *The study of oil films between the teeth of running spur gears*. Ph.D. thesis, Imperial College, London.

Jakobsson, B., & Floberg, L. 1957. *The Finite Journal Bearing, Considering Vaporization*. Vol. 190. Göteborg, Sweden: Chalmers University of Technology.

Kasolang, S, Ahmad, M A, & Dwyer Joyce, R S. 2011. Measurement of circumferential viscosity profile in stationary journal bearing by shear ultrasonic reflection. *Tribology International*, **44**(11), 1264–1270.

Kasolang, S, Ahmed, I, Dwyer-Joyce, R S, & Yousif, B F. 2013. Performance analysis of journal bearings using ultrasonic reflection. *Tribology International*, **64**(1), 78–84.

Khonsari, M. M. 1987. A review of thermal effects in hydrodynamic bearings. Part ii: Journal bearings. *ASLE Transactions*, **30**(1), 26–33.

Kim, H. J., Ehret, P., Dowson, D., & Taylor, C. M. 2001. Thermal elastohydrodynamic analysis of circular contacts: Part 2: Non-Newtonian model. *Proceedings of the Institution of Mechanical Engineers, Part J: Journal of Engineering Tribology*, **215**(4), 353–362.

Kirk M. T. 1962. hydrodynamic lubrication of Perspex. *Nature*, **194**, 965–966.

Kosasih, P. B., & Tieu, A. K. 2004. An investigation into the thermal mixing in journal bearings. *Proceedings of the Institution of Mechanical Engineers, Part J: Journal of Engineering Tribology*, **218**(5), 379–389.

Kumar, A, & Booker, J F. 1991. A Finite Element Cavitation Algorithm. *Journal of Tribology*, **113**(2), 276–284.

Lane, T B P, Hughes, J R, & Mech, G I E. 1952. A study of the oil-film formation in gears by electrical resistance measurements. *British Journal Of Applied Physics*, **3**(10), 315.

Larsson, Per Olof, Jacobson, B., & Höglund, Erik. 1994. Oil drops leaving an EHD contact. *Wear*, **179**(1-2), 23–28.

Larsson, R., & Andersson, O. 2000. Lubricant thermal conductivity and heat capacity under high pressure. *Proceedings of the Institution of Mechanical Engineers, Part J: Journal of Engineering Tribology*, **214**(4), 337–342.

Lauer, J. L., & Peterkin, M. E. 1975. Analysis of Infrared Spectra of Fluid Films in Simulated EHD Contacts. *Journal of Lubrication Technology*, **97**(2), 145–150.

Layton, James, Rothwell, Benjamin C., Ambrose, Stephen, Eastwick, Carol, Medina, Humberto, & Rebelo, Neville. 2023. A New Thermal Elasto-Hydrodynamic Lubrication Solver Implementation in OpenFOAM. *Lubricants*, **11**(7), 308.

Layton, James, Rothwell, Benjamin C., Ambrose, Stephen, Medina, Humbero, & Eastwick, Carol. 2024. A Novel Multiscale Thermal Methodology for Application in Aerospace Transmission Systems. *In: Proceedings of the 18th UK Heat Transfer Conference*, vol. 9. Birmingham: University of Birmingham, for Proceedings of the 18th UK Heat Transfer Conference.

Li, Qiang, Zhang, Shuo, Wang, Yujun, Xu, Wei Wei, & Wang, Zhenbo. 2019. Investigations of the three-dimensional temperature field of journal bearings considering conjugate heat transfer and cavitation. *Industrial Lubrication and Tribology*, **71**(1), 109–118.

Lu, X, & Khonsari, M M. 2005. On the lift-off speed in journal bearings. *Tribology Letters*, **20**(12), 299–305.

Lubrecht, A. A., Ten Napel, W. E., & Bosma, R. 1987. Multigrid, an Alternative Method of Solution for Two-Dimensional Elastohydrodynamically Lubricated Point Contact Calculations. *Journal of Tribology*, **109**(3), 437–443.

Lugt, P M, & Morales-Espejel, G E. 2011. A Review of Elasto-Hydrodynamic Lubrication Theory. *Tribology Transactions*, **54**(3), 470–496.

Ma, M. T., & Taylor, C. M. 1996. An experimental investigation of thermal effects in circular and elliptical plain journal bearings. *Tribologv*, **29**(1), 19–26.

Ma, Mingfei, Wang, Wen, & Jiang, Wenxun. 2022. Experimental and numerical study on cavitation under elastohydrodynamic lubrication point contact. *Proceedings of the Institution of Mechanical Engineers, Part J: Journal of Engineering Tribology*, **236**(6), 1033–1042.

Martin, Ivo, Kurz-Hardjosoekatmo, Wolfram, & Schrewe, Sebastian. 2024. CFD Study of Journal Bearing Flow Physics and the Influence of Oil Feed Condition Within a Planetary Gearbox. *In: Proceedings of the ASME Turbo Expo 2024: Turbomachinery Technical Conference and Exposition*, vol. 12. American Society of Mechanical Engineers.

Meng, Fanming, & Chen, Yuanpei. 2015. Analysis of elasto-hydrodynamic lubrication of journal bearing based on different numerical methods. *Industrial Lubrication and Tribology*, **67**(5), 486–497.

Okamura, H. 1993. A contribution to the numerical analysis of isothermal elastohydrodynamic lubrication. *Pages 313–320 of: Proc. 9th Leeds-Lyon Symp*. Butterworth-Heinemann.

Olsson, Karl-olof. 1965. Cavitation in Dynamically loaded Bearings. *Chalmers University of Technology, Goteborg, Sweden*, **308**.

Palavecino, Jorge A, Cavalieri, Federico J, & Damián, Santiago Márquez. 2024. A second-order in time and space model to solve the coupled Reynolds-Rayleigh-Plesset equations for the dynamics of cavitated hydrodynamic journal bearings. *Tribology International*, **192**(1), 109206.

Pierre, Isabelle, Bouyer, Jean, & Fillon, Michel. 2004. Thermohydrodynamic Behavior of Misaligned Plain Journal Bearings: Theoretical and Experimental Approaches. *Tribology Transactions*, **47**(4), 594–604.

Ransegnola, Thomas, Sadeghi, Farshid, & Vacca, Andrea. 2021. An Efficient Cavitation Model for Compressible Fluid Film Bearings. *Tribology Transactions*, **64**(3), 434–453.

Reynolds, Osborne. 1885. On the dynamical theory of incompressible viscous fluids and the determination of the criterion. *Philosophical Transactions of the Royal Society of London. (A.)*, **186**(1), 123–164.

Reynolds, Osborne. 1886. On the theory of lubrication and its application to Mr. Beauchamp tower's experiments, including an experimental determination of the viscosity of olive oil. *Philosophical Transactions of the Royal Society of London*, **177**(1), 135–217.

Roelands, C J A. 1966 (1). *Correlational Aspects of the Viscosity-Temperature-Pressure Relationship of Lubricating Oils*. Ph.D. thesis, Technical University of Delft.

Rolls-Royce. *UltraFan*.

Sadinski, Robert J, & Doll, Gary. 2021. *The High Pressure Rheological Response of SAE as 5780 HPC, MIL-PRF-23699 HTS, and DOD-PRF-85734 Lubricants*. Ph.D. thesis, University of Akron, United States – Ohio.

Sander, D E, Allmaier, H, Priebsch, H H, Reich, F M, Witt, M, Füllenbach, T, Skiadas, A, Brouwer, L, & Schwarze, H. 2014. Impact of high pressure and shear thinning on journal bearing friction. *Tribology International*, **81**(1), 29–37.

Schirru, M M, Mills, R S, Smith, O, Dwyer-Joyce, R S, & Sutton, M. 2018. In situ Measurement of Journal Bearing Lubricant Viscosity by Means of a Novel Ultrasonic Measurement Technique Using Matching Layer. *Tribology Transactions*, **61**(1), 157–167.

Sibley, L. B., & Orcutt, F. K. 1961. Elasto-Hydrodynamic Lubrication of Rolling-Contact Surfaces. *Alse Transactions*, **4**(2), 234–249.

Singh, Kushagra, Sadeghi, Farshid, Russell, Thomas, Lorenz, Steven J, Peterson, Wyatt, Villarreal, Jaret, & Jinmon, Takumi. 2021. Fluid Structure Interaction Modeling of Elastohydrodynamically Lubricated Line Contacts. *Journal of Tribology*, **143**(9), 091602.

Škurić, V, Jasak, H, World, A Almqvist Trans Motauto, & 2019, undefined. 2019. Finite area algorithm for thin film cavitation in OpenFOAM. *Trans Motauto World*, **4**(1), 3.

Smart, A. E., & Ford, R. A.J. 1974. Measurement of thin liquid films by a fluorescence technique. *Wear*, **29**(1), 41–47.

Song, Yin, & Gu, Chun-Wei. 2015. Development and Validation of a Three-Dimensional Computational Fluid Dynamics Analysis for Journal Bearings Considering Cavitation and Conjugate Heat Transfer. *Journal of Engineering Gas Turbines and Power*, **137**(12), 122502.

Srinivas, Yunus Mohammed, Munshi Shadi M., & Hussain H. Iftekar. 2015. Performance Evaluation of Hydrodynamic Journal Bearing using Gearbox and Engine Oil (SAE90 and SAE20w50) by Experimental and Theoretical Methods. *International Journal of Mechanical Engineering and Information Technology*, **3**(12), 1573–1583.

Stefani, Fabrizio, & Rebora, Alessandro. 2009. Steadily loaded journal bearings: Quasi-3D mass–energy-conserving analysis. *Tribology International*, **42**(3), 448–460.

Stieber, W. 1933. *Das Schwimmlager: Hydrodynamische Theorie des Gleitlagers.* No. V.D.I., Berlin.

Stribeck, Richard. 1901. Ball bearings for any stress. *Z. des VDI*, **45**(1), 664.

Stribeck, Richard. 1902. Characteristics of plain and roller bearings. *Z. des VDI*, **46**(1), 19.

Swift, Herbert Walker. 1931. The Stability of Lubricating Films in Journal Bearings. *Minutes of the Proceedings of the Institution of Civil Engineers*, **223**(1), 267–288.

Szeri, A. Z. 2010. *Fluid film lubrication*. Cambridge University Press.

Tošić, Marko, Larsson, Roland, Jovanović, Janko, Lohner, Thomas, Björling, Marcus, & Stahl, Karsten. 2019. A Computational Fluid Dynamics Study on Shearing Mechanisms in Thermal Elastohydrodynamic Line Contacts. *Lubricants*, **7**(8), 69.

Turchine, V., Sanborn, D. M., & Winer, W. O. 1974. Temperature Measurements in Sliding Elastohydrodynamic Point Contacts. *Journal of Lubrication Technology*, **96**(3), 464–469.

Van Odyck, D E A, & Venner, C H. 2003. Compressible Stokes Flow in Thin Films. *Journal of Tribology*, **125**(3), 543–551.

Venner, C. H. 1991. *Multilevel solution of the EHL line and point contact problems*. Ph.D. thesis, University of Twente, Enschede, The Netherlands.

Vijayaraghavan, D., & Keith, T. G. 1989. Development and Evaluation of a Cavitation Algorithm. *Tribology Transactions*, **32**(2), 225–233.

Vijayaraghavan, D., & Keith, T. G. 1990. An Efficient, Robust, and Time Accurate Numerical Scheme Applied to a Cavitation Algorithm. *Journal of Tribology*, **112**(1), 44–51.

Weller Henry. 2020. *OpenFOAM 8*.

Yasutomi, S., Bair, S., & Winer, W. O. 1984. An Application of a Free Volume Model to Lubricant Rheology I—Dependence of Viscosity on Temperature and Pressure. *Journal of Tribology*, **106**(2), 291–302.

Zhang, C., Yi, Z., & Zhang, Z. 2000. THD Analysis of High Speed Heavily Loaded Journal Bearings Including Thermal Deformation, Mass Conserving Cavitation, and Turbulent Effects. *Journal of Tribology*, **122**(3), 597–602.